

EXPERIMENTAL DETERMINATION OF THE  
VELOCITY FIELD FOR BEHIND-THE-ARMOR DEBRIS (BAD)

BY

WILLIAM WINFIELD DYESS, JR.

A DISSERTATION PRESENTED TO THE GRADUATE SCHOOL  
OF THE UNIVERSITY OF FLORIDA IN PARTIAL FULFILLMENT  
OF THE REQUIREMENTS FOR THE DEGREE OF  
DOCTOR OF PHILOSOPHY

UNIVERSITY OF FLORIDA

1994

Copyright 1994

by

William Winfield Dyess, Jr.

## ACKNOWLEDGMENTS

I wish to thank my committee for their support and advice during this educational process. In particular, I thank Dr. C. Allen Ross for his advice, support, and encouragement. Without him this effort would not have been possible. I would like to thank Mr. Danny A. Brubaker for his help in the computation portion of this study. Without his effort, this portion could not have been completed. I would also like to thank my wife, Mildred, for her patience, support, and understanding throughout this effort. I would like to acknowledge the financial support of the Air Force Development Test Center at Eglin Air Force Base, Florida, and the personal support and encouragement of Dr. Dan Stewart, Mr. Ron Jacob, and Mr. Herb Brown. Finally, I wish to acknowledge the efforts of Mr. Steve Brown, Ms. Emily Farver, Mr. John Cleary, and Ms. Deborah Godwin for their support in the editing and layout of this dissertation.

## TABLE OF CONTENTS

	<u>page</u>
ACKNOWLEDGMENTS .....	iii
ABSTRACT .....	xv
CHAPTERS	
1 INTRODUCTION .....	1
Objective .....	1
Background .....	1
Approach .....	8
2 HARDWARE DESCRIPTION .....	10
General .....	10
Penetrator .....	10
Targets .....	10
3 TEST CONDUCT AND DATA REDUCTION PROCEDURES .....	13
General .....	13
Crater Characterization .....	15
Basic BAD Characterization .....	15
Enhanced BAD Velocity Characterization .....	30
4 DATA EVALUATION .....	40
General .....	40
Crater Characterization .....	49
Basic BAD Characterization .....	50
General .....	50
Target Plate Data .....	51
Spall Panel Data .....	53
Spall Mass Data .....	54
Spall Cap Velocity Data .....	57
Enhanced BAD Velocity Characterization .....	77
Method 1: Make Screen Method .....	77
Method 2: Radiographic Method .....	77
Chapter Summary .....	86



5	EULERIAN FINITE ELEMENT MODEL STUDY	87
	General	87
	Validation of Code Inputs	88
	General	88
	Semi-infinite Armor Characterization	88
	Finite Armor Characterization	100
	Comparison of Model Results to Test Results	110
	General	110
	Study of 2.50-Inch (0.0635 Meter) Target Impact (Fracture Strength = -1.30 GPa)	110
	Study of 2.50-Inch (0.0635 Meter) Target Impact (Fracture Strength = -0.85 GPa)	126
	Study of 2.00-Inch (0.0508 Meter) Target Impact (Fracture Strength = -0.85 GPa)	135
	Study of 0.75-Inch (0.01905 Meter) Target Impact (Fracture Strength = -0.85 GPa)	145
	Study of 2.50-Inch (0.0635 Meter) Target Impact (Fracture Strength = -0.50 GPa)	152
	Chapter Summary	160
6	HYDROCODE THEORY	161
	Background	161
	Governing Equations	162
	Introduction	162
	Conservation Equations	163
	Constitutive Relations	164
	Equations of State	168
	Failure Criteria	171
	Discussion of Equations	174
	Spatial Discretization	175
	Time Integration	176
	Artificial Viscosity	177
	Chapter Summary	177
7	SUMMARY, CONCLUSIONS, AND RECOMMENDATIONS	179
	REFERENCES	186
	BIOGRAPHICAL SKETCH	189

## LIST OF TABLES

<u>Table</u>	<u>page</u>
1 Classification of the Behavior of the Penetrator as a Function of Velocity in Terms of the Relative Strengths of Target and Penetrator . . . . .	7
2 Definition of Various Metallic Components of the Armor . . . . .	12
3 Test Condition for the Complete Test Series - Target Definition . . . . .	41
4 Test Condition for the Complete Test Series - Impact Data . . . . .	42
5 Test Condition for the Complete Test Series - Evaluation Summary . . .	43
6 Results of the Crater Test Series . . . . .	44
7 Results of the BAD Test Series - Target Plate, Spall Bundle, and Spall Cap Velocity Data . . . . .	45
8 Results of the Complete BAD Test Series - Spall Mass Data . . . . .	46
9 Velocity Field Data from Test CLG0982 . . . . .	47
10 Velocity Field Data from Test CLG0955 . . . . .	47
11 Velocity Field Data from Test CLG0953 . . . . .	48
12 Velocity Field Data from Test CLG0956 . . . . .	48
13 Parameter Definition for the Various Cases Evaluated with CTH for the Crater Characterization . . . . .	92
14 CTH Results Compared to Test CLG0854 . . . . .	92
15 CTH Results Compared to Test CLG0853 . . . . .	93
16 CTH Results Compared to Test CLG0855 . . . . .	93
17 CTH Results Compared to Test CLG0856 . . . . .	94
18 Finite Target Comparative Data . . . . .	108

19	Tracer Particle Velocity, Component Velocities, and Direction Angle at 500 Microseconds from Computation of Test CLG0982 (Fracture Strength = -1.30 GPa) .....	116
20	Tracer Particle Velocity, Component Velocities, and Direction Angle at 200 Microseconds from Computation of Test CLG0982 (Fracture Strength = -0.85 GPa) .....	127
21	Tracer Particle Velocity, Component Velocities, and Direction Angle at 200 Microseconds from Computation of Test CLG0875 (Fracture Strength = -0.85 GPa) .....	136
22	Tracer Particle Velocity, Component Velocities, and Direction Angle at 200 Microseconds from Computation of Test CLG0951 (Fracture Strength = -0.85 GPa) .....	146
23	Tracer Particle Velocity, Component Velocities, and Direction Angle at 200 Microseconds from Computation of Test CLG0982 (Fracture Strength = -0.50 GPa) .....	153

## LIST OF FIGURES

<u>Figure</u>	<u>page</u>
1 Velocity Distribution . . . . .	4
2 Cross Sections of Spall Bubble Concepts . . . . .	5
3 Event Ranges . . . . .	6
4 Schematic Drawing of the Penetrator . . . . .	11
5 Test Area C-64 . . . . .	17
6 Schematic of Test Area C-64 Setup . . . . .	18
7 Typical Preimpact Radiographs . . . . .	19
8 Preimpact Radiographic Setup . . . . .	20
9 Radiographic Setup for the BAD Debris Radiographs . . . . .	21
10 Technique Used to Define the Crater Characterization Data for Inclusion into the Database . . . . .	22
11 Primary Hole Measurements Taken for Inclusion into the Database . . .	23
12 Spall Ring Measurements Taken from the Sectioned Target for Inclusion into the Database . . . . .	24
13 Spall Witness Bundle Definition . . . . .	25
14 Typical Data Taken from the Spall Panels . . . . .	26
15 Positioning of the Spall Bundle in a Spall Box . . . . .	27
16 Design of the Spall Box Used for BAD Testing - Side View . . . . .	28
17 Design of the Spall Box Used for BAD Testing - Front View . . . . .	29
18 Front of One of the Quarter Steradian Zone Switch Screen Designs . . .	33

19	Side View of the Three-Array Form of the Quarter Steradian Zone Switch Screen Design .....	34
20	Schematic of the Process of Sectioning the Spall Cone .....	35
21	Schematic of the Enhanced Velocity Test Setup - Side View .....	36
22	Schematic of the Enhanced Velocity Test Setup - Sectioned View ....	37
23	Data Collection Area .....	38
24	Spall Cone Geometry versus Test Parameters .....	39
25	Comparison of the Actual Craters Created by the Penetrator .....	59
26	Database Data from the Crater Tests .....	60
27	Penetration versus Velocity .....	61
28	Calculated Crater Volume versus Kinetic Energy .....	62
29	Limit Thickness versus Velocity .....	62
30	Average Profile Hole Diameter as a Function of the Target Areal Density .....	63
31	Average Spall Ring Depth as a Function of the Target Areal Density .....	63
32	Average Spall Ring Diameter as a Function of the Target Areal Density .....	64
33	Sectioned Views - 2.0-Inch (0.0508 Meter) Targets .....	65
34	Sectioned Views - 2.5-Inch (0.0635 Meter) Targets .....	66
35	Rear View - 3-Inch (0.0762 Meter) Targets .....	67
36	Sectioned View of Selected BAD Targets .....	68
37	Sectioned View - 3.5-Inch (0.0889 Meter) Target .....	69
38	Computer Generated Plot of the Perforations of the First Spall Witness Panel for Selected BAD Tests .....	70
39	Number of Holes in Panel 1 of the Spall Bundle as a Function of the Target Density .....	71

40	Number of Holes in Panel 2 of the Spall Bundle as a Function of the Target Areal Density .....	71
41	Spall Half-Cone Angle as Measured on Panel 1 of the Spall Bundle as a Function of the Target Areal Density .....	72
42	Total Spall Mass as a Function of the Target Areal Density .....	72
43	Number of Fragments Whose Mass are Greater Than One Gram as a Function of the Target Areal Density .....	73
44	Total Nonferrous Spall Mass as a Function of the Target Areal Density .....	73
45	Total Ferrous Spall Mass as a Function of the Target Areal Density ...	74
46	Percent of Dust as a Function of the Target Areal Density .....	74
47	Mass Distribution Plot .....	75
48	Spall Cap Velocity Expressed as a Percent of the Impact Velocity as a Function of Target Areal Density .....	76
49	Typical Traces from the Make Screens .....	80
50	Standard Overhead Radiographic View behind a 0.75-Inch (0.01905 Meter) Target .....	81
51	Standard Side Radiographic View behind a 0.75-Inch (0.01905 Meter) Target .....	81
52	New Side Radiographic View behind a 0.75-Inch (0.01905 Meter) Target .....	82
53	Standard Overhead Radiographic View behind a 2.5-Inch (0.0635 Meter) Target .....	83
54	Standard Side Radiographic View behind a 2.5-Inch (0.0635 Meter) Target .....	83
55	New Side Radiographic View behind a 2.5-Inch (0.0635 Meter) Target .....	84
56	Fragment Velocity Test Data Compared to Single Bubble Predictions ..	85
57	Fragment Spatial Test Data Compared to Single Bubble Predictions ...	85
58	CTH Grid Pattern for Semi-infinite Armor Study .....	91

59	Volume Study .....	95
60	Penetration Depth Study .....	96
61	Comparison of the Crater Shape of CLG0853 to Those Predicted by Cases 1, 3, and 5 .....	97
62	Comparison of the Crater Shape of CLG0853 to Those Predicted by Cases 2, 3, and 4 .....	98
63	Comparison of the Crater Shape of CLG0854 to Those Predicted by Cases 1 and 3 .....	102
64	Comparison of the Crater Shape of CLG0855 to Those Predicted by Cases 1 and 3 .....	103
65	Comparison of the Crater Shape of CLG0856 to Those Predicted by Cases 1 and 3 .....	104
66	Predicted Crater Using Case 4 and CLG0853 Models and Values in a 3-D Evaluation .....	105
67	Range of BHN Encountered as a Function of RHA Thickness .....	106
68	Ultimate Tensile Strength versus BHN for Steel .....	107
69	CTH Grid Pattern for Finite Armor Study .....	108
70	Comparison of Measured versus Computed Spall Cap Velocity .....	109
71	CTH Grid Used for the Simulation of Test CLG0982 (2.50-Inch [0.0635 Meter] Target) .....	113
72	Tracer Particle Pattern for Simulation of Test CLG0982 .....	114
73	Computed Velocity Plot for Tracer 17 of CLG0982 .....	115
74	Computed Velocity Plot for Tracer 29 of CLG0982 .....	115
75	Calculated Velocity Vector Field for CLG0982 at Time = 0 Microsecond (Fracture Strength = -1.30 GPa) .....	117
76	Calculated Velocity Vector Field for CLG0982 at Time = 23 Microseconds (Fracture Strength = -1.30 GPa) .....	118
77	Calculated Velocity Vector Field for CLG0982 at Time = 53 Microseconds (Fracture Strength = -1.30 GPa) .....	119

78	Calculated Velocity Vector Field for CLG0982 at Time = 83 Microseconds (Fracture Strength = -1.30 GPa) . . . . .	120
79	Calculated Velocity Vector Field for CLG0982 at Time = 100 Microseconds (Fracture Strength = -1.30 GPa) . . . . .	121
80	Calculated Velocity Vector Field for CLG0982 at Time = 200 Microseconds (Fracture Strength = -1.30 GPa) . . . . .	122
81	Calculated Velocity Vector Field for CLG0982 at Time = 500 Microseconds (Fracture Strength = -1.30 GPa) . . . . .	123
82	Calculated Velocity Vector Field for CLG0982 at Time = 1,000 Microseconds (Fracture Strength = -1.30 GPa) . . . . .	124
83	Calculated Spall Cap Area for CLG0982 at Time = 1,000 Microseconds - Enlarged (Fracture Strength = -1.30 GPa) . .	125
84	Calculated Velocity Vector Field for CLG0982 at Time = 23 Microseconds (Fracture Strength = -0.85 GPa) . . . . .	128
85	Calculated Velocity Vector Field for CLG0982 at Time = 53 Microseconds (Fracture Strength = -0.85 GPa) . . . . .	129
86	Calculated Velocity Vector Field for CLG0982 at Time = 83 Microseconds (Fracture Strength = -0.85 GPa) . . . . .	130
87	Calculated Velocity Vector Field for CLG0982 at Time = 100 Microseconds (Fracture Strength = -0.85 GPa) . . . . .	131
88	Calculated Velocity Vector Field for CLG0982 at Time = 200 Microseconds (Fracture Strength = -0.85 GPa) . . . . .	132
89	Calculated Velocity Vector Field for CLG0982 at Time = 500 Microseconds (Fracture Strength = -0.85 GPa) . . . . .	133
90	Calculated Material Interface Plots for CLG0982 (Fracture Strength = -0.85 GPa) . . . . .	134
91	Tracer Particle Pattern for Simulation of Test CLG0875 . . . . .	137
92	Calculated Velocity Vector Field for CLG0875 at Time = 25 Microseconds (Fracture Strength = -0.85 GPa) . . . . .	138
93	Calculated Velocity Vector Field for CLG0875 at Time = 50 Microseconds (Fracture Strength = -0.85 GPa) . . . . .	139
94	Calculated Velocity Vector Field for CLG0875 at Time = 75 Microseconds (Fracture Strength = -0.85 GPa) . . . . .	140



95	Calculated Velocity Vector Field for CLG0875 at Time = 150 Microseconds (Fracture Strength = -0.85 GPa) .....	141
96	Calculated Velocity Vector Field for CLG0875 at Time = 200 Microseconds (Fracture Strength = -0.85 GPa) .....	142
97	Calculated Velocity Vector Field for CLG0875 at Time = 400 Microseconds (Fracture Strength = -0.85 GPa) .....	143
98	Calculated Material Interface Plots for CLG0875 (Fracture Strength = -0.85 GPa) .....	144
99	Tracer Particle Pattern for Simulation of Test CLG0951 .....	147
100	Calculated Velocity Vector Field for CLG0951 at Time = 25 Microseconds (Fracture Strength = -0.85 GPa) .....	148
101	Calculated Velocity Vector Field for CLG0951 at Time = 50 Microseconds (Fracture Strength = -0.85 GPa) .....	149
102	Calculated Velocity Vector Field for CLG0951 at Time = 75 Microseconds (Fracture Strength = -0.85 GPa) .....	150
103	Calculated Density/Velocity Vector Field for Late Times for CLG0951 (Fracture Strength = -0.85 GPa) .....	151
104	Calculated Velocity Vector Field for CLG0982 at Time = 25 Microseconds (Fracture Strength = -0.50 GPa) .....	154
105	Calculated Velocity Vector Field for CLG0982 at Time = 75 Microseconds (Fracture Strength = -0.50 GPa) .....	155
106	Calculated Velocity Vector Field for CLG0982 at Time = 100 Microseconds (Fracture Strength = -0.50 GPa) .....	156
107	Calculated Velocity Vector Field for CLG0982 at Time = 200 Microseconds (Fracture Strength = -0.50 GPa) .....	157
108	Calculated Velocity Vector Field for CLG0982 at Time = 500 Microseconds (Fracture Strength = -0.50 GPa) .....	158
109	Calculated Material Interface Plots for CLG0982 (Fracture Strength = -0.50 GPa) .....	159
110	Comparison of the Calculated Values for BAD Velocity and Those Determined from Actual Tests - 0.75-Inch (0.01905 Meter) Target .....	181

111	Comparison of the Calculated Values for BAD Velocity and Those Determined from Actual Tests - 2.00-Inch (0.0508 Meter) Target . . . . .	181
112	Comparison of the Calculated Values for BAD Velocity and Those Determined from Actual Tests - 2.50-Inch (0.0635 Meter) Target . . . . .	182
113	Tracer Point Velocities as a Function of Origin for 2.50-Inch (0.0635 Meter) Target Impact (Fracture Strength = -0.85 GPa) . . .	185
114	Tracer Point Velocities as a Function of Origin for 2.50-Inch (0.0635 Meter) Target Impact (Fracture Strength = -0.50 GPa) . . .	185

Abstract of Dissertation Presented to the Graduate School  
of the University of Florida in Partial Fulfillment of the Requirements  
for the Degree of Doctor of Philosophy

EXPERIMENTAL DETERMINATION OF THE  
VELOCITY FIELD FOR BEHIND-THE-ARMOR DEBRIS (BAD)

By

WILLIAM WINFIELD DYESS, JR.

December 1994

Chairman: C. Allen Ross

Major Department: Aerospace Engineering, Mechanics and Engineering Science

Impacts of deforming/eroding projectiles on metallic armors generate a highly energetic debris field behind the armor during the perforation process. In the community involved with this event, the debris field is referred to as the behind-the-armor debris (BAD) field. The study of BAD and its effects, as defined in this dissertation, was started in 1959. Since that time, various empirical models have been developed which strive to predict the field. Only recently have the capabilities of the hydrocodes been added.

The BAD field is generally studied as several components: fragment spatial distribution, fragment mass distribution, and fragment velocity distribution. This dissertation addresses one of the basic issues of the last component. Prior to this work, there were two theories in the community. The first was that the fragments in the BAD field were on the outer edge of the expanding BAD field (single bubble

theory). This resulted in a single parabolic distribution of the velocity field about the line of impact. The shape of the parabola was then adjusted to provide an overall energy match. The second theory was that the fragments in the BAD field were distributed over a series of expanding fronts (multiple bubble theory).

This study proves conclusively that the single bubble theory is invalid. High fidelity data is presented which refutes the concept, and a test technique was developed and is presented which can be used to acquire further high fidelity data for continued studies. In addition, an advanced test technique is discussed which would allow, with some developmental effort, the ability to collect high fidelity data as a part of the standard BAD field characterization, thus reducing the cost of obtaining the data.

This dissertation also contains a study of the ability of a commercial hydrocode to duplicate the results of the tests. The results were encouraging, and areas where further work is needed were identified. The dominant data input for matching the resulting BAD field to that determined from the test was found to be the fracture strength. Further work in characterizing this parameter in the high strain rate environment needs to be accomplished.

## CHAPTER 1 INTRODUCTION

### Objective

The primary goal of the proposed investigation was to obtain an improved understanding of the velocity in the behind-the-armor debris (BAD) field resulting from projectile impact. To accomplish this, a new test technique was developed to obtain the required velocity data. A correlation between the resulting test data and the results from a commercially available hydrocode was sought. It was not the intent of this study to remodel the complete penetration process, but considerable review of this area was necessary in order to understand the latter stages of this event which formed the basis of the fragmentation process. Comparison will involve fragment size, fragment velocity, and fragment size distribution.

### Background

BAD, as used in this dissertation, is defined as the debris behind the target plate, or armor, which was composed of fractured target and projectile material. For this study, this BAD was generated by the penetration/perforations of a target plate by a deforming/eroding projectile. This BAD should not be confused with the debris associated with penetration/perforation of a rigid projectile which may result in scabbing, plugging, or petaling. In general, this latter event was reasonably understood and modeled.

The history of BAD modeling is fairly recent. In 1959, a test series known as the Canadian Armament Research and Development Establishment (CARDE) trials [1] was conducted. This was the beginning of the modern understanding of BAD effects. This test series evaluated the damage done to "modern" tanks by "modern" shape charge warheads. Using this data, Nail, Jackson, Beardon [2] and others developed the first models, using a consistent data set, for predicting the loss of combat utility for tanks. These models were expanded to include all ground mobile targets. These early models were so-called "compartment" models. The models related the probability of the loss of combat utility of a ground mobile target to the size of the hole made by the shape charge jet. The model was referred to as a "compartment" model because each compartment of the ground mobile target (i.e., turret, engine area, crew compartment, etc.) was assigned a different loss of combat utility requirement. The use of this type of simple model has continued over the years because of its low cost and small data requirements. To keep the technique current and usable, several changes have been made. The more important were as follows: 1) a minimum residual penetration for both jets and long rod penetrators was defined, which ensured ample residual energy accompanied the armor hole size to generate the required lethality; and 2) the definitions of the "compartments" have been changed, and current damage data have been added to augment the damage predictions.

In the 1980s, the concept of a point burst methodology was introduced. This technique required a detailed geometric model of the target since the concept was to model the spall field and predict the damage to the target components. The most notable of the models were developed by Flint [3], Nail [4], and Ozolins [5].

Once the damaged components were determined, a criticality analysis was used to determine the effect of the damage on the combat utility of the vehicle.

The development of the point burst methodology has been largely performed by analysts, and statistical techniques have been used throughout. The methodology could be referred to as a statistical fit to empirical data with little physics or continuum mechanics used. The point burst methodology has allowed major improvements in the prediction of vehicle vulnerability. This ability was even better when the actual warhead tests data were incorporated into the model. With one notable exception, techniques have been developed which enabled a standardized collection of data to determine the necessary BAD field parameters. The one parameter which remained unresolved was the velocity of the fragments in the BAD field.

The best velocity model was based entirely on the spall cap velocity. The spall cap velocity was easily obtainable from radiographic coverage of the spall field behind the armor. This spall cap velocity (sometimes referred to as the residual penetrator velocity) was the maximum fragment velocity along the shot line. The fragment velocities were modeled, by quarter steradian zones, using an energy balance. The central zone was assigned the velocity of the spall cap, the next zone was assigned a reduced velocity, etc. The velocity assignment was based on a parabolic distribution. All fragments within each zone were assigned the velocity of that zone, and a total energy was calculated for the spall field. If the value of the energy of the spall field minus that of the impact event was other than zero, the parabolic distribution was modified. This continued until an energy

balance was achieved. This process is further explained in Chapter 4. Figure 1 presents a schematic of this type of distribution.

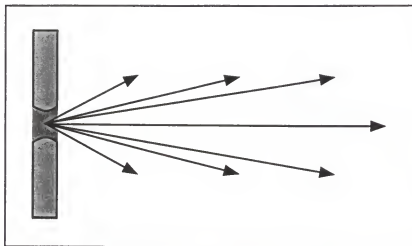


Figure 1. Velocity Distribution

No one in the field assumed this technique was exact, and everyone agreed that it could be improved. However, at the time of this study, there was disagreement about what form the improvement should take. The basic problem was that there were two assumptions as to the composition of the BAD field. The first was that all mass in the debris field was on the expanding spall bubble. The second was that the expanding spall field was composed of several bubbles, each with its own velocity field. These concepts are shown in Figure 2. Before any further meaningful work could be done in this area, the true composition of the BAD field needed to be resolved experimentally.



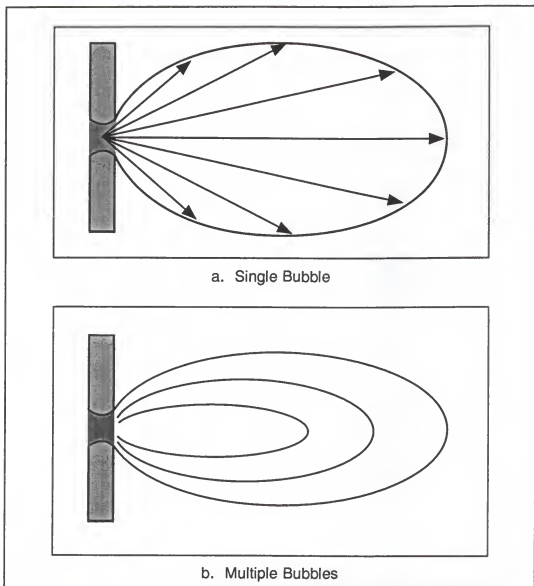


Figure 2. Cross Sections of Spall Bubble Concepts

The primary areas of current interest for the defeat of ground mobile targets are in the high transition and hydrodynamic ranges which are characterized by large numbers of energetic fragments resulting in a complex and highly lethal spall field. These areas are defined in Figure 3 as Phases II and III. The line appearing as a horizontal line and labeled the hydrodynamic limit is calculated from Equation 1-1 below.

$$\frac{P}{L} = \sqrt{\frac{\rho_p}{\rho_t}} \quad (1-1)$$

where:

$P$  is the penetration depth

$L$  is the length of penetrator

$\rho_p$  is the density of the penetrator material

$\rho_t$  is the density of the target material

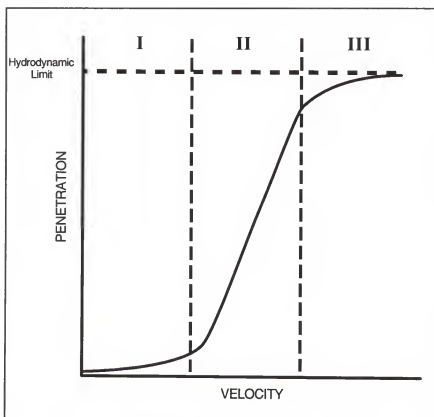


Figure 3. Event Ranges

As an example, for a copper penetrator and a rolled homogeneous armor (RHA) target, the hydrodynamic limit was 1.07 and occurred at a velocity of approximately 2.3 to 2.5 kilometers per second (km/s).

Figure 3 could be calculated for any penetrator material versus target material, and the shape of the curve would change depending on their properties. The displayed shape is for materials which deform during the penetration process. The events discussed in this report were contained in late event range II. and early event range III. It should be noted that in this region the transverse wave velocities in the target were of the same order of magnitude as the penetration front velocity. Woodward [6] presented this consideration in a different manner in Table 1. The materials which will be discussed in this report fall within the first category of this table, and the velocity regime is well within the last block. The yield strengths discussed in Table 1 should be the dynamic yield strength of the materials at the strains rates to be encountered in the event. For the higher strain rate regions where values as high as  $10^6$  /s may be encountered, split Hopkinson bar data (order  $10^4$  /s) was generally used as the most applicable.

Table 1. Classification of the Behavior of the Penetrator as a Function of Velocity in Terms of the Relative Strengths of Target and Penetrator

Relative Flow Stress of Projectile and Target	Behavior with Increasing Velocity		
	Mushrooming	Projectile enters target and deforms inside target	
$\sigma_{yp} < \sigma_{yt}$	Mushrooming	Projectile enters target, but projectile elements inside target do not deform	
$\sigma_{yt} < \sigma_{yp} < 3\sigma_{yt}$	Mushrooming	Projectile enters target, but projectile elements inside target do not deform	Projectile deforms inside target
$\sigma_{yp} > 3\sigma_{yt}$	Projectile enters target without deforming	Projectile elements outside target deform, but those within do not	Both projectile and target deform
Note: $\sigma_{yp}$ - Yield strength of penetrator $\sigma_{yt}$ - Yield strength of target			

In the late 1980s, modifications were made to the hydrocodes by Johnson, Stryk, Holmquist, and Souka [7] and Grady [8] which enabled the codes to predict the spall field parameters. Even though these codes predicted the spall fields, they were too costly and time consuming to be used for vulnerability analyses. Vulnerability analyses involved several thousand impact points of a munition on a target to determine the overall probability of reduction of combat utility. Zukas and Kimsey [9] presented data showing that a typical three-dimensional calculation of one impact required 39 hours of Cray X-MP central processing unit (CPU) time. Thus, it was unlikely that the vulnerability community would embrace the hydrocodes as a tool of its trade.

Since the spall modeling part of the codes had never been incorporated in actual spall prediction associated with vulnerability studies, their true ability to predict results within the complex environment of a real-world engagement had not been assessed. Alternately, the current techniques have been through exhaustive evaluation in this manner.

What was needed was a better understanding of the event so that a standard production test method could be developed, or a current one modified, to generate the required fragment velocity data. Alternately, if the code capability could be verified for this regime, then the codes could be used to generate the basic data for the vulnerability models, thus reducing the overall cost of testing.

#### Approach

Step 1: A series of tests would be conducted involving the impact of a copper rod on various thicknesses of RHA. These impacts would be concentrated in the 1.5- to 2.3-km/s velocity range. This range was selected for the reasons as

follows: 1) the region was commonly encountered for projectiles of this size in practical applications, and 2) the region involves the transition range between dynamic strength dependence and hydrodynamic flow. Data would be gathered to characterize the terminal effects of the penetrator. This characterization would include the composition of the BAD field as a function of the armor thickness and the impact velocity. Portions of the BAD field from selected tests would be examined to determine the mass and velocity vector of the individual fragments. The details of this step are discussed in Chapters 2 through 4.

Step 2: A series of simulations of the tests conducted in Step 1 would be generated using a commercially available hydrocode. The purpose of this portion of the study was to investigate the BAD phase of the event. The grid size and constitutive model inputs would be adjusted until the penetration/perforation predictions of the code matched the parameters found in the characterization performed in Step 1. The primary parameters which would be considered during this process would be the semi-infinite penetration depth and the residual penetrator velocity. After the adjustments were made, the code would be used to investigate the agreement between the predicted BAD parameters and those found in the tests of Step 1 for the failure criterion provided with the code. The details of this step are discussed in Chapters 5 and 6.

Step 3: Conclusions would be drawn as to the merit of the hydrocode as applied to this problem. A recommendation would be made as to the type of standard test which could be employed to provide the necessary data in a production environment. The details of this step are discussed in Chapter 7.

## CHAPTER 2 HARDWARE DESCRIPTION

### General

The hardware used in this series consisted of the penetrator and target as well as the test diagnostic equipment which is fully covered in the work by Dyess [10]. The diagnostic equipment will not be further discussed, except in general terms. The penetrator and targets are discussed in the following paragraphs.

### Penetrator

Figure 4 presents the schematic of the penetrator used in these tests. The purpose of the aluminum drag cone was only to provide stability. Its effect on the terminal effects of the penetrator should be minimal. The material of the penetrator itself was annealed copper.

### Targets

There was only one type of target examined under this effort which was various thicknesses of RHA. The basic parameters of RHA are presented in Table 2. The high hard armor data are presented for comparison as this was the hardest metal used for general armor efforts, and the mild steel data are presented for general comparison and also because they were used in the witness packages (spall bundles).

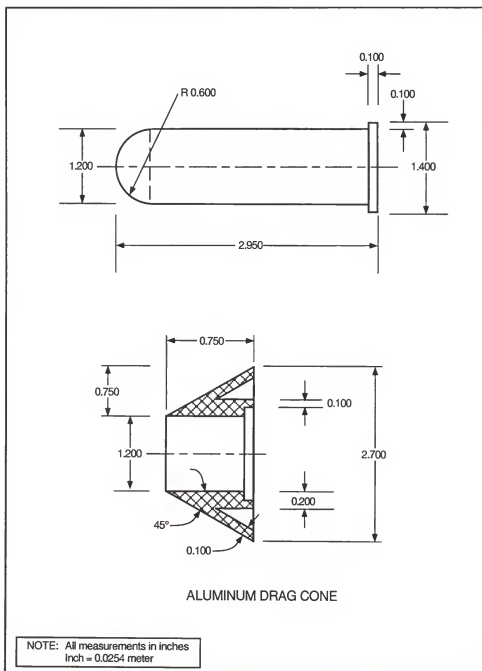


Figure 4. Schematic Drawing of the Penetrator

Table 2. Definition of Various Metallic Components of the Armor

Armor Type	Military Specification	Brinell Hardness Number (BHN)	Thickness Range (in.)
High hard	A-46100-3	418-555	0.25 - 1.50
RHA	A-125606	269-418	0.25 - 6.00
Mild steel	S-7952	100-156	0.06 - 0.13
Note: in. - Inch = 0.0254 meter			



## CHAPTER 3 TEST CONDUCT AND DATA REDUCTION PROCEDURES

### General

A complete review of how the basic tests were conducted and the data reduced was written by Dyess [10]. In general, the tests were conducted on Test Area C-64 (Figures 5 and 6) at Eglin Air Force Base (AFB), Florida. The penetrators were fired from the 125-millimeter (mm) smooth bore gun. In addition to the basic tests discussed in the work by Dyess [10], special tests for determining the BAD velocity vector fields were conducted. The test conduct and data reduction procedures for these special tests will be discussed in detail later in this section.

Reduction of the basic data was accomplished in the usual format for crater characterization and BAD characterization as discussed in the work by Dyess [10] for explosively formed penetrators (EFP). Although not an EFP, this penetrator was similar with regard to the terminal effects; thus, the test procedure and data reduction procedure were basically the same. This included crater data, profile hole diameter data, spall ring data, spall panel data, spall mass data, and spall cap velocity data.

The preimpact data for these tests were mostly taken from radiographs. Figure 7 presents a typical set of preimpact radiograph. The two radiographs were taken in orthogonal planes. Not only could the velocity be calculated, but also the preimpact angles and rotational rates were measurable. Figure 7 shows a sizable preimpact pitch and almost no yaw. In order to insure that data reduction

confusion was minimized, a standard practice involving the numbering of the radiographic plates was adopted. Odd-numbered plates were used for vertical (overhead) views and even-numbered plates were used for horizontal (side) views. A schematic of the preimpact radiographic setup is presented as Figure 8. Figure 7 also demonstrates one of the strengths of this dual-source, orthogonal system. Even if one of the sources were to fail (as it did in this case), the required results would be obtainable. Occasionally, the radiographic data for the preimpact portion of the experiment was not available. For these cases, the preimpact velocity was obtained from a make screen. Make screens were composed of two sheets of conducting material with a sheet of nonconducting material separating them. When the projectile or other conducting material penetrated the screen, an electrical circuit was made and the event was recorded. Two of these screens, at a known distance apart, were used as a backup source of velocity data to the radiographic instrumentation. Due to the reduced accuracy in the velocity data and the inability to obtain orientation data, the make screen data was not the preferred source.

A radiographic setup (Figure 9) similar to, but more extensive than, the preimpact setup was used to collect data on the BAD field's overall shape and the spall cap velocity. Again, a set of make screens were used as a backup source of spall cap velocity data. Here the screen data can be even more misleading since a small fragment in front of the spall cap can easily be what triggers the screen.

In order to understand the technique which was used to present the basic data, the term "areal density" must be defined. Thickness and areal density were related through a simple calculation. The areal density was computed by dividing

the mass of the base armor, or target, by the frontal area perpendicular to the projectile flightpath. This calculation, throughout this report, resulted in units of kilograms per square meter ( $\text{kg/m}^2$ ). The equivalent thickness, in inches, was simply the areal density divided by 200  $\text{kg/m}^2$  inches. This constant is the areal density of 1 inch (0.0254 meter) of steel. This method of presenting the data was common within the lethality/vulnerability community where the practice has been found to be beneficial when dealing with complex targets.

#### Crater Characterization

The crater data were taken in accordance with the requirements of Dyess [10], as shown in Figure 10. Notice that the data were taken every quarter inch (0.00635 meter) into the armor from a section of the crater. This allowed for calculations involving the volume of the crater as well as determining the exact depth of penetration. Note that the bulge was also recorded. This information was used in calculating the true "semi-infinite" depth of penetration. This is the penetration which would occur in a homogeneous, continuous media of infinite thickness.

#### Basic BAD Characterization

The BAD or spall data were collected in accordance with the requirements in the report by Dyess [10]. In summary, this meant that hole data were taken in accordance with the definitions given in Figures 11 and 12. The profile hole diameter was the diameter of the smallest cross-section of the perforation. This diameter was recorded both vertically and horizontally and the average of the two values obtained. The spall panel data were taken using the spall bundle, as

defined in Figure 13. Figure 14 presents a processed spall panel with quarter steradian zones drawn on the panel. Figure 15 reveals the placement of the spall panel in the spall box behind the target. This arrangement can also be seen in Figure 6. Figures 16 and 17 show the spall box used for these tests. This box was used to completely contain all spall fragments.

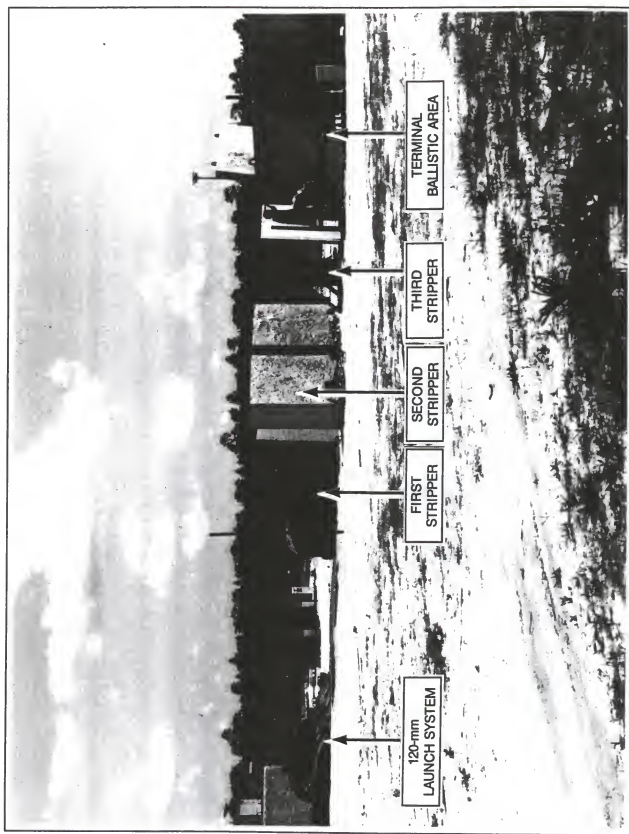


Figure 5. Test Area C-64

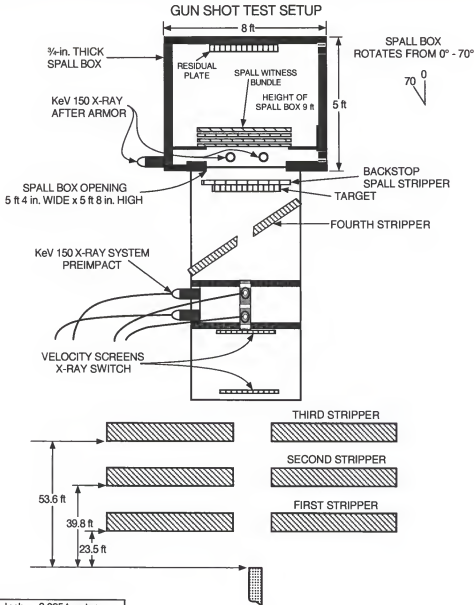


Figure 6. Schematic of Test Area C-64 Setup

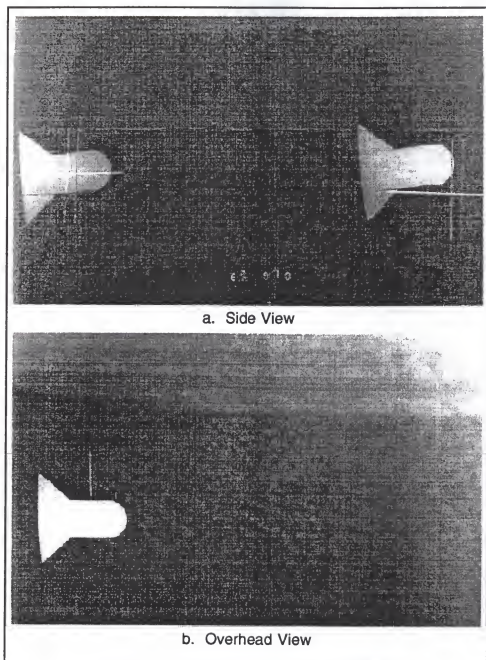


Figure 7. Typical Preimpact Radiographs

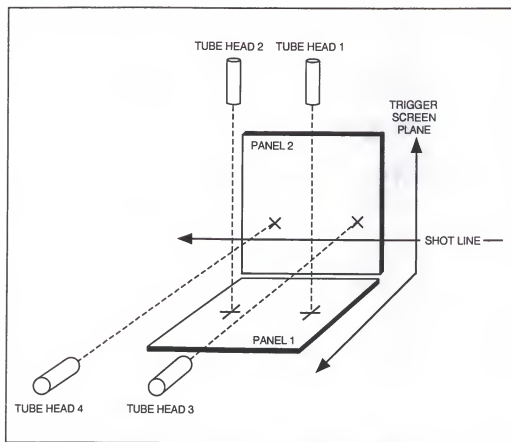


Figure 8. Preimpact Radiographic Setup



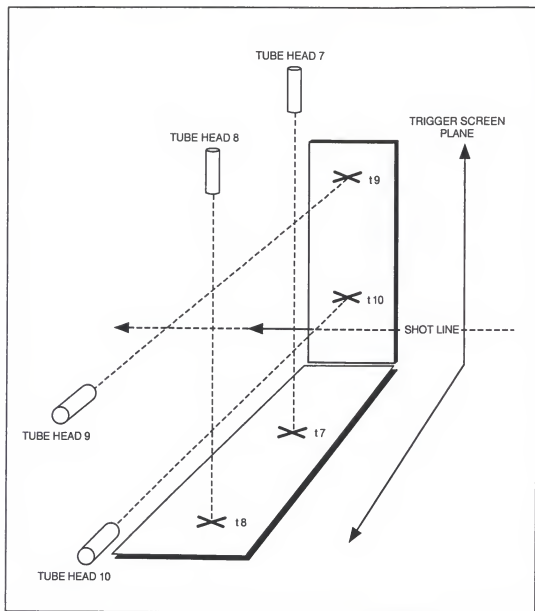


Figure 9. Radiographic Setup for the BAD Debris Radiographs

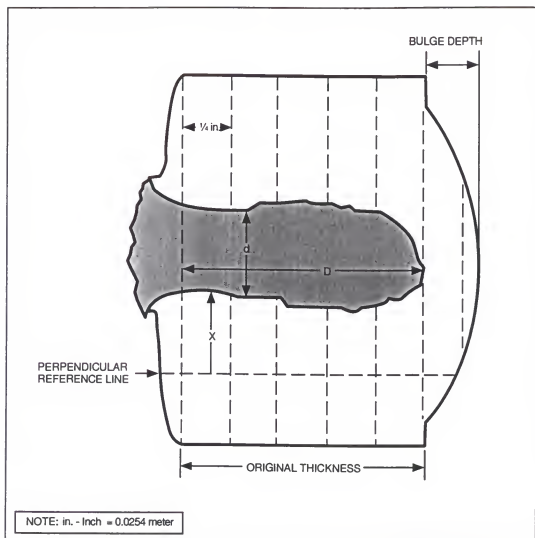
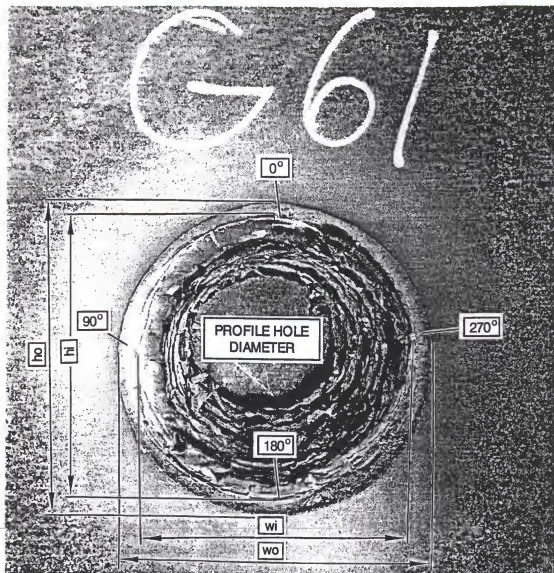


Figure 10. Technique Used to Define the Crater Characterization Data for Inclusion into the Database



Note: hi - Inside Height of Spall Ring  
ho - Outside Height of Spall Ring  
wi - Inside Width of Spall Ring  
wo - Outside Width of Spall Ring

Figure 11. Primary Hole Measurements Taken for Inclusion into the Database

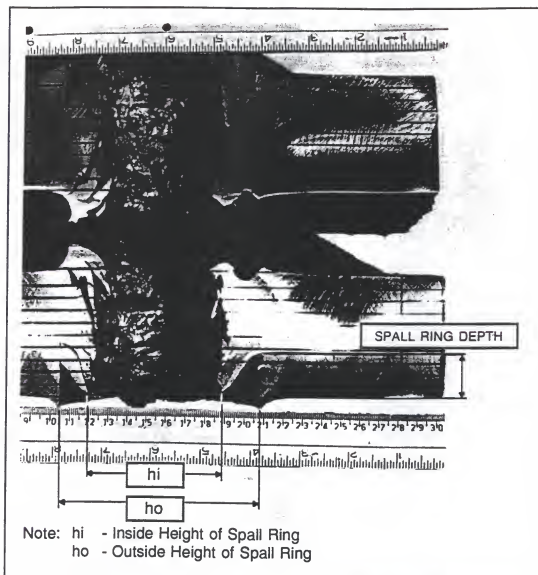
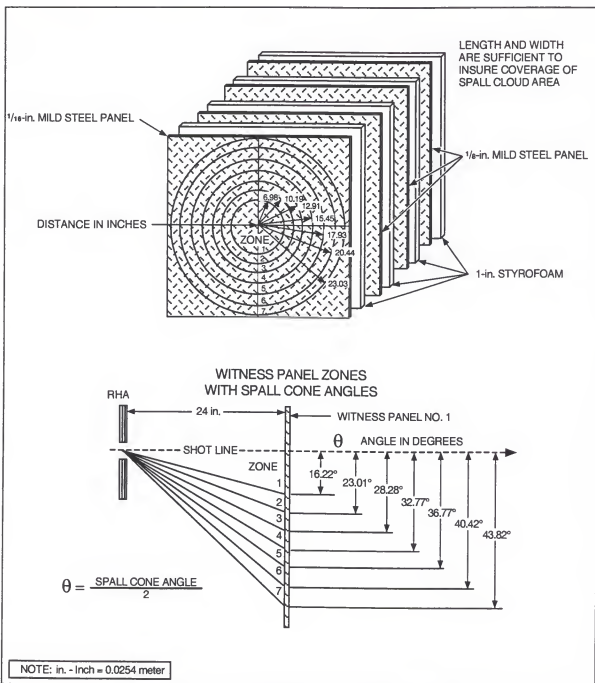


Figure 12. Spall Ring Measurements Taken from the Sectioned Target for Inclusion into the Database



NOTE: Cross Hairs is Aimpoint. Numbers on Upper Right are Shot Line Correction from Aimpoint.

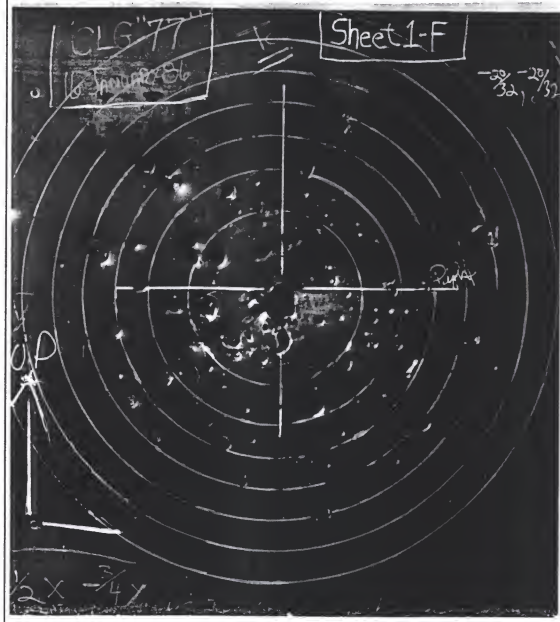


Figure 14. Typical Data Taken from the Spall Panels

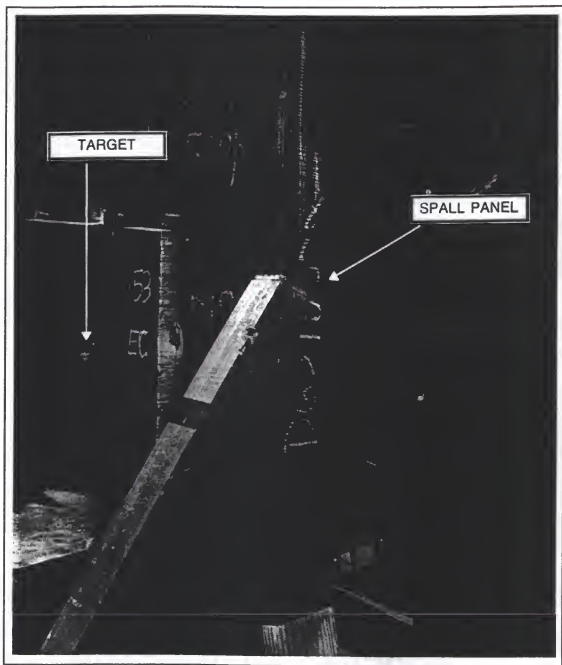


Figure 15. Positioning of the Spall Bundle in a Spall Box

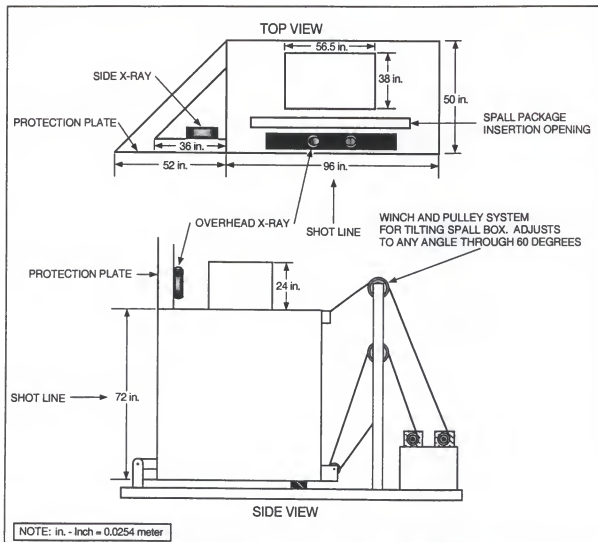


Figure 16. Design of the Spall Box Used for BAD Testing - Side View



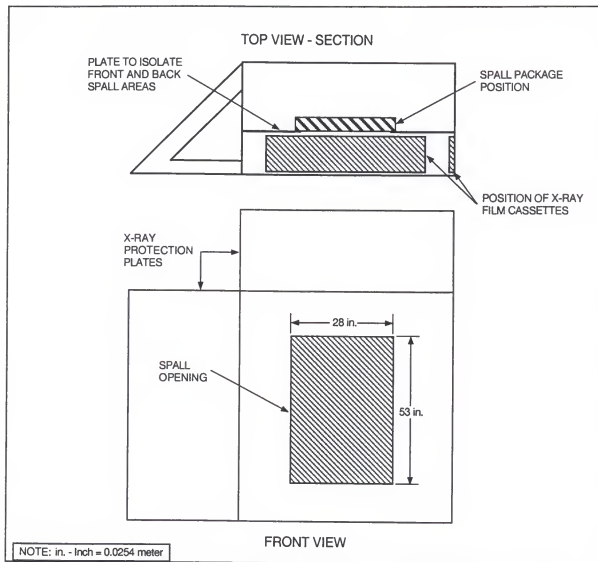


Figure 17. Design of the Spall Box Used for BAD Testing - Front View

### Enhanced BAD Velocity Characterization

The problem with obtaining the individual spall fragment velocities was the inability to determine which fragment was which on a radiographic view. The fragments were irregular, plate-like in shape, and usually tumbling. Thus, the shadows which they cast on the radiographic plates generally were not the same when viewed from two points or at two times. Add to this the complexity of some of the fragments approaching the radiographic source and some approaching the radiographic film, and the problem became insurmountable with current capabilities.

Two different methods were attempted during this effort. The first was to place from 16 to 32 make screens in two or three arrays between the back of the target and the front of the witness bundle. The distance between the target and the witness bundle was only 2 feet (0.6096 meter) in the normal setup, a small area to use for this type of experiment. Figures 18 and 19 show one of the several setups examined. For this particular attempt, three make screen arrays at 6 inches (0.1524 meters) apart were used. The goal of this method was to obtain the velocity of the spall fragments in quarter steradian zones without affecting the gathering of the normal, required data. To match the generally used data format, the make screens were made in the shape of quarter steradians and, in some cases, further divided so that several distinct screens composed each quarter steradian zone. Besides the setup already shown, an attempt was made to take data with even smaller zones thus reducing the number of impacts per zone. Since the number of recording channels was limited, this necessitated that only a quarter of the spall cone be covered. That is, instead of the screens being over the entire surface of the witness bundle, only a quarter of the witness bundle face was covered. A further attempt was made by removing the witness bundle and placing the screens at a larger standoff from

the rear of the target. This allowed the BAD field to spread and enabled the screens to be further separated. For typical make screen work, this technique will result in improved accuracy. Additionally, this allowed for the first screen to be further removed from the breakout point on the back side of the armor which reduced the impacts of small, ineffective particles. For all of these techniques, the data were recorded with a Pacific Model 5700 Portable Data Acquisition System with a sample rate of 500 kilohertz (kHz).

The second method involved the "slicing" of a portion of the spall cone. This concept is shown in Figure 20. The schematic of the basic setup used is shown in Figures 21 and 22. Specific experiment related values (such as spatial relationship between the back of the target where the perforation was assumed to be going to occur and the various radiographic sources and make screens) were recorded prior to each experiment and adjusted based on the actual perforation point after each test. The high density polyethylene was used as the surface of the front plate to suppress the number and velocity of the BAD fragments which were eliminated from the continuing BAD field by the plate. This was done to reduce the potential damage which these fragments could cause in the test area. The portion of the polyethylene surface which normally incurred the most damage was designed so that it could easily be replaced for each experiment. Figure 23 presents the data collection area. This setup was different than the standard BAD test setup. Therefore, in order to generate this data as a standard portion of BAD data in a production environment, additional tests would be required. This would result in additional costs which was seen as a distinct disadvantage. However, the hope was to obtain enough data and understanding so that techniques similar to those previously explained could be employed. This test method again employed the Pacific instrumentation. However, the primary method of data collection was through

radiographic reduction. Since only a narrow band of the spall cone was allowed into the zone where the radiographic data were collected, the data were much easier to reduce. After reduction of the data to determine the velocity vector for each fragment of interest, each fragment was traced back to the approximate point of origin. If this point was not within, or nearly within, the exit hole of the penetrator through the target, the fragment was determined to have been affected by the slicing of the spall field. This could have happened, for example, by a deflection of the fragment due to an impact on the sides of the opening in the first plate. In addition to the radiographic and make screen data, the fragments were captured and weighed. Frequently the fragments directly on the shot line were not captured because of the excessive kinetic energy of this zone. This could be done in later tests as it has been done for other efforts.

One final point should be noted about these tests. The first method described would generate all data required for the complete characterization of the BAD velocity field. The second method would not. There were two primary reasons for this. First, the method investigates only a slice of the BAD field, not the entire field. Thus, the results would have to be manipulated to model the entire BAD velocity field. Second, due to geometric constraints as shown in Figure 24, only a portion of the BAD field slice was analyzed. This coverage could be improved for future tests. However, the second method was designed for the specific purpose of observing the general makeup of the BAD field. Both test methods may be required to completely characterize the BAD velocity field.

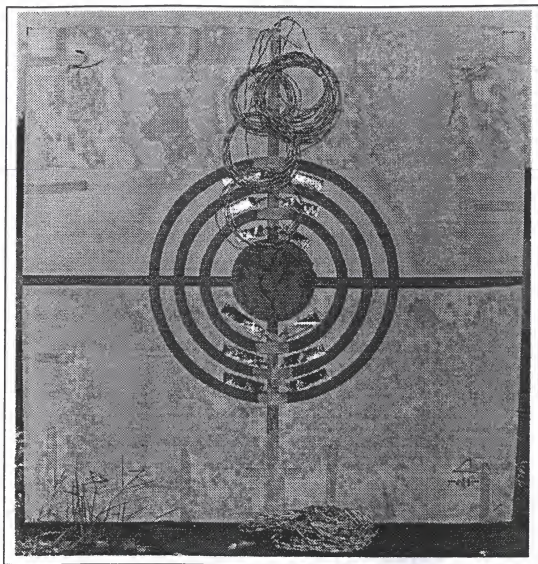


Figure 18. Front of One of the Quarter Steradian  
Zone Switch Screen Designs

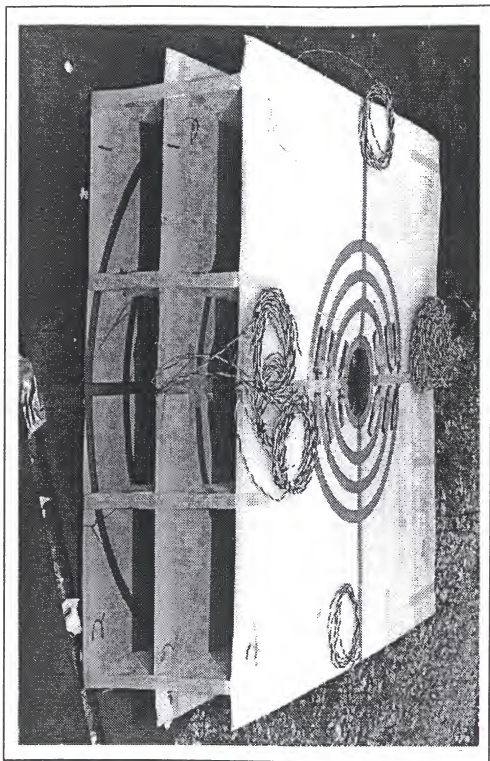


Figure 19. Side View of the Three-Array Form of the Quarter Steradian Zone Switch Screen Design

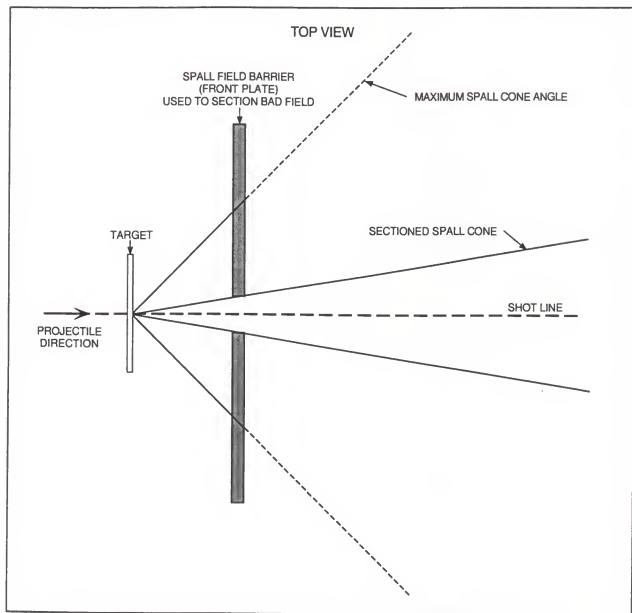
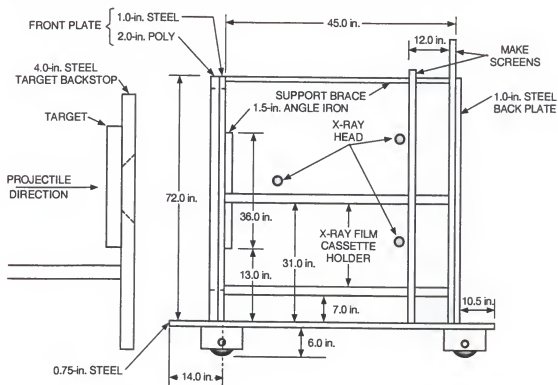


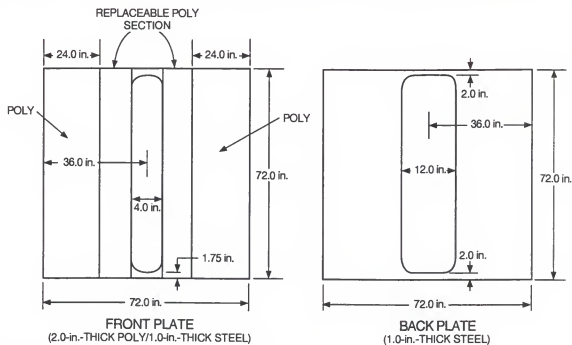
Figure 20. Schematic of the Process of Sectioning the Spall Cone



NOTE: Not to scale  
 in. - Inch = 0.0254 meter  
 POLY - High density (1 gram per cubic centimeter) polyethylene

Figure 21. Schematic of the Enhanced Velocity Test Setup - Side View





NOTE: Not to scale  
 in. - Inch = 0.0254 meter  
 POLY - High density (1 gram per cubic centimeter) polyethylene

Figure 22. Schematic of the Enhanced Velocity Test Setup - Sectioned View

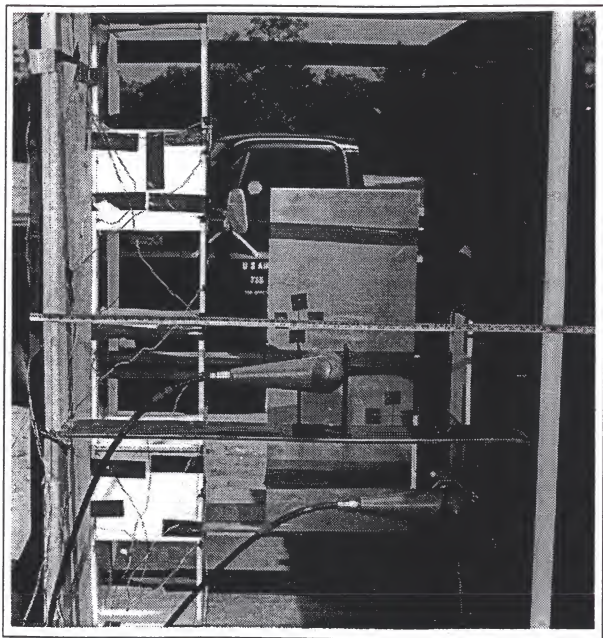


Figure 23. Data Collection Area

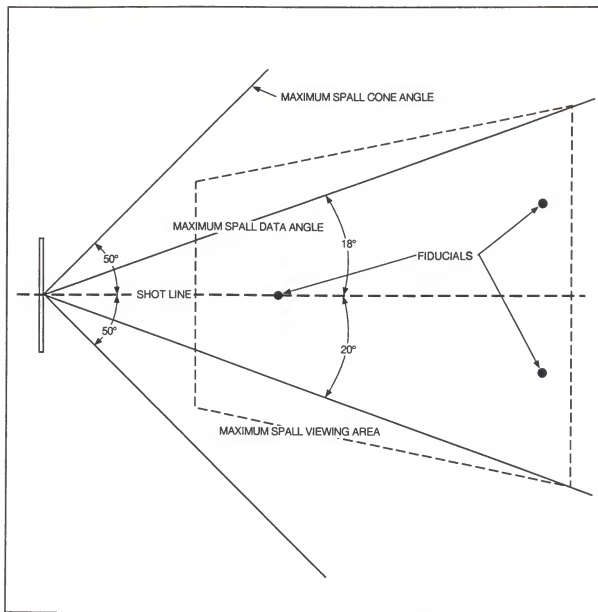


Figure 24. Spall Cone Geometry versus Test Parameters

## CHAPTER 4 DATA EVALUATION

### General

In this dissertation, all of the collected and reduced data will be presented, and then each set will be discussed in the appropriate subsection. Tables 3, 4, and 5 present the preimpact data for all tests. Table 6 presents the crater data for all crater tests, and Tables 7 and 8 present the BAD data for all BAD tests. Tables 9, 10, 11, and 12 present reduced fragment velocity data for those tests which were of sufficient quality for the reduction to be meaningful. The use of "ND" in the tables denotes that no data were available for that entry. The use of "N" or "NA" denotes that data were not applicable for this test.

The standard method for collecting data as outlined by Dyess [10] were followed. This method results in data being acquired in the units with which the data collectors were most knowledgeable. In the past, this was found to result in much fewer inadvertent errors. However, as can be seen in the previously presented tables, the resulting raw data was in mixed units. Mass data was recorded in metric units whereas everything else was recorded in British units. This trend was continued throughout this document to ensure that all reduced data and analytical results could be compared directly to the raw data. In all cases, either the metric equivalent or the appropriate multiplicative constant were provided for consistency.

Table 3. Test Condition for the Complete Test Series - Target Definition

Test Number	Brinell Hardness Number (BHN)	Target Thickness (in.)	Areal Density (kg/m <sup>2</sup> )	Test Type
CLG0852	255	12.00	2400	Crater
CLG0853	255	12.00	2400	Crater
CLG0854	267	12.00	2400	Crater
CLG0855	255	12.00	2400	Crater
CLG0856	255	12.00	2400	Crater
CLG0857	321	2.00	400	Spall and Make Screens
CLG0858	364	0.75	150	Spall and Make Screens
CLG0859	302	3.50	700	Spall and Make Screens
CLG0860	340	1.50	300	Spall and Make Screens
CLG0863	340	2.00	400	Spall and Make Screens
CLG0866	321	2.00	400	Spall and Make Screens
CLG0867	321	2.00	400	Spall and Make Screens
CLG0875	340	2.00	400	Spall and Make Screens
CLG0877	321	1.00	200	Spall and Make Screens
CLG0894	364	1.00	200	Make Screens
CLG0919	340	0.75	150	Make Screens
CLG0920	364	0.75	150	Make Screens
CLG0927	321	0.75	150	Make Screens
CLG0928	340	0.75	150	Make Screens
CLG0951	364	0.75	150	Spall Velocity
CLG0952	364	0.75	150	Spall Velocity
CLG0953	364	0.75	150	Spall Velocity
CLG0954	364	1.50	300	Spall Velocity
CLG0955	321	2.00	400	Spall Velocity
CLG0956	340	2.50	500	Spall Velocity
CLG0981	302	2.00	400	Spall Velocity
CLG0982	302	2.50	500	Spall Velocity
CLG0983	321	2.00	400	Spall Velocity
CLG0984	321	2.00	400	Spall Velocity
CLG1003	302	3.00	600	Spall
CLG1004	321	2.50	500	Spall
CLG1013	387	0.75	150	Spall
CLG1014	340	0.50	100	Spall
CLG1015	340	0.50	100	Spall
CLG1016	302	2.50	500	Spall
CLG1017	340	0.50	100	Spall
CLG1018	302	3.00	600	Spall

Note: kg/m<sup>2</sup> - Kilogram per square meter  
in. - Inch = 0.0254 meter

Table 4. Test Condition for the Complete Test Series - Impact Data

Test Number	Penetrator Mass (g)	Impact Velocity (ft/s)	Pitch <sup>a</sup> Angle (deg)	Yaw <sup>b</sup> Angle (deg)	Impact <sup>c</sup> Angle (deg)
CLG0852	501.4	6104	0.00	0.00	0.00
CLG0853	501.7	5976	0.00	0.00	0.00
CLG0854	501.2	5115	2.50	0.00	2.50
CLG0855	501.1	7034	-1.00	0.00	1.00
CLG0856	500.7	8225	0.00	0.00	0.00
CLG0857	501.8	5906	-2.50	0.00	2.50
CLG0858	499.8	6050	0.00	-2.50	2.50
CLG0859	500.4	6168	0.00	-1.00	1.00
CLG0860	501.4	6084	0.00	0.00	0.00
CLG0863	500.3	6424	2.00	-1.50	2.50
CLG0866	501.4	6164	0.00	-1.50	1.50
CLG0867	500.0	6164	-1.50	-5.00	5.22
CLG0875	499.6	6063	0.00	0.00	0.00
CLG0877	501.4	6160	ND	ND	ND
CLG0894	499.4	6000	-3.50	-1.00	3.64
CLG0919	500.9	5814	0.00	1.00	1.00
CLG0920	500.3	5883	2.50	-1.50	4.30
CLG0927	500.0	6093	1.00	-1.00	1.41
CLG0928	500.6	6020	0.00	0.00	0.00
CLG0951	500.0	6138	0.00	0.00	0.00
CLG0952	501.1	6150	1.00	1.50	1.80
CLG0953	500.0	6244	-2.00	-2.50	3.20
CLG0954	500.0	6238	-1.50	-2.50	2.91
CLG0955	500.0	6213	-1.00	-3.00	3.16
CLG0956	500.0	6250	-1.00	-1.00	1.41
CLG0981	501.1	6313	-1.00	0.00	1.00
CLG0982	503.5	6362	0.00	0.00	0.00
CLG0983	503.4	6188	0.00	0.50	0.50
CLG0984	503.0	6300	-1.50	-2.00	2.50
CLG1003	503.7	6163	0.00	0.00	0.00
CLG1004	502.7	6220	-2.50	-2.00	3.20
CLG1013	503.3	6120	-1.00	-1.50	1.80
CLG1014	502.5	6193	0.50	0.00	0.50
CLG1015	503.5	6024	ND	ND	ND
CLG1016	503.5	6207	0.00	0.00	0.00
CLG1017	503.8	6107	ND	ND	ND
CLG1018	501.9	6127	0.00	-1.50	1.50

Note: <sup>a</sup> Measured up (+) or down (-) from shot line

<sup>b</sup> Measured right (+) or left (-) from shot line

<sup>c</sup> Calculated from pitch and yaw angles

$$\text{Impact Angle} = \arctan \sqrt{\tan^2(\text{Pitch Angle}) + \tan^2(\text{Yaw Angle})}$$

ft/s - Feet per second = 0.3048 meter per second

g - Gram

ND - No data available

Table 5. Test Condition for the Complete Test Series - Evaluation Summary

Test Number	DATA				
	Crater	Hole	Panel	Fragmentation	Velocity
CLG0852	G	N	N	N	N
CLG0853	G	N	N	N	N
CLG0854	G	N	N	N	N
CLG0855	G	N	N	N	N
CLG0856	G	N	N	N	N
CLG0857	N	G	G	G	G
CLG0858	N	G	G	G	G
CLG0859	N	G	G	G	G
CLG0860	N	G	G	G	G
CLG0863	N	G	G	G	G
CLG0866	N	G	G	G	B
CLG0867	N	G	G	G	G
CLG0875	N	G	G	G	G
CLG0877	N	G	G	G	G
CLG0894	N	G	N	N	G
CLG0919	N	G	N	N	G
CLG0920	N	G	N	N	N
CLG0927	N	B	N	N	N
CLG0928	N	G	N	N	N
CLG0951	N	B	N	N	G
CLG0952	N	G	N	N	G
CLG0953	N	G	N	N	G
CLG0954	N	G	N	N	G
CLG0955	N	G	N	N	G
CLG0956	N	G	N	N	G
CLG0981	N	G	N	N	G
CLG0982	N	G	N	N	G
CLG0983	N	G	N	N	G
CLG0984	N	G	N	N	G
CLG1003	N	G	G	G	G
CLG1004	N	G	G	G	G
CLG1013	N	G	G	G	G
CLG1014	N	B	G	G	G
CLG1015	N	B	G	G	B
CLG1016	N	G	G	G	G
CLG1017	N	B	G	G	G
CLG1018	N	G	G	G	G

Note: B - Bad  
G - Good  
N - Not applicable

Table 6. Results of the Crater Test Series

Test Number	Depth (in.)	Bulge (in.)	Corrected Depth (in.)	Penetration Depth (in.)	X (in.)	D (in.)
CLG0853	2.48	0.20	2.28	0.00	0.30	3.84
				0.25	0.37	3.66
				0.50	0.46	3.52
				0.75	0.53	3.36
				1.00	0.62	3.20
				1.25	0.75	2.96
				1.50	0.86	2.82
				1.75	1.00	2.46
				2.00	1.29	2.00
				2.25	1.56	1.26
2.50	2.12	0.12				
CLG0854	1.78	0.20	1.58	0.00	0.90	3.22
				0.25	0.80	3.18
				0.50	0.86	3.10
				0.75	1.02	2.86
				1.00	1.15	2.64
				1.25	1.30	2.36
				1.50	1.62	1.62
				CLG0855	2.96	0.18
0.25	1.04	3.58				
0.50	1.08	3.48				
0.75	1.15	3.32				
1.00	1.20	3.30				
1.25	1.18	3.40				
1.50	1.16	3.34				
1.75	1.12	3.26				
2.00	1.36	2.88				
2.25	1.50	2.62				
2.50	1.74	2.12				
2.75	2.12	1.36				
CLG0856	3.80	0.20	3.60	0.00	0.85	3.90
				0.25	0.94	3.90
				0.50	0.99	3.76
				0.75	1.01	3.72
				1.00	0.96	3.76
				1.25	0.96	3.82
				1.50	0.92	3.92
				1.75	1.00	3.66
				2.00	1.10	3.50
				2.25	1.16	3.12
				2.50	1.32	2.84
				2.75	1.52	2.44
				3.00	1.66	2.12
				3.25	1.94	1.84
				3.50	1.16	1.36
3.75	3.02	0.20				

Note: in. - Inch = 0.0254 meter



Table 7. Results of the BAD Test Series - Target Plate, Spall Bundle, and Spall Cap Velocity Data

Test Number	Hole Data			Spall Bundle Data			
	Average Spall Ring Diameter (in.)	Average Spall Ring Depth (in.)	Average PHD (in.)	Holes Panel No. 1	Cone Angle Panel No. 1	Holes Panel No. 2	X-Ray Spall Cap Velocity (ft/s)
CLG0857	3.63	ND	2.63	46	31.34	27	2846
CLG0858	3.10	ND	2.38	128	48.78	56	5295
CLG0859	0.00	0.00	0.00	0	0.00	0	0
CLG0860	3.50	0.78	2.44	115	46.79	61	4229
CLG0863	3.88	0.31	2.53	74	41.70	40	3284
CLG0866	3.86	0.45	2.25	51	42.75	28	ND
CLG0867	4.03	0.34	2.64	74	37.20	38	3267
CLG0875	3.72	0.26	2.29	63	35.32	32	3254
CLG0877	3.18	0.28	2.13	144	40.93	78	5144
CLG0894	3.06	0.26	2.34	NA	NA	NA	5071
CLG0919	2.88	0.21	2.27	NA	NA	NA	5011
CLG0920	3.07	0.16	2.40	NA	NA	NA	NA
CLG0927	2.98	0.24	2.43	NA	NA	NA	NA
CLG0928	2.99	0.22	2.53	NA	NA	NA	NA
CLG0951	ND	ND	2.10	NA	NA	NA	5292
CLG0952	3.15	0.17	2.47	NA	NA	NA	5221
CLG0953	3.09	0.20	2.35	NA	NA	NA	5230
CLG0954	3.57	0.57	2.45	NA	NA	NA	4306
CLG0955	4.01	0.51	2.63	NA	NA	NA	3143
CLG0956	3.99	0.94	2.74	NA	NA	NA	2377
CLG0981	3.90	0.52	2.72	NA	NA	NA	3341
CLG0982	4.01	0.98	2.90	NA	NA	NA	2512
CLG0983	3.91	0.54	2.69	NA	NA	NA	3027
CLG0984	3.88	0.54	2.65	NA	NA	NA	3748
CLG1003	3.75	1.51	2.73	26	34.23	5	1400
CLG1004	4.37	0.92	2.64	ND	ND	ND	2307
CLG1013	3.19	0.15	2.31	142	48.32	64	5373
CLG1014	6.13	0.00	5.80	121	49.02	55	5533
CLG1015	ND	ND	ND	ND	ND	ND	ND
CLG1016	4.66	0.56	2.67	50	45.60	20	2700
CLG1017	7.10	0.07	6.60	100	44.45	45	5613
CLG1018	3.95	0.83	2.80	47	33.52	5	1029

Note: ft/s - Feet per second = 0.3048 meter per second

in. - Inch = 0.0254 meter

NA - Not applicable

ND - No data available



Table 9. Velocity Field Data from Test CLG0982

Fragment Number	Theta <sup>a</sup> (deg)	Velocity <sup>b</sup> (ft/s)	Origin <sup>c</sup> (in.)
1	- 3.08	3821	-0.04
2	5.54	2537	1.30
3	0.52	2579	1.46
4	0.22	2512	1.16
5	- 3.55	2671	-0.33
6	-21.77	2238	1.31
7	4.15	2881	0.33
8	- 0.24	3542	1.01
9	- 8.55	2793	3.83
10	- 2.40	3391	0.52
11	1.11	3356	-0.95
12	22.86	2470	0.00
13	10.59	1989	1.47
14	3.33	2306	1.32
15	17.84	2307	-0.33
16	10.91	2291	0.94

Notes: <sup>a</sup> Measured up (+) or down (-) from shot line  
<sup>b</sup> Measured along fragment path  
<sup>c</sup> Measured up (+) or down (-) from center of exit hole at rear surface of target

ft/s - Feet per second = 0.3048 meter per second  
in. - Inch = 0.0254 meter

Table 10. Velocity Field Data from Test CLG0955

Fragment Number	Theta <sup>a</sup> (deg)	Velocity <sup>b</sup> (ft/s)	Origin <sup>c</sup> (in.)
1	-10.09	3632	-0.21
2	19.09	3377	0.19
3	12.63	3503	1.37
4	- 0.96	3768	-0.65

Notes: <sup>a</sup> Measured up (+) or down (-) from shot line  
<sup>b</sup> Measured along fragment path  
<sup>c</sup> Measured up (+) or down (-) from center of exit hole at rear surface of target

ft/s - Feet per second = 0.3048 meter per second  
in. - Inch = 0.0254 meter

Table 11. Velocity Field Data from Test CLG0953

Fragment Number	Theta <sup>a</sup> (deg)	Velocity <sup>b</sup> (ft/s)	Origin <sup>c</sup> (in.)
1	-0.16	6290	0.13
2	9.00	6369	-5.99
3	2.90	6312	-0.00
4	2.53	6128	0.93
5	10.78	5038	1.48
6	14.55	4868	1.27
7	8.46	4453	1.75
8	3.14	5180	1.31
9	5.13	5979	-1.14
10	2.11	5791	0.11
11	-7.06	5212	-1.59
12	-7.66	5078	-0.48
13	-7.06	5463	1.02
14	-5.93	5944	1.94
15	-4.76	4874	-0.26
16	-4.06	6180	1.54

Notes: <sup>a</sup> Measured up (+) or down (-) from shot line  
<sup>b</sup> Measured along fragment path  
<sup>c</sup> Measured up (+) or down (-) from center of exit hole at rear surface of target

ft/s - Feet per second = 0.3048 meter per second  
in. - Inch = 0.0254 meter

Table 12. Velocity Field Data from Test CLG0956

Fragment Number	Theta <sup>a</sup> (deg)	Velocity <sup>b</sup> (ft/s)	Origin <sup>c</sup> (in.)
1	-3.02	2980	-2.06
2	1.97	2769	0.39
3	-0.74	2377	0.32
4	-4.77	3017	0.34
5	7.15	3216	-4.31
6	-2.19	2663	0.24
7	-0.71	2857	0.02

Notes: <sup>a</sup> Measured up (+) or down (-) from shot line  
<sup>b</sup> Measured along fragment path  
<sup>c</sup> Measured up (+) or down (-) from center of exit hole at rear surface of target

ft/s - Feet per second = 0.3048 meter per second  
in. - Inch = 0.0254 meter

### Crater Characterization

Figure 25 presents the photographs of the various penetrator-generated craters at different impact velocities. All of the targets for the crater studies were composed of two 6-inch (0.1524 meter) thick blocks of RHA. The purpose of these tests was to determine the effect of velocity on the performance of the penetrator so that estimates could be made as to the velocity effect on the BAD data. Figure 26 presents these same tests, but the recorded data were used. The primary point to note was that the shapes of the craters were basically the same. Notice, however, that each of the craters from the recorded data has a flat bottom, whereas the actual craters do not. This variance resulted because the recorded data plots stopped at the corrected depth (measured depth minus bulge). Thus, the more deformed the armor, the more squared off the crater.

The crater comparison shows that the increased velocity has resulted in an increase in the depth of penetration. This is in keeping with the increase in kinetic energy on target. Figure 27 presents a plot of the penetration versus velocity. The dotted line at the top of the plot is the hydrodynamic limit for this penetrator/target condition as determined by the usual square root of the density ratio rule presented as Equation 1-1. Figure 28 presents a plot of the crater volume as calculated from the sectioned target versus the impact kinetic energy. The nearly straight line was as predicted by the theories presented in A Short Course on Penetration Mechanics by Wilbeck, et al. [11].

Using the empirical algorithm presented by Matuska [12] and refined for copper EFPs by Dyess [13], the predicted value of the limit thickness (the thickness which the penetrator will perforate 50 percent of the time) can be determined. The algorithm is

$$t_{\text{lim}} = P_c + 0.4 D_{ss} \quad (4-1)$$

where:

$t_{\text{lim}}$  is the limit thickness

$P_c$  is the corrected penetration depth

$D_{ss}$  is the steady state diameter of the crater

The predicted limit thicknesses determined were 2.68 inches (0.06807 meter) at approximately 5,000 feet per second (ft/s) (1,524 meters per second [m/s]), 3.48 inches (0.08839 meter) at approximately 6,000 ft/s (1,829 m/s) impact (nominal velocity for these tests), 4.10 inches (0.10414 meter) at approximately 7,000 ft/s (2,134 m/s) impact, and 4.99 inches (0.12675 meter) at approximately 8,000 ft/s (2,438 m/s) impact. A plot of these data is presented in Figure 29.

### Basic BAD Characterization

#### General

The purpose of this subsection is to evaluate the effect of armor thickness on the BAD generation of the penetrator under the selected nominal impact condition. For this dissertation, the target areal density is used as the independent parameter and is used for each of the major data displays. Nondimensional parameters were not used for these presentations since Dyess [14] showed that results were highly dependent on the high strain rate material properties of the penetrator and target

materials, and only limited success was achieved when comparing impacts on RHA using copper and pure iron penetrators. To attempt to compensate for the effects of the dynamic properties, the thickness data were nondimensionalized using the limit thickness. This parameter was selected since it was itself a function of these dynamic properties. As long as the penetrator and target materials were not changed and the impact velocities were kept within the range of interest (1.5 to 2.3 km/s) the results were useful for predicative purposes. However, even with these constraints, the predictions were only valid if the targets being considered were from 20 to 80 percent of the penetrator's limit thickness. Attempts to use the same predictions for different materials were less successful. For example, use of the copper/RHA data to predict pure iron/RHA results were, at best, only of limited use.

The basic concept of BAD data can be divided into four classes which are target plate data, spall panel data, spall mass data, and spall cap velocity data. These will be discussed in the subsequent sections.

#### Target Plate Data

Three primary parameters were examined in this section: the profile hole diameter, the spall ring depth, and the spall ring diameter. These parameters were previously defined in Figures 11 and 12. The plots of these three parameters are shown in Figures 30, 31, and 32.

Historically, the thin armor effects were dependent on the tail cone diameter, the medium armor effects were dependent on the confinement of these processes and energy within the armor causing additional erosion and plastic flow, and the final or near-limit thickness armor effects were dependent on the "plugging" of the

armor. This plugging occurred when the terminal energy of the penetrator was just barely sufficient to cause perforation. When this occurred, a final hole, roughly the size of the residual penetrator, was sheared through the remainder of the target.

Similarly, the spall ring was not formed in the thin armor. As the armor thickness increased, the spall ring became wider and deeper. This growth continued until very near the limit thickness, usually 90 percent or higher. At this point, the spall cap spalled off as a solid piece or several large broken pieces, resulting in a large, shallow, flat-bottomed ring. The final or plugging condition had no spall ring.

The presented plots of these data follow the above discussed trends. However, there was considerable scatter in the spall ring depth data. The reason for this scatter can be seen in Figures 33, 34, and 35. Figure 33 presents section photographs of three of the 2-inch (0.0508 meter) targets. In the first case, both sides of the hole show clear formation of the spall ring. However, only one side has completely broken free of the target. In the second case, neither side has completely broken free of the target. The third case shows both sides broken free, but the upper side has been partially closed by the adjacent ring. Figure 34 shows two sections of 2.5-inch (0.0635 meter) targets. In the first case, the spall ring has been formed, but little has broken free. Notice that the ring measured (broken free) was only one of a possible three rings. The second case shows a larger ring which was generated by two of the possible rings breaking free. Figure 35 shows the rear of two of the 3-inch (0.0762 meter) targets. In the first case, a robust, complete ring has been formed and ejected. In the second case, the ring has been formed, but much of the material still remains. The above simply demonstrates the normal variations encountered during testing. All of the targets



were RHA manufactured to the government specification for armor. In several cases, the targets were from the same plate of RHA. However, in the spall ring formation, the local surface condition, the local carbon content, etc., all may play a major role. Naturally, due to the scatter encountered in this portion of the data reduction, a similar scatter was anticipated in the mass data. Fortunately, only a small fraction of the total BAD mass originated from the spall ring for this class of impacts, so the scatter would be less dramatic. The formation of the spall ring, although only a small contributor to the total mass, may contain the information necessary to the understanding of the wave interactions in the spall formation.

Figure 36 presents the sectioned views for a selection of the targets tested. This figure demonstrates the general trends as discussed during the introduction to this subsection.

Note also that the test against the 3.5-inch (0.0889) target did not perforate. The sectioned view as presented in Figure 37 shows the target to be very close to being defeated. This compared well with the value of 3.48 inches (0.08839 meter) calculated from Equation 4-1.

#### Spall Panel Data

Three primary parameters were examined in this section. These were the number of holes in panels 1 and 2 of the spall bundle and the half-cone angle of the spall field as determined by the perforations of the first spall panel. To generate a concept of what these parameters relate to, Figure 38 presents the computer captured data showing the perforations of the first witness panel for the same tests as were presented in Figure 36. This allows an easy correlation as to

the perforation and its result. The data reduced from the raw computer data are then presented as Figures 39, 40, and 41.

#### Spall Mass Data

Spall mass was collected using the spall box discussed previously. All mass recovered was cleaned and sorted according to material. Any fragment of 1 gram or more was individually processed, and the location where it was recovered in the spall box was recorded. The possible recovery locations, in order of the implied increasing energy, would be on the floor of the spall box in front of the spall bundle, between panels 1 and 2 of the spall bundle, between panels 2 and 3 of the spall bundle, between panels 3 and 4 of the spall bundle, and behind the spall bundle. All material particles less than 1 gram from the same recovery area were processed as a composite and labeled as dust. After completion of all data reduction, the material was photographed on a special mat identifying where the fragments had been found and their material nature.

Figure 42 presents the total spall mass recovered as a function of the target areal density. As explained by Dyess [10], the collection technique used for the spall mass recovery was such that all mass in the spall field was recovered with the possible exception of a portion of the residual penetrator. This recovery included both the effective, highly energetic mass, and the slow, ineffective mass. This figure presents a composite of these data.

Figure 43 presents the data generated by counting and weighing the individual recovered spall fragments. Again, as stated by Dyess [10], all spall fragments of 1 gram or more were individually recorded. This figure presents the total of such fragments recovered.

Figures 44 and 45 present the same data as above in a different and more detailed manner. First, the portion of the spall mass which originated as part of the penetrator is shown (Figure 44). Next, the spall mass which was originally part of the target is presented (Figure 45). Finally, the percent of dust is presented in Figure 46 as the percent of the total recovered spall mass. This percentage figure gives an easy indication of the degree of fracture which the armor had undergone. The plot of the nonferrous mass indicates a problem which was mentioned earlier. Some of the penetrator mass was obviously not recovered when thin armor was tested. This mass was in the stopper plates behind the spall bundle and not recoverable.

Just as it was necessary to find a method that would allow for the modeling of the distribution of the various size holes within the spall panel, it was also necessary to find a method of determining the masses of the fragments which made these holes. In general, the holes in the panels were divided into four classes: Class 1, up to 1/4 inch (0.00635 meter) in diameter; Class 2, 1/4 to 1/2 inch (0.00635 to 0.0127 meter) in diameter; Class 3, 1/2 to 1 inch (0.0127 to 0.01905 meter) in diameter; and Class 4, greater than 1 inch (0.01905 meter) in diameter. For example, if our model said that there would be 10 Class 4 holes in a panel and the distribution was given by polar zone, then it was necessary to know what the average mass was of the 10 largest fragments. Then, if the model said 20 Class 3 holes, the average mass of the next 20 largest fragments was needed, etc. The plots used to accomplish this are presented in Figure 47. To obtain this graph, the fragment masses were arranged in descending order. The largest one was then plotted as the 1 fragment. The two largest were then added together and

the average mass was plotted as the 2 fragment. Thus, if the average mass of the 10 largest fragments were desired, simply read across the graph on the 10 fragment line until the appropriate test number was encountered; the average mass is below on the scale.

Of course this technique would have little value unless it were repeatable and could be modeled for other target thicknesses. This is, in fact, the case as is shown in Figure 47. Here data from different tests at different armor thicknesses are plotted. As seen, there is an obvious relationship between these curves. At the thicknesses where repeated tests were made, good correlation exists. As the target thickness increases, the curves move to the right, implying increased fragment size. This fact, of course, has already been demonstrated. Now consider the two thinnest targets (0.50 and 0.75 inch [0.0127 and 0.01905 meter]). Notice how the 0.50-inch (0.0127 meter) target data spreads across the plot for the three cases and how the slopes of the curves are basically the same at the highest number count. The problem here is that the target is severely overmatched. This results in an irregularly formed hole through the thin armor due to pieces being fractured off the armor around the hole. This can also be seen in the hole data (Figures 30 and 32). One large piece broken from the target will shift the entire curve to the right. However, this is not repeatable. To a lesser extent, this problem occurs in the 0.75-inch (0.01905 meter) target curve as well. However, for the thicker targets, the techniques generate repeatable curves. Notice that as the target thickness increases, the basic curve moves to the right; meaning that the average weight of the fragments increase. Also notice that as the target thickness

increases, the slope of the upper portion of the corresponding curves increases slightly. These observations were consistent throughout the range where the target was not severely overmatched (1 inch [0.0254 meter] and higher).

#### Spall Cap Velocity Data

The spall cap velocity was measured for this subsection. This was the velocity of the leading point of the spall field and usually consisted of the residual penetrator fragments mixed with some of the target material. As stated previously, the spall cap velocity was normally used to model the velocities of the rest of the field by employing an approximately parabolic distribution and an energy match. An approximate value for the BAD energy were first calculated by the empirical relationship

$$E_{BAD} = E_I \left( \frac{t_t}{t_{lim}} \right) \quad (4-2)$$

where:

$E_{BAD}$  is the BAD field kinetic energy

$E_I$  is the impact kinetic energy

$t_t$  is the finite target thickness

$t_{lim}$  is the limit thickness.

The spall field was then divided into a series of quarter steradian zones. The central zone was assigned a velocity equal to the spall cap velocity. Each

subsequent zone was assigned a percentage of the spall cap velocity based on the equation

$$v = v_{cap} (\cos \theta)^3 \quad (4-3)$$

where

$v$  is the velocity along the  $\theta$  ray

$v_{cap}$  is the spall cap velocity

$\theta$  is the ray angle from the shotline.

Note that Equation 4-3 provided the velocity along a ray. The band of angles for a given quarter steradian zone were used to get an average velocity in the zone. The total energy of the BAD field was then computed using this velocity distribution and the assumed mass distribution and compared to the energy computed from Equation 4-2. The velocities, as calculated from Equation 4-3, were then modified until a match in the BAD energy using the two techniques was achieved. This process is explained by Flint [3] in more detail including examples of results in vulnerability analyses.

Figure 48 presents the spall cap velocity data as a function of the target areal density. Note that the spall cap velocity is actually presented as a nondimensional parameter by dividing it by the impact velocity. This transaction also negates the small effects caused by the small variations in impact velocity.

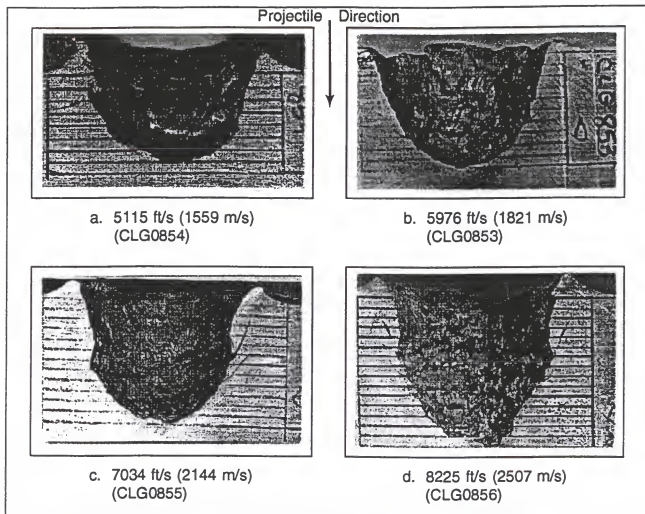


Figure 25. Comparison of the Actual Craters Created by the Penetrator

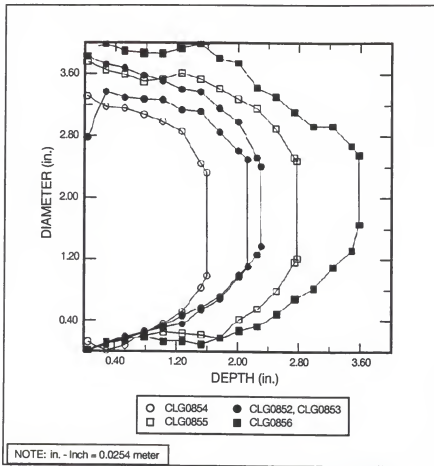


Figure 26. Database Data from the Crater Tests



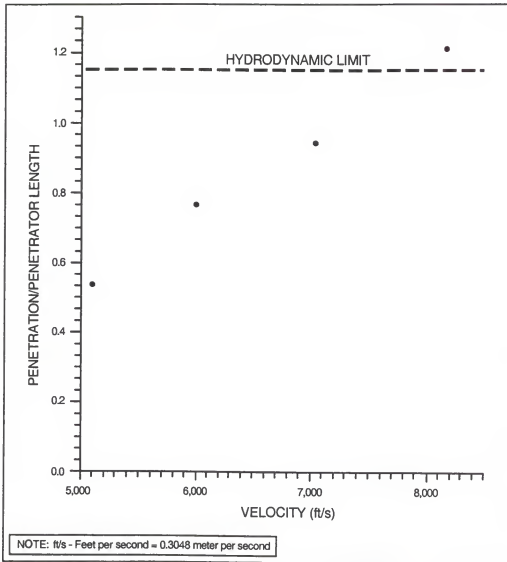


Figure 27. Penetration versus Velocity

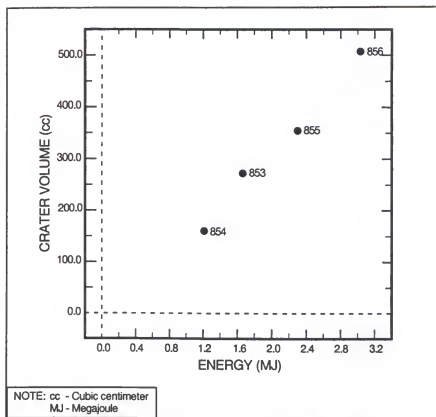


Figure 28. Calculated Crater Volume versus Kinetic Energy

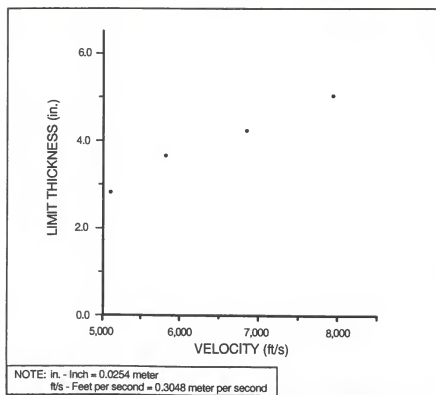


Figure 29. Limit Thickness versus Velocity

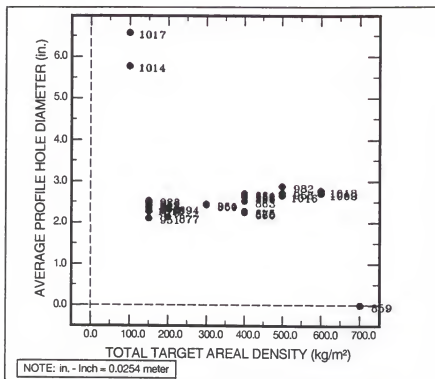
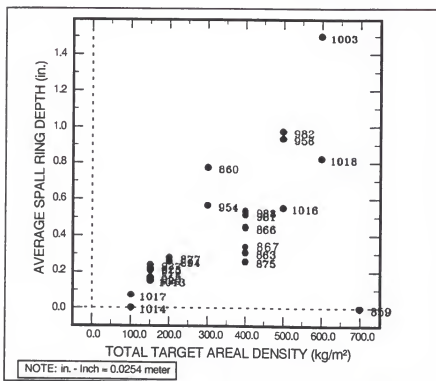
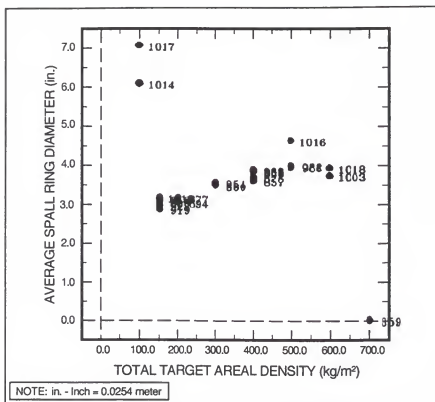


Figure 30. Average Profile Hole Diameter as a Function of the Target Areal Density





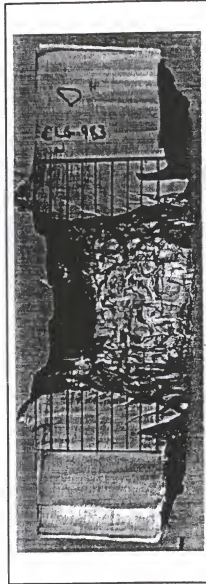
Projectile → Direction



a. Case 1



b. Case 2



c. Case 3

Figure 33. Sectioned Views - 2.0-Inch (0.0508 Meter) Targets

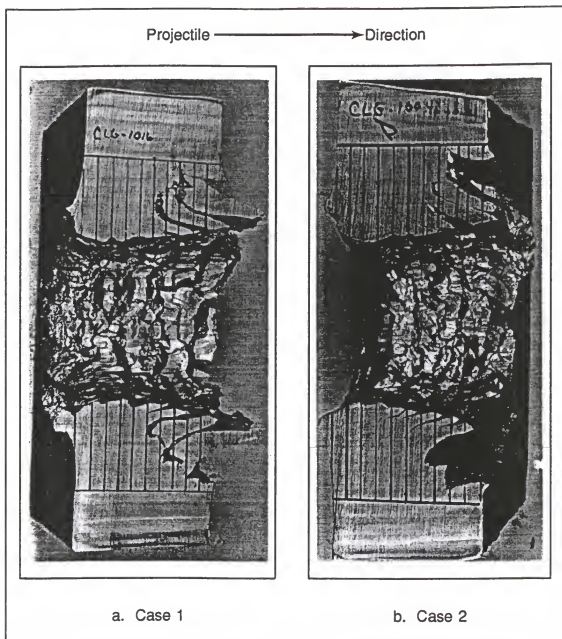
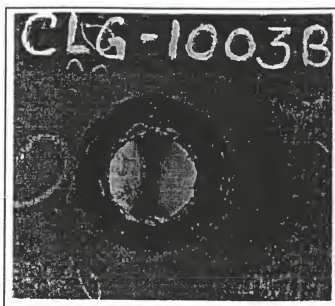
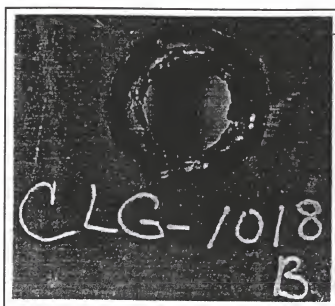


Figure 34. Sectioned Views - 2.5-Inch (0.0635 Meter) Targets



a. Case 1



b. Case 2

Figure 35. Rear View - 3-Inch (0.0762 Meter) Targets

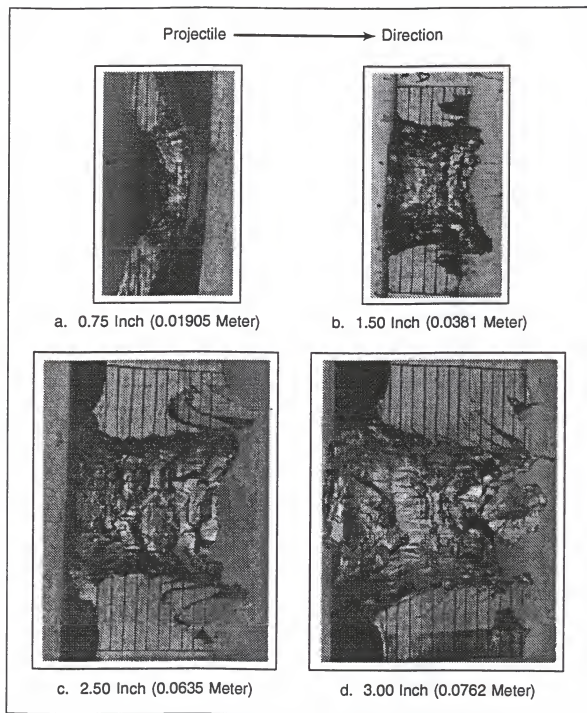


Figure 36. Sectioned View of Selected BAD Targets



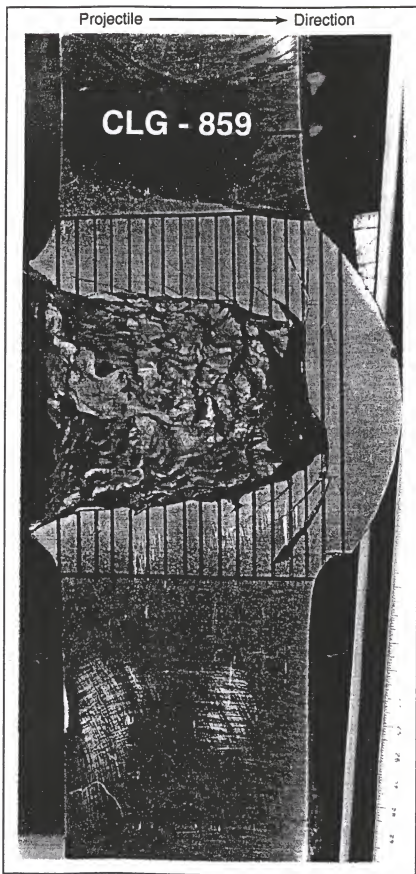


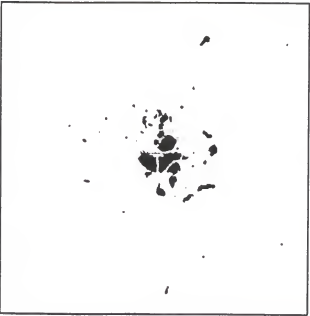
Figure 37. Sectioned View - 3.5-Inch (0.0889 Meter) Target



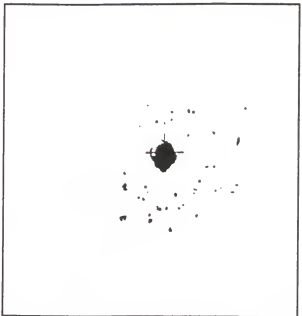
a. 0.75 Inch (0.01905 Meter)



b. 1.50 Inch (0.0381 Meter)



c. 2.50 Inch (0.0635 Meter)



d. 3.00 Inch (0.0762 Meter)

Figure 38. Computer Generated Plot of the Perforations of the First Spall Witness Panel for Selected BAD Tests

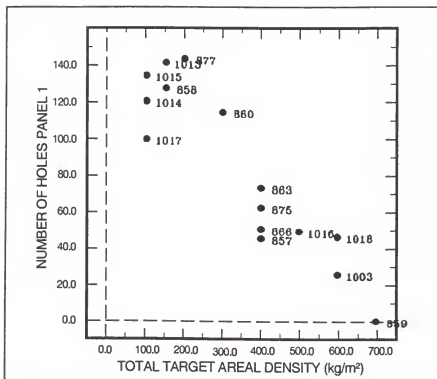


Figure 39. Number of Holes in Panel 1 of the Spall Bundle as a Function of the Target Density

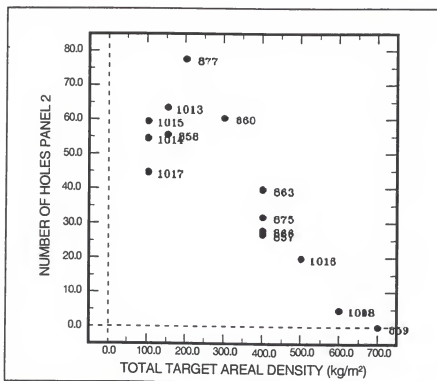


Figure 40. Number of Holes in Panel 2 of the Spall Bundle as a Function of the Target Areal Density

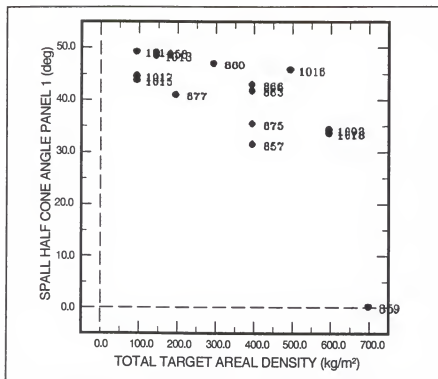


Figure 41. Spall Half-Cone Angle as Measured on Panel 1 of the Spall Bundle as a Function of the Target Areal Density

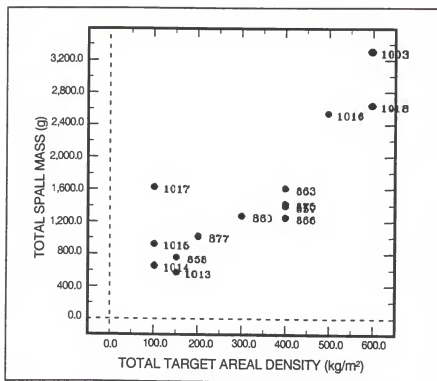


Figure 42. Total Spall Mass as a Function of the Target Areal Density

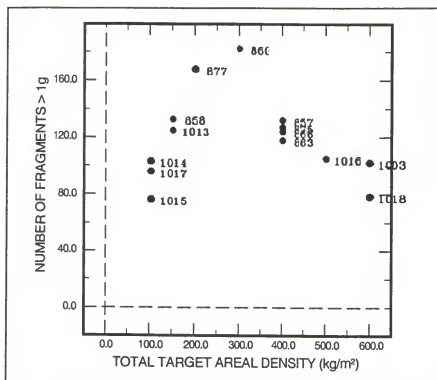


Figure 43. Number of Fragments Whose Mass are Greater Than One Gram as a Function of the Target Areal Density

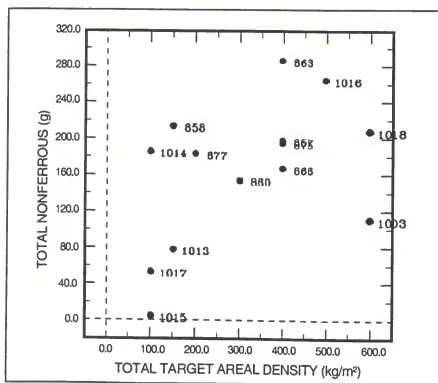


Figure 44. Total Nonferrous Spall Mass as a Function of the Target Areal Density

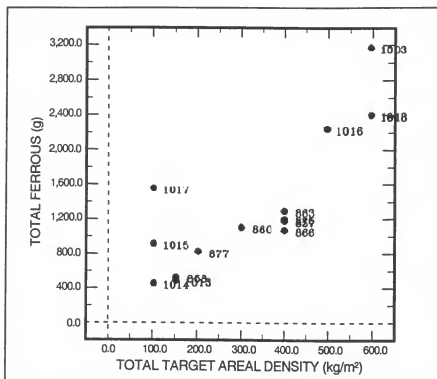


Figure 45. Total Ferrous Spall Mass as a Function of the Target Areal Density

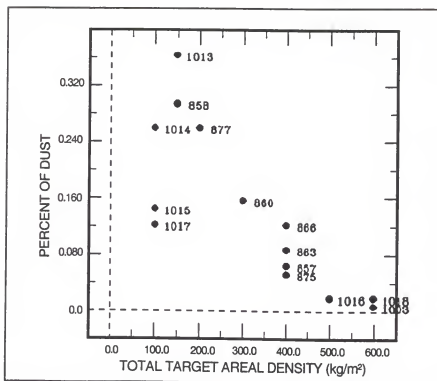


Figure 46. Percent of Dust as a Function of the Target Areal Density

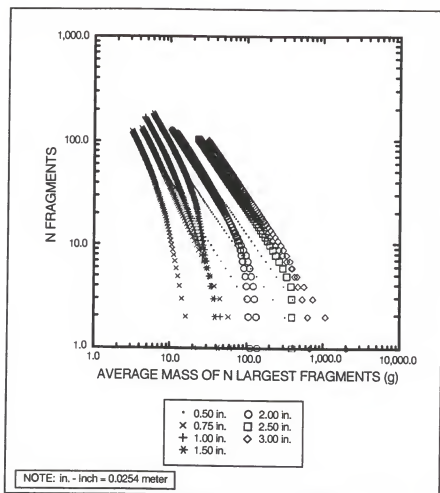


Figure 47. Mass Distribution Plot

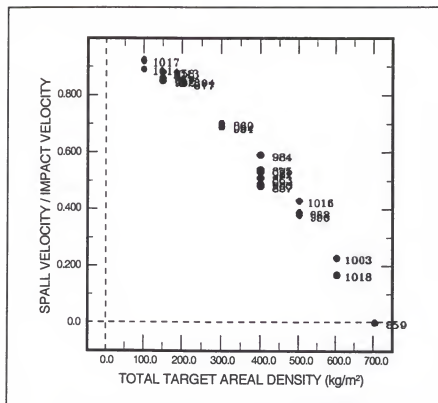


Figure 48. Spall Cap Velocity Expressed as a Percent of the Impact Velocity as a Function of Target Areal Density



### Enhanced BAD Velocity Characterization

#### Method 1: Make Screen Method

The series of tests, which used just the make screens, generated inconclusive data. Because of the destructive nature of the environment and density of the spall fragments within the small area where the measurements were taken, the data were frequently good for only the first fragment through the screens. Thus, at best, the velocity of the leading edge of the spall field was determined. This was not satisfactory. Figure 49 presents a typical set of traces from a front and back screen. Although some data were obtained, there was a significant degree of noise which could have actually been data from a subsequent or simultaneous impact of another fragment.

#### Method 2: Radiographic Method

The slicing technique was developed so that a better understanding of what was transpiring could be gained. With this better understanding, it was hoped that the more complete and complex data generated in the previous tests could be understood. This would eventually lead to a system which could be employed as an addition to the normal test setup without sacrificing any of the required data.

Figures 50, 51, and 52 present a comparison between a standard spall field radiograph taken behind a 0.75-inch (0.01905 meter) target and the radiograph obtained behind the same target for this type of test. In reducing radiographs, the ratio between the distance from the radiographic source to the fragment and the distance from the radiographic source to the film was essential. This ratio was used to determine the position in real space of the fragment shown on the film. If a fragment could be recognized in orthogonal radiographic views then, through an

iterative process, its position could be determined. Figures 50 and 51 illustrate the problems associated with this procedure. Notice the images on the two figures of the spill cap at T2 (time 2). Figure 50 shows a large piece of the spill cap torn loose and following the lead piece. In Figure 51, the shadowing was such that this cannot be seen. This was a simple, but obvious, example of the problems associated with shadowing which make the exact resolution of the position of a fragment difficult, if not impossible. To determine the velocity vector for a fragment, it was necessary to locate the fragment in four views (orthogonal at two times). This increased the difficulty level significantly. Not only does the shadowing problem exist but the fragments were tumbling, thus changing their projected appearance. This can also be seen in Figures 50 and 51. Now consider Figure 52. Since only a defined slice of the BAD field was allowed into the field of view of the radiographics, orthogonal views are not necessary. The ratio of the distances was controlled. Now the makeup of the spill field could be determined. For example, consider the fragment labeled A in Figure 52. Its path can easily be determined. Notice that the tumbling and the different angle of projection has changed its projected shape slightly, but it was still easily recognized, its position in real space easily computed, and its velocity vector easily determined. Notice also the fragments labeled as B in Figure 52. These fragments were easily tracked, as shown, from the T1 to the T2 position. Notice how they have moved apart and, in some cases, changed their projected shapes. The group of fragments labeled as C in Figure 52 illustrate these traits even more succinctly. Figures 53, 54, and 55 present the same comparison for a 2.5-inch (0.0635 meter) target.

Tables 9 and 10 present the findings for the 2.0-inch (0.0508 meter) target. There were significant differences in the fragment velocities, both as a function of

angle ( $\theta$ ) from the shot line, and even along the same  $\theta$  ray. This fact is again shown in Tables 11 and 12 which present the same data for a 0.75-inch (0.01905 meter) and a 2.5-inch (0.0635 meter) target.

Figure 56 presents all of the measured fragment test data and the predicted fragment velocity data from Equation 4-3. As can be seen from this figure, the predicted velocities were generally lower than the actual measured values. This was expected since the predicted values are based on the single bubble assumption. Figure 57 presents this data in a different manner. Here the spatial distribution of the fragments at 500 microseconds are shown along with the predicted position of the bubble from Equation 4-3. Again, the difference between the predicted positions and the actual data is obvious.

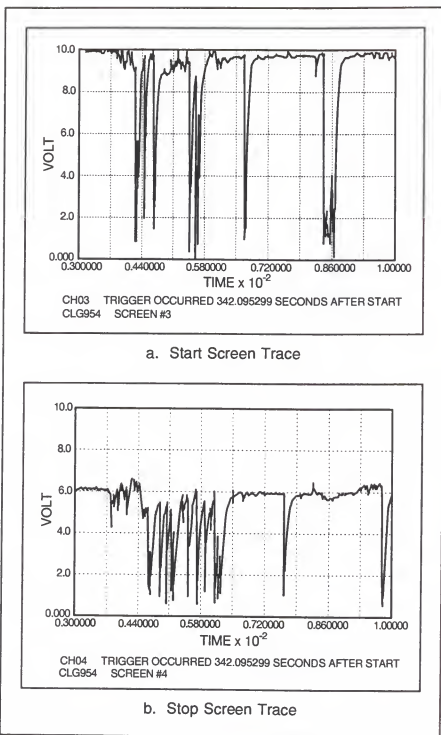


Figure 49. Typical Traces from the Make Screens

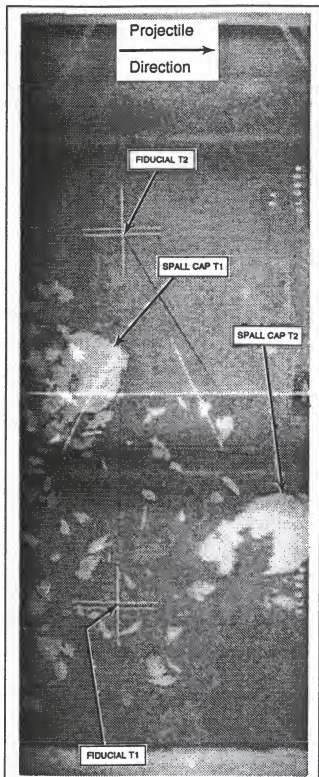


Figure 50. Standard Overhead Radiographic View behind a 0.75-Inch (0.01905 Meter) Target

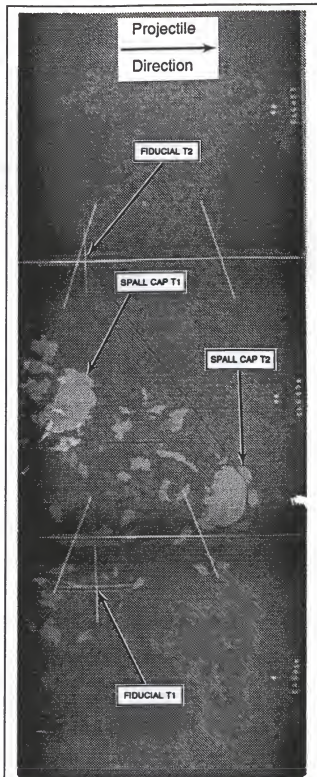


Figure 51. Standard Side Radiographic View behind a 0.75-Inch (0.01905 Meter) Target

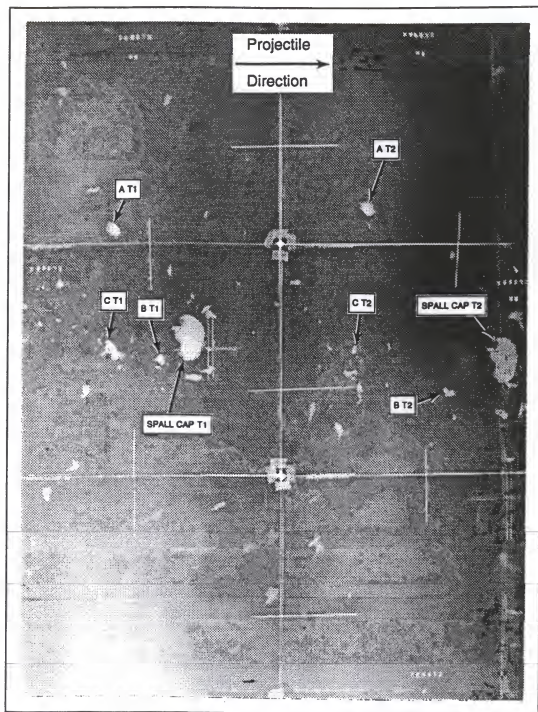


Figure 52. New Side Radiographic View behind  
a 0.75-Inch (0.01905 Meter) Target



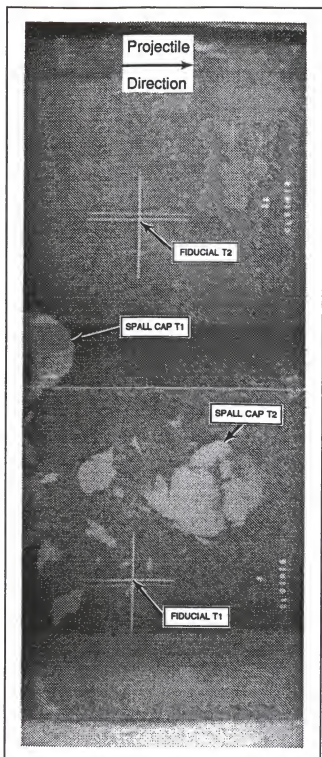


Figure 53. Standard Overhead Radiographic View behind a 2.5-Inch (0.0635 Meter) Target

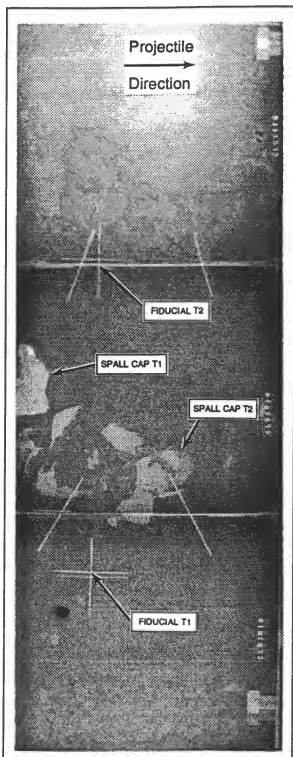


Figure 54. Standard Side Radiographic View behind a 2.5-Inch (0.0635 Meter) Target

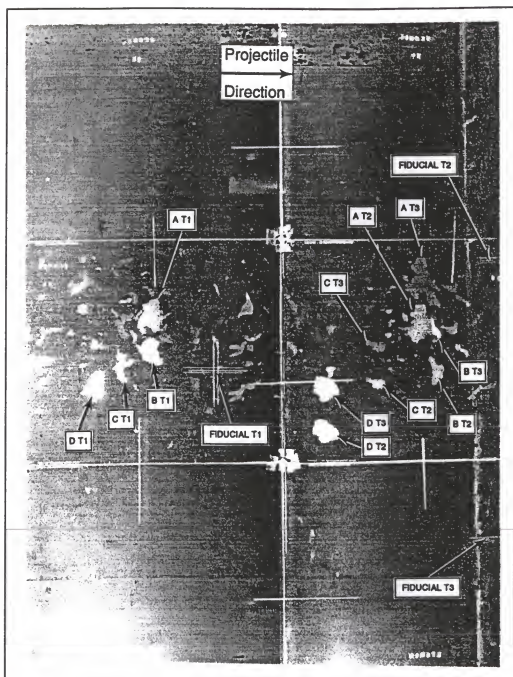


Figure 55. New Side Radiographic View behind a 2.5-Inch (0.0635 Meter) Target



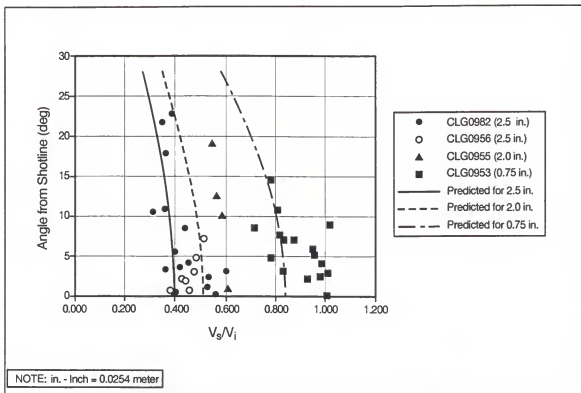


Figure 56. Fragment Velocity Test Data Compared to Single Bubble Predictions

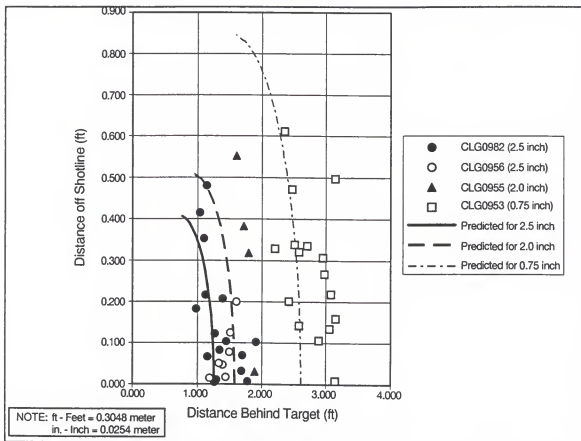


Figure 57. Fragment Spatial Test Data Compared to Single Bubble Predictions

### Chapter Summary

Within this chapter, the penetration and standard BAD characteristics of the penetrator were determined. A technique was presented which sliced the BAD field into a narrow vertical slice. Slices from several tests were analyzed to determine the corresponding BAD velocity fields. If the single bubble theory were true, then no fragments would be observed except on the outer bubble. If the multiple bubble theory were true, then multiple fragments would be observed along a given ray at different velocities. In all cases, significant BAD was found to exist behind the leading bubble. Therefore, the single bubble theory was shown to be invalid.

This information could be employed within the community by statistically varying the velocities within the BAD field. The range of variations would be in the order of 10 percent although values of as much as 30 percent were observed. Note that even a 10-percent change in velocity may have a profound effect on the lethality of a particular fragment, since many of the component vulnerability models are a function of kinetic energy.

The new velocity model will be refined as more test or analytical data become available. Now that the variation in velocity along a ray has been proven, further effort will be expended to develop the make screen method to obtain a statistically significant set of data during normal testing in order to improve the model.

## CHAPTER 5 EULERIAN FINITE ELEMENT MODEL STUDY

### General

The code used in this study was CTH [15]. This commercially available code had a number of constitutive and failure models resident within it [16], [17]. The governing equations for hydrocodes are discussed in Chapter 6. At the conclusion of the crater study, a constitutive model was selected, and the finite armor study was initiated. This effort was primarily a study of the available fracture models and how well they predicted the spall cap velocity. At the conclusion of this phase, a failure model was selected. After the code inputs were validated by comparison to the actual test results, a parametric study was conducted to generate a set of predicted BAD fields. These fields were then evaluated to obtain directly comparable data to that obtained in the various tests.

The objectives of this effort were twofold. First, to attempt to gain a better understanding of where and how the BAD originated and second, to determine if the models could be made to replicate the variation in the velocity field found in the experimental section of this dissertation. If the variation could be replicated, then this process could be used to augment/replace further experimental data needed to develop the necessary statistical model for the velocity field.

## Validation of Code Inputs

### General

The method used in this study was to evaluate the constitutive model applicability by investigating the semi-infinite impact event. The volume, shape, and depth of the resulting predicted crater was compared to the actual crater. A match in depth of the crater would result in a proper match in the percent of the limit thickness for the finite armor study. This match was essential since it greatly affected the resulting spall field. The volume and shape of the crater influenced the amount of mass in the spall field and gave an indication of the energy deposition. Again, for this study, it was considered necessary to match both of these parameters.

### Semi-infinite Armor Characterization

To perform this characterization, four test cases (CLG0854, CLG0853, CLG0855, and CLG0856) in order of increasing impact velocity were duplicated with CTH. The penetrator was modeled geometrically as per Figure 4. This resulted in a calculated mass of 460.477 grams of copper and 37.627 grams of aluminum for a total of 498.104 grams, which was used for all further computations. The penetrator material was annealed copper with a yield strength of 0.024 gigapascal (GPa) [17]. The armor material was RHA with a dynamic yield strength of 0.8 GPa as determined by review of O'Donoghue et al. [18] and Ravid et al. [19].

The grid pattern for the study is presented in Figure 58. In order to determine the "best" match between the CTH runs and the actual tests, a parametric approach was taken. The different conditions evaluated with CTH are as defined in Table 13.

Tables 14 through 17 present the data reduced from these runs as compared to the actual test data recorded. Not all cases were run for each test case, since it was felt not to be necessary. The volumes presented for the CTH runs were calculated in the same manner as those for the test results, by volume of revolution.

CLG0853 represents the test condition where the finite armor effort was conducted (nominal impact velocity of 6,000 ft/s [1,829 m/s]). Therefore, this condition was selected to study the effect of all the cases. Case 1 used the elastic-perfectly plastic constitutive model (see Chapter 6) with the dynamic yield strength of the RHA as found in the Split Hopkinson Bar experiment. This case was run for all crater conditions and found to consistently generate higher crater volumes. Case 2 was run to determine the sensitivity of the crater volume and crater depth to change in the fracture strength of the RHA would have an effect on the crater volume. A 25-percent reduction in the strength was selected. This resulted in approximately a 2-percent increase in volume. The effect was considered a secondary one. Next, the sensitivity of the predicted crater volume and crater depth to a change in the material model was considered. The Johnson-Cook model, a strain hardening model, was selected. This was labeled as Case 4. The effect was a major one, greatly decreasing both the predicted volume (51 percent) and the predicted depth (25 percent). Next, the sensitivity of the

crater volume and crater depth to changes in the dynamic yield strength of the RHA was examined. A 25-percent reduction was considered (Case 5). This resulted in increases in both predicted volume and depth as expected. Using these data, Case 3 was determined. This case had only a small change in the dynamic yield strength of the RHA (6.25 percent increase), and resulted in a reasonable match to the measured test data as can be seen in Table 15. With this information, CTH runs were conducted at the other three test points. All cases as described above were conducted using the axisymmetric stress option.

Figure 59 presents the complete set of data for the crater volume study. Notice that the selected constitutive model (Case 3) resulted in a reasonable match to the test data in the area of interest for the infinite armor evaluation but began to depart from the test data at the upper and lower velocity bounds.

Figure 60 presents the complete set of data for the penetration depth study. The same conclusion as was found for the volume was found for these data. However, unlike the volume where all of the predicted values were higher than the test data, the upper velocity data showed a reversal. It is not unusual for test results to indicate a slight "overshoot" of the hydrodynamic limit before returning to the limit value [20]. However, hydrocodes do not predict this.

The preceding discussion covers two of the three parameters of this section. The final parameter is the shape of the crater. The diameter data from Tables 14 through 17 can be used to evaluate this in part, but a better technique is to view the craters themselves. Figures 61 and 62 present a comparison of the predicted shapes to the test shape for the baseline (CLG0853).

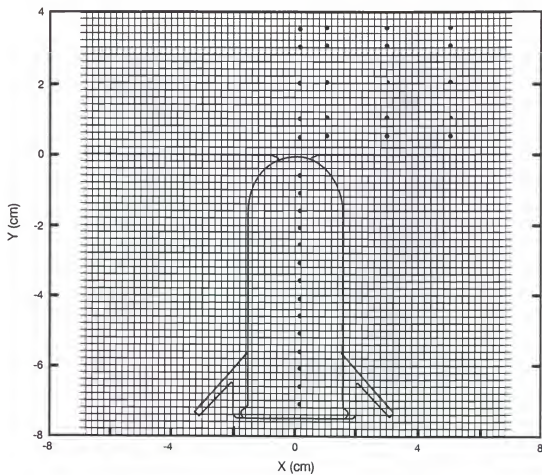


Figure 58. CTH Grid Pattern for Semi-infinite Armor Study

Table 13. Parameter Definition for the Various Cases Evaluated with CTH for the Crater Characterization

Case	Target Thickness (cm)	Constitutive Model	Failure Model	Material Properties					
				Pfrac (GPa)			Yield (GPa)		
				Copper	RHA	Al	Copper	RHA	Al
1	30.48	E-PP	Default	-2.0	-1.300	-2.0	0.024	0.80	0.29
2	30.48	E-PP	Default	-2.0	-0.975	-2.0	0.024	0.80	0.29
3	30.48	E-PP	Default	-2.0	-1.300	-2.0	0.024	0.85	0.29
4	30.48	J-C	Default	-2.0	-1.300	-2.0	0.024	0.80	0.29
5	30.48	E-PP	Default	-2.0	-1.300	-2.0	0.024	0.60	0.29

Note: E-PP - Elastic-Perfectly Plastic model  
 GPa - Gigapascal  
 J-C - Johnson-Cook model  
 Pfrac - Tensile fracture strength

See Chapter 6 for more detail

Table 14. CTH Results Compared to Test CLG0854

Interval	Test	Case 1	Case 2	Case 3	Case 4	Case 5
Diameter at 0.25-Inch Intervals (in.)						
0.00	3.22	3.25		3.19		
0.25	3.18	3.25		3.25		
0.50	3.10	3.28		3.25		
0.75	2.86	3.24		3.19		
1.00	2.64	3.16		3.13		
1.25	2.36	3.00		3.00		
1.50	1.62	2.31		2.69		
1.75	0.76	2.50		2.06		
2.00		1.00				
Depth (in.)	1.58	2.05		2.00		
Difference (%)		29.75		26.57		
Volume (cm <sup>3</sup> )	159.35	223.35		216.90		
Difference (%)		40.16		36.12		

Note: cm<sup>3</sup> = Cubic centimeters  
in. = Inch = 0.0254 meter







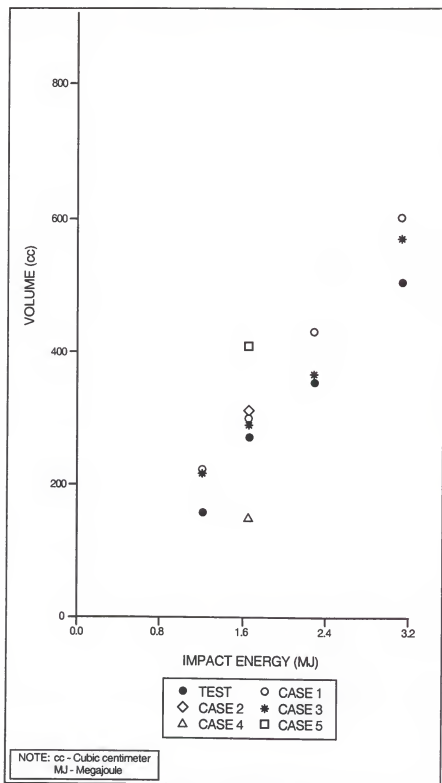


Figure 59. Volume Study

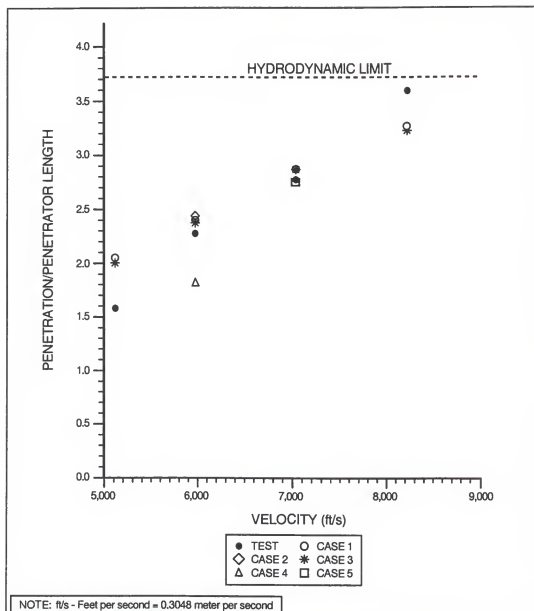


Figure 60. Penetration Depth Study

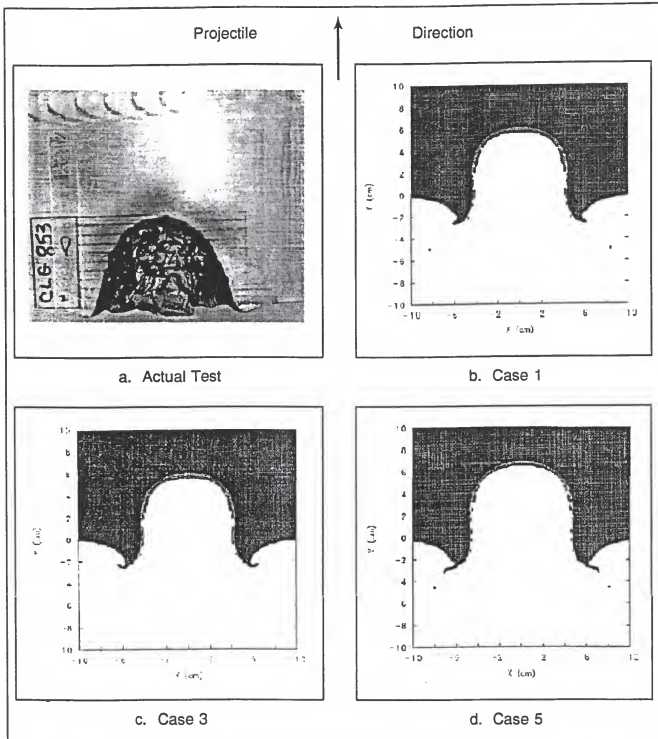


Figure 61. Comparison of the Crater Shape of CLG0853 to Those Predicted by Cases 1, 3, and 5

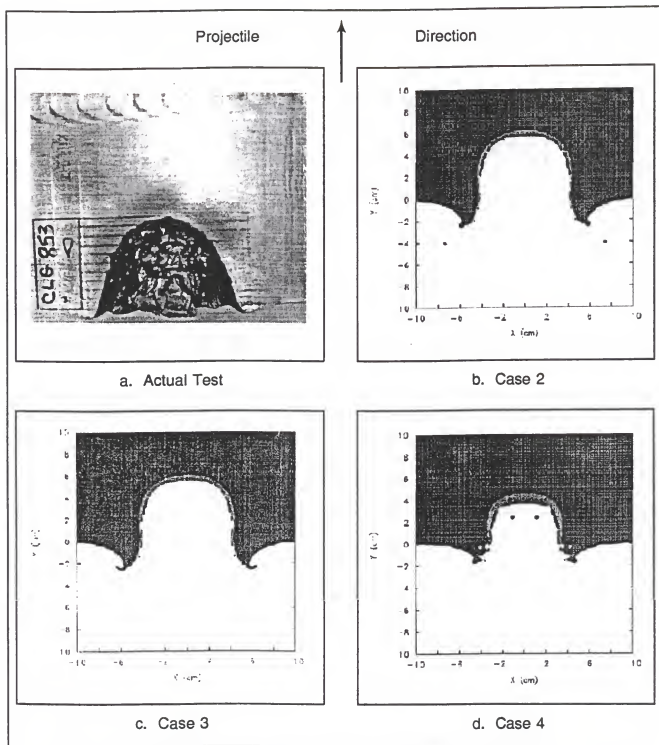


Figure 62. Comparison of the Crater Shape of CLG0853 to Those Predicted by Cases 2, 3, and 4

In Figure 61, the actual crater resulting from the test and the three predictions, where only the yield strength of the armor was changed, are presented. The images in this figure, as well as the similar ones in subsequent figures, were scaled so that they could be directly compared. Figure 62 adds the strain hardening (Johnson-Cook model) and the change to the material fracture value. The primary point which is obvious is that the shape of the test crater has a less hemispherical bottom than do any of the predictions. This implies that the energy deposition for the test is different than that in the predictions. With this exception, the shapes are generally similar, except for the Case 4 which is compressed. Figures 63, 64, and 65 present the test crater and Case 1 and Case 3 predicted craters for the other test conditions. The conclusions reached from review of those figures are the same as stated above.

To ensure that the shape being produced by CTH was not due to the use of the axisymmetric form, a complete three-dimensional run was made. This was accomplished using the Case 4 models and inputs. The resulting crater is presented in Figure 66. There was no change to the basic shape. However, there is significantly more fracture and texture to the surface of the crater. To enhance this presentation, the target portion of the side view was removed so that only the crater remains.

From the discussions above, it was determined that Case 3 was the proper model for calculation at the velocity of interest. It was noted that the ability to predict the test result(s) degenerated as the hydrodynamic limit was approached or as the velocity decreased significantly.

### Finite Armor Characterization

The primary parameter to match in this study was the spall cap velocity. The model determined in the crater study was used, but the dynamic yield strength had to be modified based on the range of Brinell Hardness Numbers (BHN) recorded during the tests. These values were presented in Table 2. Figure 67 presents these data graphically. The ranges were the values encountered in the tests, and the dot represented conditions where only one value of BHN was recorded. For this study only, those tests where the impact angle was less than or equal to 3 degrees were included. The matching values of strength for the BHNs were determined from the Metals Handbook [21]. Figure 68 is a graphical representation of this relationship. The values from the Metals Handbook [21] were for the ultimate strength, not the dynamic yield strength. The rationale/assumptions in using these values directly were as follows:

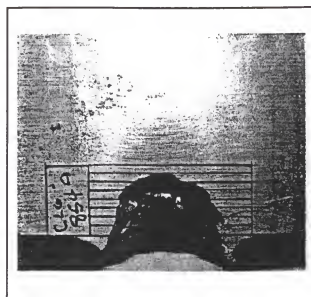
1. The ultimate strength at a BHN of 255 (the average value for the crater work) is approximately equal to the dynamic yield strength found to be correct above.
2. The effect of strain rate would be the same for different thicknesses of the same material.
3. The dynamic yield strength for a thickness of 0.0508 meter, 4340 steel (commercial counterpart to RHA), with a BHN of approximately 340, as reported by Zukas, et al. [20], was approximately 1.17 GPa, which again matched the ultimate strength from the handbook.



4. Therefore, the ultimate (low/no strain rate) strength relationship to BHN would be used as the relationship between dynamic yield strength and BHN.

The CTH grid pattern used for the finite armor series was essentially the same as that used for the semi-infinite study. An example is shown in Figure 69. The line representing the rear of the armor was moved for each thickness.

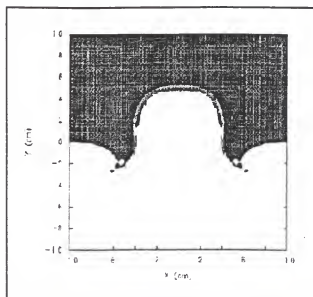
The dynamic yield strength used for the finite armor calculations and the resulting computed spall cap velocities are presented in Table 18. A comparison of the range of spall cap velocities measured from the test to those computed is presented in Figure 70. The match is reasonably good. Thus, the elastic-perfectly plastic constitutive relationship with the dynamic yield strengths taken from Figure 68 (as shown in Table 18) will be used for the final effort.



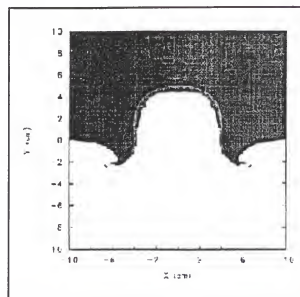
Projectile  
Direction



a. Actual Test



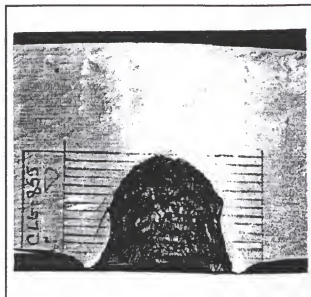
c. Case 1



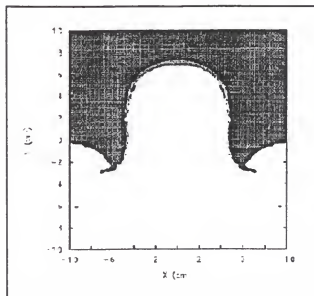
d. Case 3

Figure 63. Comparison of the Crater Shape of CLG0854 to Those Predicted by Cases 1 and 3

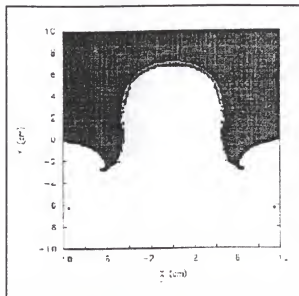
Projectile  
Direction



a. Actual Test

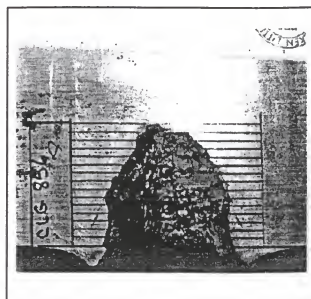


c. Case 1

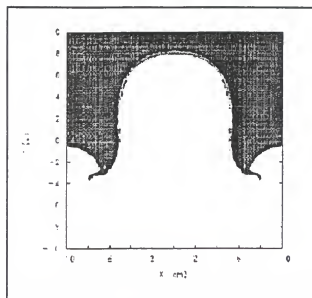


d. Case 3

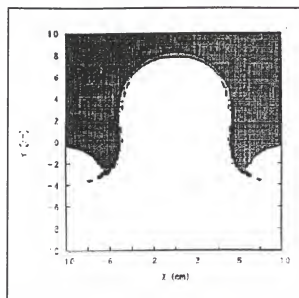
Figure 64. Comparison of the Crater Shape of CLG0855 to Those Predicted by Cases 1 and 3



a. Actual Test

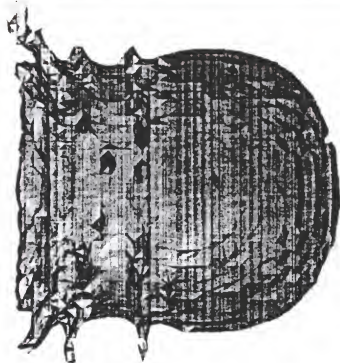


b. Case 1



c. Case 3

Figure 65. Comparison of the Crater Shape of CLG0856  
to Those Predicted by Cases 1 and 3



a. Side View



b. Front View

Figure 66. Predicted Crater Using Case 4 and CLG0853 Models and Values in a 3-D Evaluation

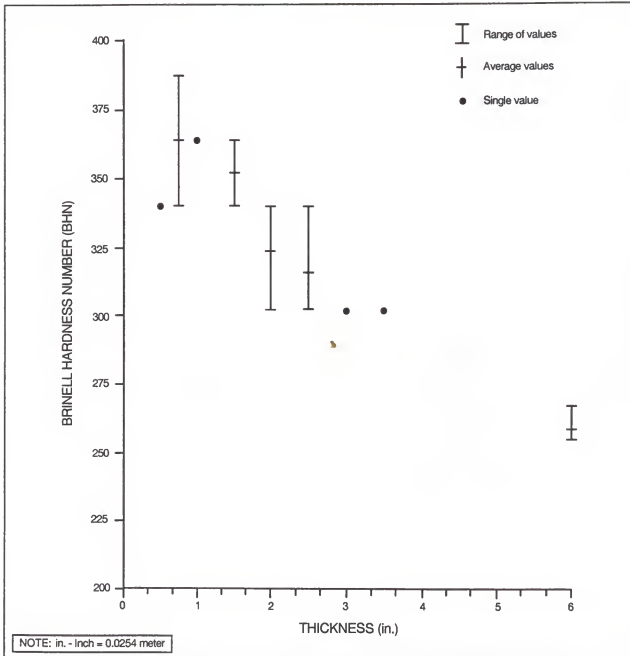
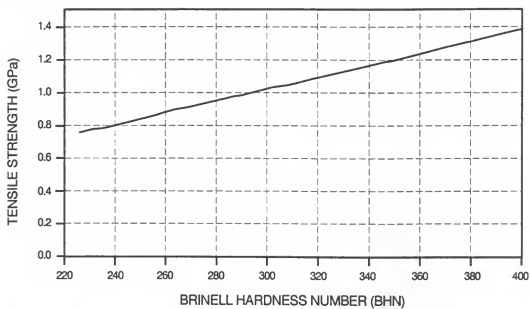


Figure 67. Range of BHN Encountered as a Function of RHA Thickness



REF: ASM METALS HDBK [21]

Figure 68. Ultimate Tensile Strength versus BHN for Steel

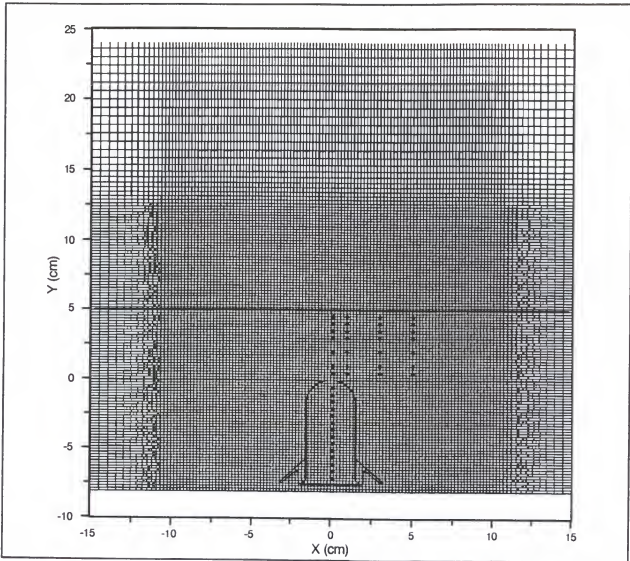


Figure 69. CTH Grid Pattern for Finite Armor Study

Table 18. Finite Target Comparative Data

Test	Measured					Calculated		
	Target Thickness (in.)	BHN	Impact Velocity ( $V_i$ ) (ft/s)	Spall Cap Velocity ( $V_p$ ) (ft/s)	$V_p/V_i$	Ultimate Strength (GPa)	Spall Cap Velocity ( $V_p$ ) (ft/s)	$V_p/V_i$
CLG1014	0.50	340	6193	5533	0.89	1.1720	5967	0.96
CLG0951	0.75	364	6138	5292	0.86	1.2553	5667	0.92
CLG0894	1.00	364	6000	5071	0.85	1.2553	4850	0.81
CLG0960	1.50	340	6084	4229	0.70	1.1720	4200	0.69
CLG0875	2.00	340	6063	3254	0.54	1.1720	2933	0.48
CLG0982	2.50	302	6362	3144	0.49	1.0380	2283	0.36
CLG1003	3.00	267	6163	1400	0.23	0.9123	1383	0.22

Note: ft/s - Feet per second = 0.3048 meter per second  
 GPa - Gigapascal  
 in. - Inch = 0.0254 meter



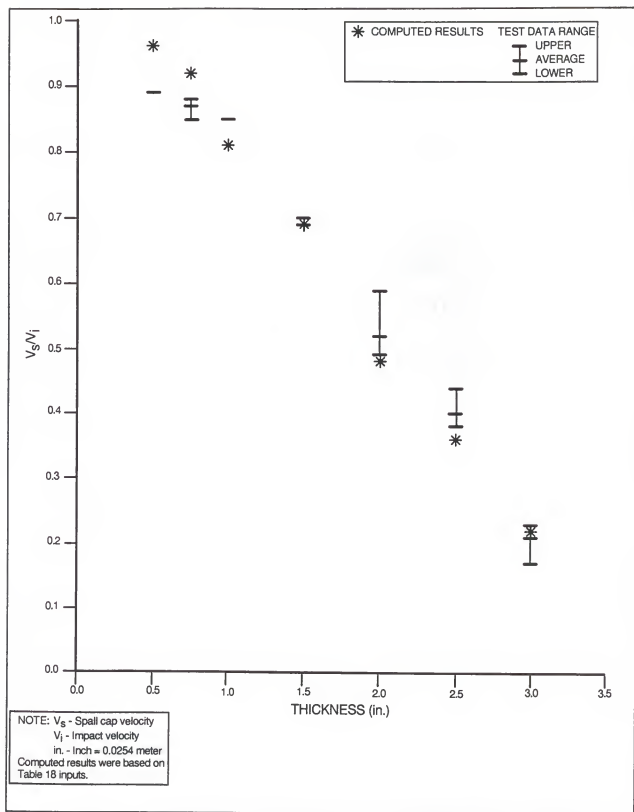


Figure 70. Comparison of Measured versus Computed Spall Cap Velocity

## Comparison of Model Results to Test Results

### General

The method employed in this section was to place multiple tracer points in the CTH grid and track these points throughout the process. The times for the study were extended to allow the particles to reach a point in their travel similar to that space captured by the radiographic technique employed in the tests. A study of each thickness considered in the tests was conducted, and the results are discussed in the following sections. For all studies, in excess of 500 tracer points were placed in the target with another 14 in the penetrator. The purpose of these tracer points was to track the velocity of the various portions of the material.

### Study of 2.50-Inch (0.0635 Meter) Target Impact (Fracture Strength = -1.30 GPa)

The grid used is presented in Figure 71. Figure 72 displays a blowup of this grid with the associated tracer numbers displayed on the edge of the grid. The filled-in grid cells were those where tracer point data were printed for review. However, all tracer point data were saved on the computer file in case subsequent studies were required.

Velocity data for the identified tracer points were then plotted versus time. Figures 73 and 74 present two of the many resulting plots. In the first case, the data are continuous and easily understood. The second figure demonstrates a common problem with using these data when investigating the BAD velocity field. The obvious data instability occurred for two reasons. First, the information for the tracer points was determined using the surrounding material data, insuring continuity. When the material was fractured and some, or all, of the surrounding grid cells were voids, the results became inconsistent. Second, if the grid cell

which contained a tracer point became composed of both material and void (i.e., if the material particle on which the tracer point resided became smaller than a grid cell), then the tracer data "fell out." In either case, data dropout occurred.

Table 19 presents the data acquired from the generated plots for the 500-microsecond time. Note that there are no negative velocities. All of the forward ejecta data have been dropped for one of the reasons stated above.

Figures 75 through 82 present resulting material interface-tracer velocity (MITV) and vector field plots for times of 0, 23, 53, 83, 100, 200, 500, and 1,000 microseconds, respectively, after impact. The MITV is a material interface plot with the tracer particle velocity overlaid. Material interface plots show the line between one material and another or between material and a void. If two fragments, in their travels, come back together, they appear as one. Also, in CTH, when this rejoining occurred, the two were treated as one, as if the fracture never occurred. The flow of the material and the velocity of the material can be easily seen in the earlier plots. Notice the forward ejecta in the early plots and the characteristic spread of the BAD. From the 200-microsecond figure on, the forward ejection has disappeared. The 200-microsecond view is also the first time-view where perforation has occurred. Review of Figures 80, 81, and 82 quickly shows how the tracer velocity data have dropped out as the material particles have spread. Also note that there are two basic parts of the velocity vector field, that tied to the spall cap and that which appears to move outward at about 30 degrees from the spall cap vectors.

To assist in the understanding of these results, the spall cap area of the 1,000-microsecond view was enlarged. Figure 83 presents two different displays

of this area. The first view is the typical material interface plot showing the different materials in the spall cap. The second view is a density plot which was used to attempt to capture all of the material in the area. Material interface plots print the grid cell by determining what material comprises more than half of the cell. Thus, if a grid cell is more than half void, it is printed as a void. The density plot will print this same cell as a reduced density. Thus, a comparison between the material interface plot and the density plot enables better knowledge of the number of small particles involved. Although there were a significant number of particles which were found in this way, the basic shape of the spall cloud material plot did not change.

The results of this computation were conclusive; neither the predicted velocity field nor the spall cloud mass distribution match that found in the test. The maximum velocity does match, as discussed earlier, but the remainder of the field does not. The code predicted a single shell of material expanding at a near constant velocity along a given ray. The data presented in Table 9 for the actual test do not confirm this. The predicted mass was mostly found in a coherent spall cap. In the actual tests, as shown in Figures 53, 54, and 55, the spall cap was not coherent. In fact, it can clearly be seen to be heavily fractured and widely spread.

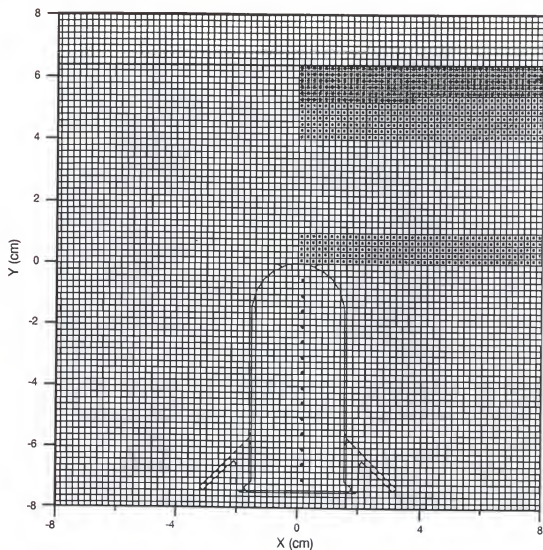


Figure 71. CTH Grid Used for the Simulation of Test CLG0982 (2.50-Inch [0.0635 Meter] Target)

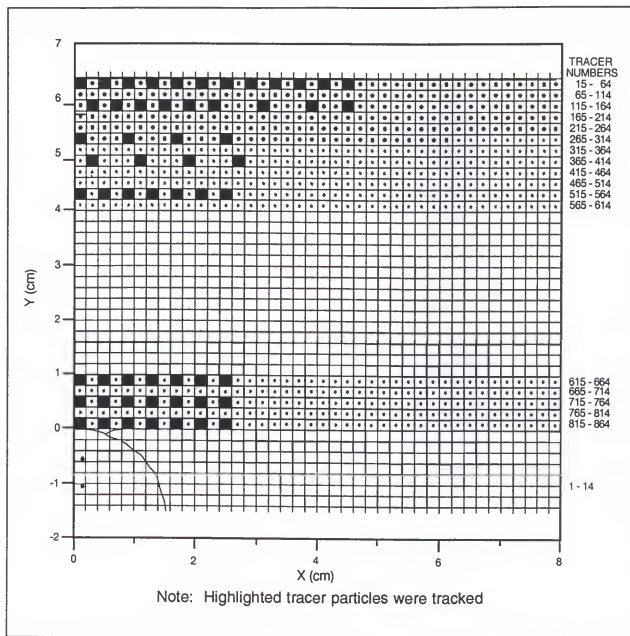


Figure 72. Tracer Particle Pattern for Simulation of Test CLG0982

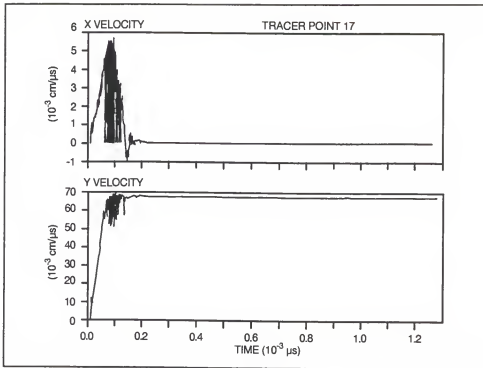


Figure 73. Computed Velocity Plot for Tracer 17 of CLG0982

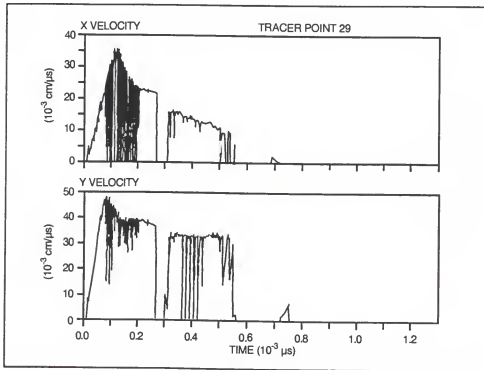


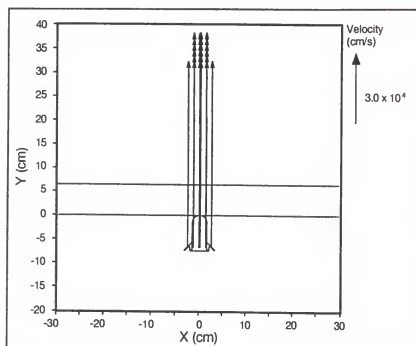
Figure 74. Computed Velocity Plot for Tracer 29 of CLG0982

Table 19. Tracer Particle Velocity, Component Velocities, and Direction Angle at 500 Microseconds from Computation of Test CLG0982 (Fracture Strength = -1.30 GPa)

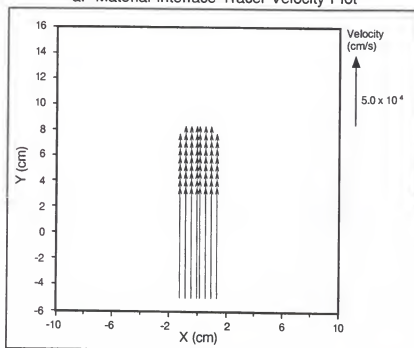
Tracer	$v_x$ (ft/s)	$v_y$ (ft/s)	$v$ (ft/s)	$\theta$ (deg)	Tracer	$v_x$ (ft/s)	$v_y$ (ft/s)	$v$ (ft/s)	$\theta$ (deg)
15	0	2200	2200	0	515	0	2200	2200	0
17	0	2200	2200	0	517	0	2200	2200	0
19	0	2200	2200	0	519	0	2200	2200	0
21	0	2200	2200	0	521	0	2200	2200	0
23	0	2200	2200	0	523	0	2200	2200	0
25	0	2200	2200	0	525	DD	DD	DD	DD
27	DD	DD	DD	DD	527	316	1066	1112	16.51
29	333	1133	1181	16.38					
31	DD	DD	DD	DD	615	0	2200	2200	0
33	0	0	0	0	617	DD	DD	DD	DD
35	0	0	0	0	619	0	0	0	0
37	0	0	0	0	621	0	0	0	0
					623	0	0	0	0
116	0	2200	2200	0	625	0	0	0	0
118	0	2200	2200	0	627	0	0	0	0
120	0	2200	2200	0					
122	0	2200	2200	0	715	0	2200	2200	0
124	0	2200	2200	0	717	DD	DD	DD	DD
126	DD	DD	DD	DD	719	0	0	0	0
130	DD	DD	DD	DD	721	0	0	0	0
134	0	0	0	0	723	0	0	0	0
137	0	0	0	0	725	0	0	0	0
					727	0	0	0	0
265	0	2200	2200	0					
269	0	2200	2200	0	815	0	2200	2200	0
273	0	2200	2200	0	817	DD	DD	DD	DD
277	0	0	0	0	819	0	0	0	0
					821	0	0	0	0
366	0	2200	2200	0	823	0	0	0	0
370	0	2200	2200	0	825	0	0	0	0
374	0	2200	2200	0	827	0	0	0	0
378	333	1133	1181	16.38					

Note: DD - Data drop  
ft/s - Feet per second = 0.3048 meter per second  
 $v_x$  - Velocity in x-direction  
 $v_y$  - Velocity in y-direction  
 $v$  - Total velocity  
 $\theta$  - Angle measure from shot line



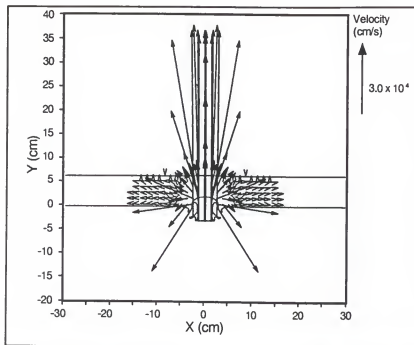


a. Material Interface-Tracer Velocity Plot

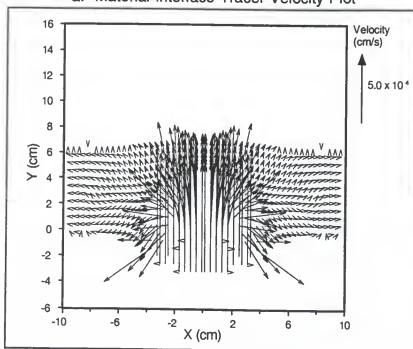


b. Velocity Field

Figure 75. Calculated Velocity Vector Field for CLG0982 at Time = 0 Microsecond (Fracture Strength = -1.30 GPa)

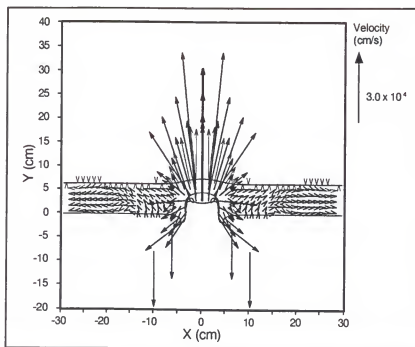


a. Material Interface-Tracer Velocity Plot

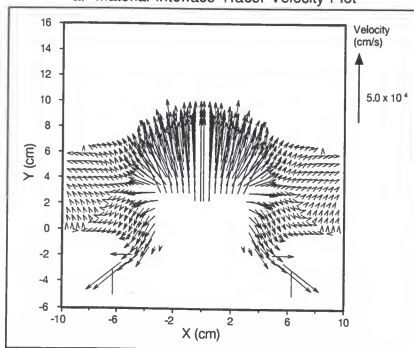


b. Velocity Field

Figure 76. Calculated Velocity Vector Field for CLG0982 at Time = 23 Microseconds (Fracture Strength = -1.30 GPa)

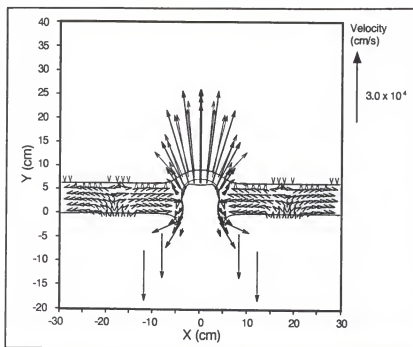


a. Material Interface-Tracer Velocity Plot

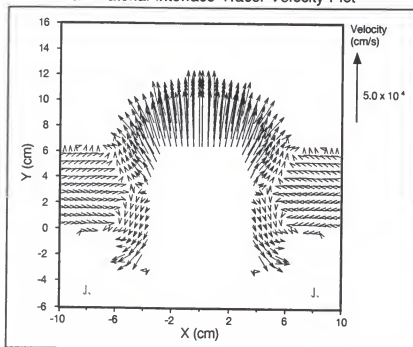


b. Velocity Field

Figure 77. Calculated Velocity Vector Field for CLG0982 at Time = 53 Microseconds (Fracture Strength = -1.30 GPa)

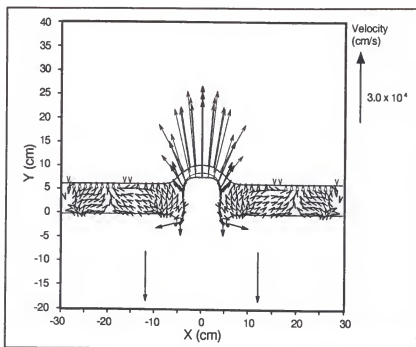


a. Material Interface-Tracer Velocity Plot

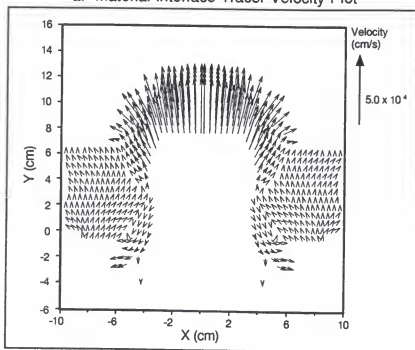


b. Velocity Field

Figure 78. Calculated Velocity Vector Field for CLG0982 at Time = 83 Microseconds (Fracture Strength = -1.30 GPa)

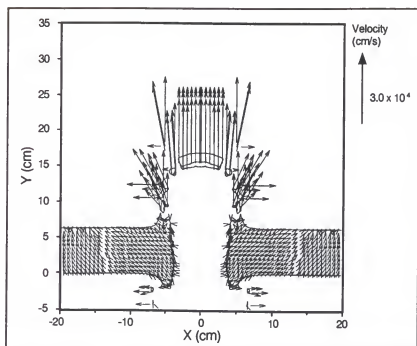


a. Material Interface-Tracer Velocity Plot

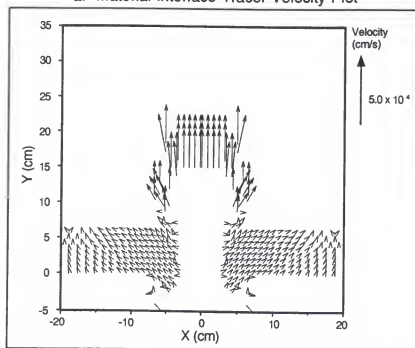


b. Velocity Field

Figure 79. Calculated Velocity Vector Field for CLG0982 at Time = 100 Microseconds (Fracture Strength = -1.30 GPa)

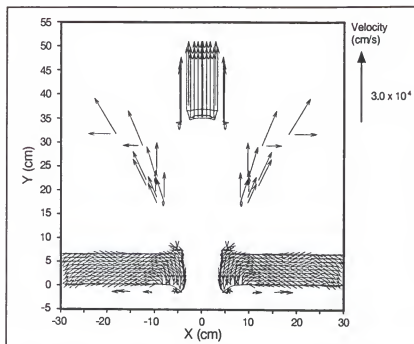


a. Material Interface-Tracer Velocity Plot

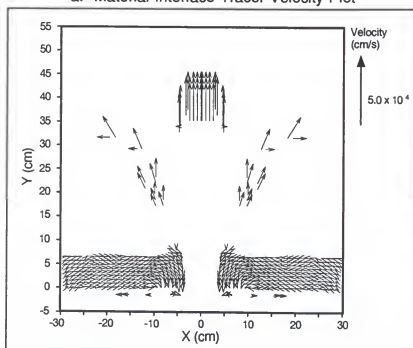


b. Velocity Field

Figure 80. Calculated Velocity Vector Field for CLG0982 at Time = 200 Microseconds (Fracture Strength = -1.30 GPa)

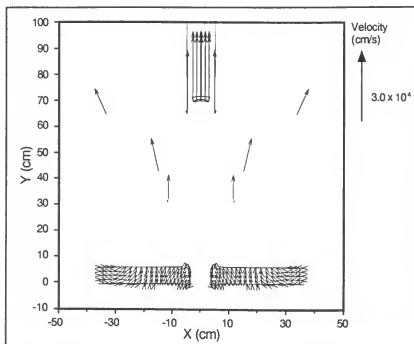


a. Material Interface-Tracer Velocity Plot

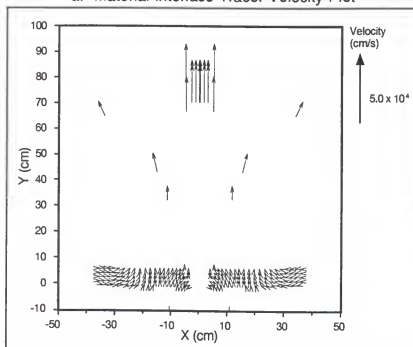


b. Velocity Field

Figure 81. Calculated Velocity Vector Field for CLG0982 at Time = 500 Microseconds (Fracture Strength = -1.30 GPa)



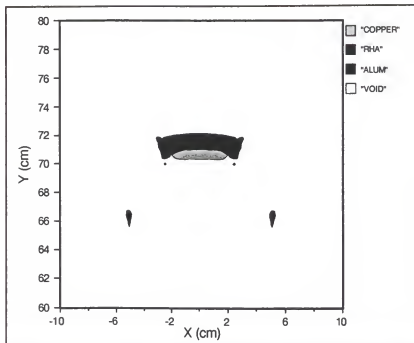
a. Material Interface-Tracer Velocity Plot



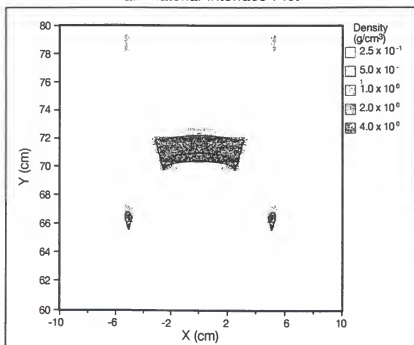
b. Velocity Field

Figure 82. Calculated Velocity Vector Field for CLG0982 at Time = 1,000 Microseconds (Fracture Strength = -1.30 GPa)





a. Material Interface Plot



b. Density Plot

Figure 83. Calculated Spall Cap Area for CLG0982 at Time = 1,000 Microseconds - Enlarged (Fracture Strength = -1.30 GPa)

Study of 2.50-Inch (0.0635 Meter) Target Impact (Fracture Strength = -0.85 GPa)

Discussions with Mr. Leo Wilson of the Wright Aeronautical Laboratory at Eglin Air Force Base, Florida, revealed unpublished data which indicated that the dynamic fracture strength of the armor plate being used was actually -0.85 GPa instead of the code default value of -1.30 GPa. Since the previous study had resulted in a BAD field which was inconsistent with the experimental data, it was decided to reconduct the study with this unpublished value. Table 20 presents the velocity data at 200 microseconds for comparison to Table 19, and most of the previous plots were generated for this study as Figures 84 through 89.

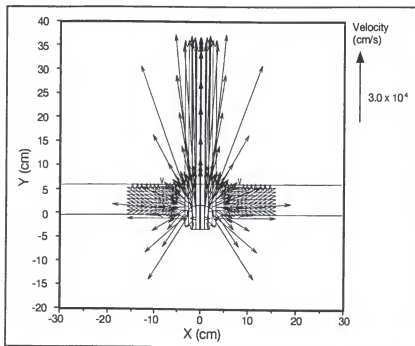
The earlier time for Table 20 was selected due to data dropout at the 500-microsecond time. Due to the lower dynamic fracture strength, the degree of fracture of the target plate was significantly increased resulting in almost all tracer point velocity data being lost prior to the 500-microsecond time.

The results from this study were greatly improved over that previously discussed. Table 20 shows a distinct variation in the tracer point velocities and the MITV plots show that the spall cap has been fractured into many fragments. To better evaluate this, consider Figure 90. In this case, material interface plots are repeated but without the tracer velocity overlay. It can clearly be seen that the BAD is layered instead of being confined to the surface of the bubble. This figure compares much more favorably to Figures 53, 54, and 55 than did the previous study.

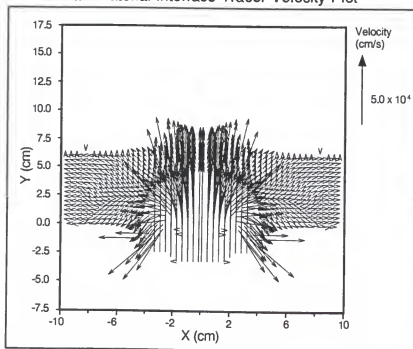
Table 20. Tracer Particle Velocity, Component Velocities, and Direction Angle at 200 Microseconds from Computation of Test CLG0982 (Fracture Strength = -0.85 GPa)

Tracer	$v_x$ (ft/s)	$v_y$ (ft/s)	$v$ (ft/s)	$\theta$ (deg)	Tracer	$v_x$ (ft/s)	$v_y$ (ft/s)	$v$ (ft/s)	$\theta$ (deg)
15	37	2667	2667	0.79	366	157	2650	2655	3.38
17	173	2600	2606	3.81	370	583	2467	2535	13.31
19	400	2600	2631	8.75	374	667	1783	1904	20.50
21	567	2367	2434	13.47	378	633	1600	1721	21.60
23	600	2267	2345	14.83					
25	683	1733	1863	21.52	515	103	2633	2635	2.25
27	800	1733	1909	24.78	517	567	1767	1855	17.79
29	867	1533	1761	29.48	519	0	0	0	0
31	650	1133	1307	29.84	521	0	0	0	0
33	0	0	0	0	523	0	0	0	0
35	0	0	0	0	525	0	0	0	0
37	0	0	0	0	527	0	0	0	0
116	117	2683	2686	2.49	615	117	2667	2669	2.51
118	350	2633	2656	7.57	617	DD	DD	DD	DD
120	533	2600	2654	11.59	619	DD	DD	DD	DD
122	567	2317	2385	13.75	621	DD	DD	DD	DD
124	667	1800	1919	20.32	623	DD	DD	DD	DD
126	883	1767	1975	26.57	625	DD	DD	DD	DD
130	700	1333	1506	27.70	627	DD	DD	DD	DD
134	0	0	0	0					
137	0	0	0	0	715	DD	DD	DD	DD
265	42	2700	2700	0.88					
269	500	2500	2550	11.31					
273	600	1900	1992	17.53					
277	733	1633	1790	24.18					

Note: DD - Data drop  
ft/s - Feet per second = 0.3048 meter per second  
 $v_x$  - Velocity in x-direction  
 $v_y$  - Velocity in y-direction  
 $v$  - Total velocity  
 $\theta$  - Angle measure from shot line

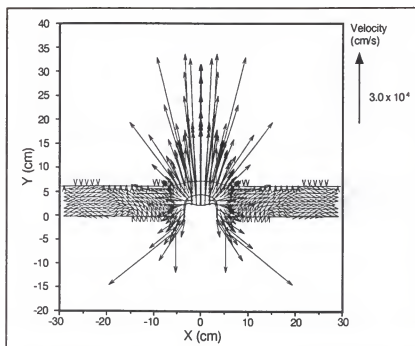


a. Material Interface-Tracer Velocity Plot

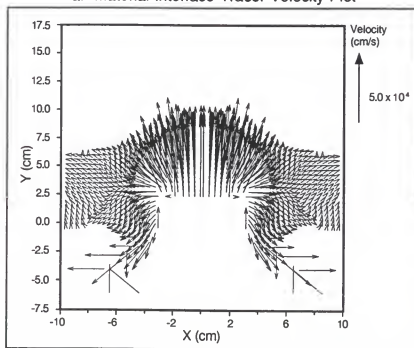


b. Velocity Field

Figure 84. Calculated Velocity Vector Field for CLG0982 at Time = 23 Microseconds (Fracture Strength = -0.85 GPa)

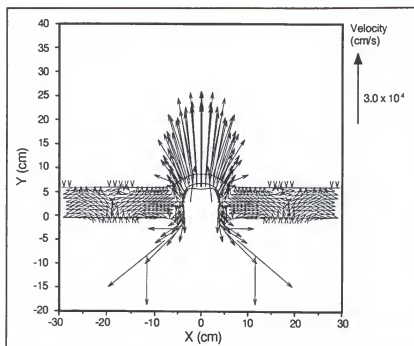


a. Material Interface-Tracer Velocity Plot

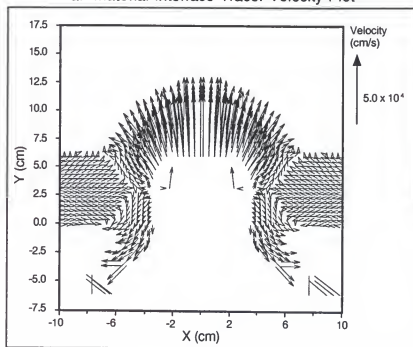


b. Velocity Field

Figure 85. Calculated Velocity Vector Field for CLG0982 at Time = 53 Microseconds (Fracture Strength = -0.85 GPa)

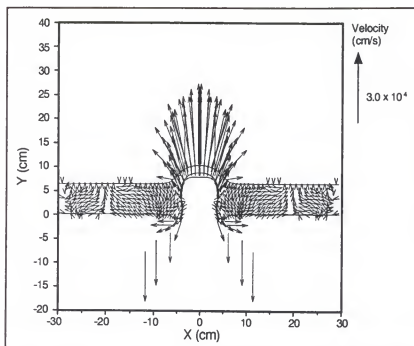


a. Material Interface-Tracer Velocity Plot

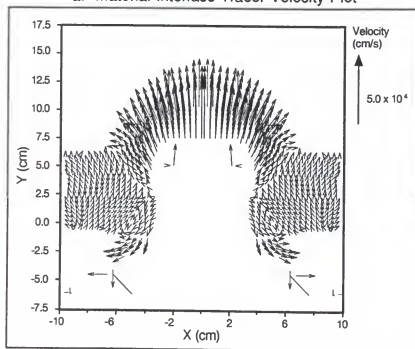


b. Velocity Field

Figure 86. Calculated Velocity Vector Field for CLG0982 at Time = 83 Microseconds (Fracture Strength = -0.85 GPa)

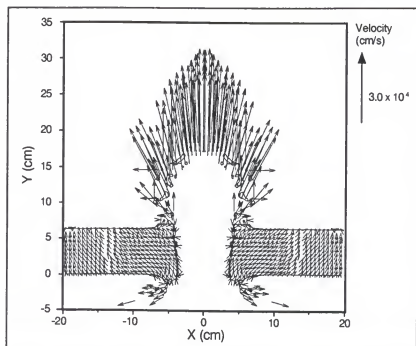


a. Material Interface-Tracer Velocity Plot

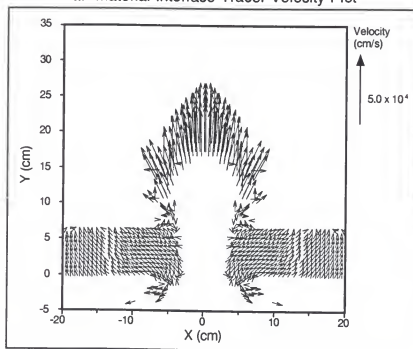


b. Velocity Field

Figure 87. Calculated Velocity Vector Field for CLG0982 at Time = 100 Microseconds (Fracture Strength = -0.85 GPa)



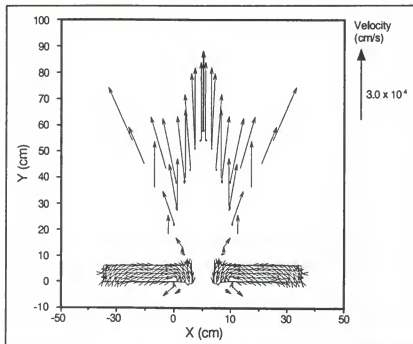
a. Material Interface-Tracer Velocity Plot



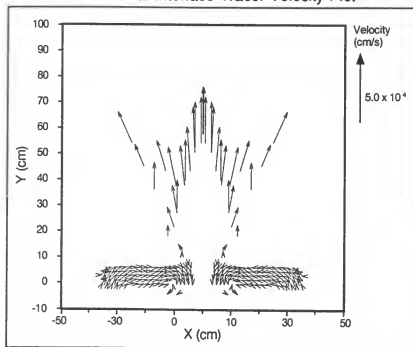
b. Velocity Field

Figure 88. Calculated Velocity Vector Field for CLG0982 at Time = 200 Microseconds (Fracture Strength = -0.85 GPa)



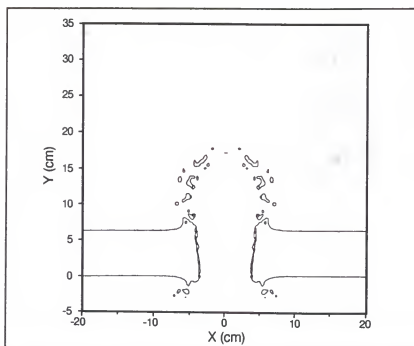


a. Material Interface-Tracer Velocity Plot

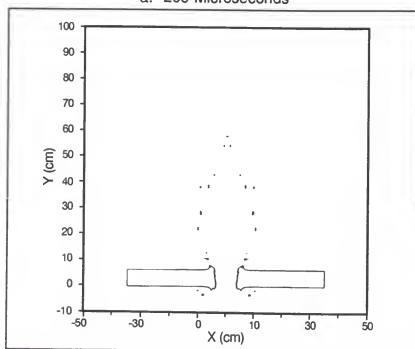


b. Velocity Field

Figure 89. Calculated Velocity Vector Field for CLG0982 at Time = 500 Microseconds (Fracture Strength = -0.85 GPa)



a. 200 Microseconds



b. 500 Microseconds

Figure 90. Calculated Material Interface Plots for CLG0982 (Fracture Strength = -0.85 GPa)

Study of 2.00-Inch (0.0508 Meter) Target Impact (Fracture Strength = -0.85 GPa)

Based on the success of the previous study, the dynamic fracture strength of -0.85 GPa was used for this study. Table 21 presents the calculated tracer point velocities, again at 200 microseconds. A new arrangement of tracer points was required since the armor plate was somewhat thinner. This new arrangement is depicted in Figure 91.

Figures 92 through 97 present the MITV and velocity field plots for 25, 50, 75, 150, 200, and 400 microseconds, respectively. Again, to make the comparison to the radiographic figures, Figure 98 presents just the material interface plots. The BAD was heavily fractured with a variation in velocity within the field.

Table 21. Tracer Particle Velocity, Component Velocities, and Direction Angle at 200 Microseconds from Computation of Test CLG0875 (Fracture Strength = -0.85 GPa)

Tracer	$v_x$ (ft/s)	$v_y$ (ft/s)	$v$ (ft/s)	$\theta$ (deg)	Tracer	$v_x$ (ft/s)	$v_y$ (ft/s)	$v$ (ft/s)	$\theta$ (deg)
15	30	3400	3400	0.51	366	150	3333	3337	2.58
17	233	3300	3308	4.04	370	917	2933	3073	17.36
19	DD	DD	DD	DD	374	900	2267	2439	21.66
21	800	2567	2688	17.31	378	800	1267	1498	32.28
23	900	2500	2657	19.80					
25	867	2100	2272	22.43	515	80	3467	3468	1.32
27	1,167	2067	2373	29.45	517	DD	DD	DD	DD
29	833	1300	1544	32.66	519	0	0	0	0
31	DD	DD	DD	DD	521	0	0	0	0
33	DD	DD	DD	DD	523	0	0	0	0
35	0	0	0	0	525	0	0	0	0
37	0	0	0	0	527	0	0	0	0
116	123	3400	3402	2.08	615	90	3467	3468	1.49
118	417	3167	3194	7.50	617	DD	DD	DD	DD
120	600	2933	2994	11.56	619	0	0	0	0
122	917	2583	2741	19.54	621	0	0	0	0
124	1,000	2267	2477	23.81	623	0	0	0	0
126	1,133	2133	2416	27.98	625	0	0	0	0
130	833	1300	1544	32.66	627	0	0	0	0
134	0	0	0	0					
137	0	0	0	0					
265	38	3467	3467	0.63					
269	700	3000	3081	13.13					
273	917	2500	2663	20.14					
277	583	867	1045	33.95					

Note: DD - Data drop  
ft/s - Feet per second = 0.3048 meter per second  
 $v_x$  - Velocity in x-direction  
 $v_y$  - Velocity in y-direction  
 $v$  - Total velocity  
 $\theta$  - Angle measure from shot line

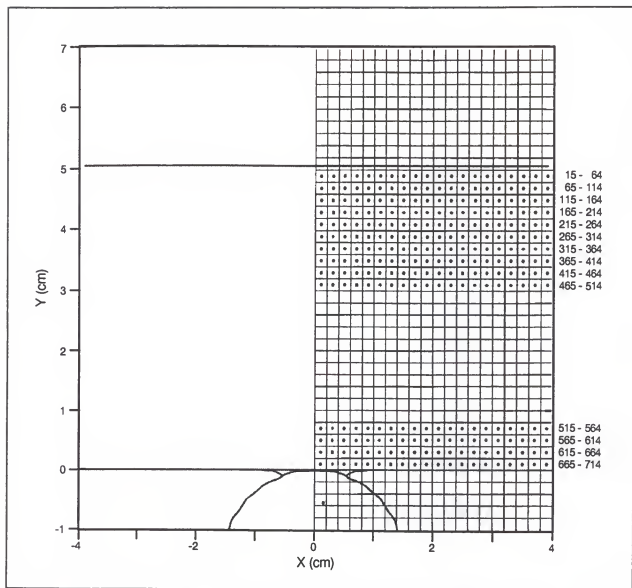
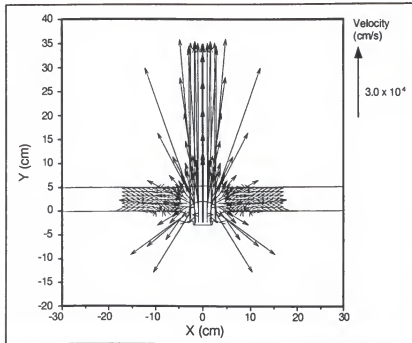
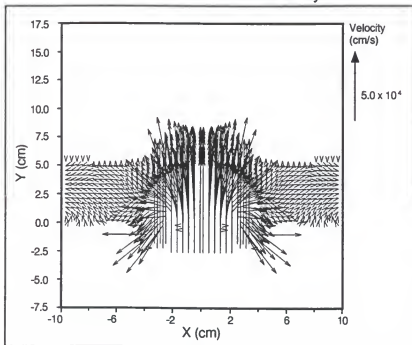


Figure 91. Tracer Particle Pattern for Simulation of Test CLG0875

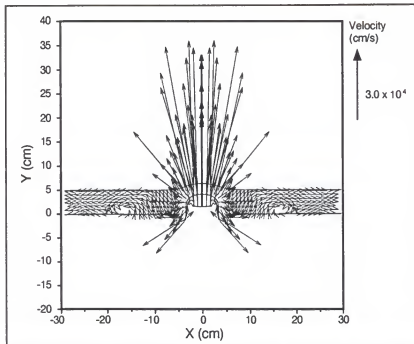


a. Material Interface-Tracer Velocity Plot

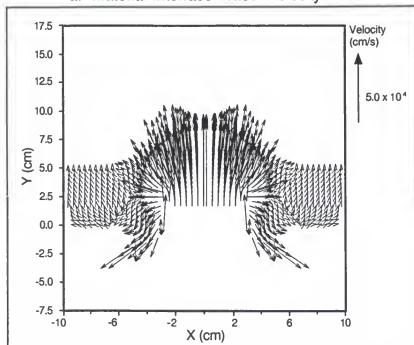


b. Velocity Field

Figure 92. Calculated Velocity Vector Field for CLG0875 at Time = 25 Microseconds (Fracture Strength = -0.85 GPa)

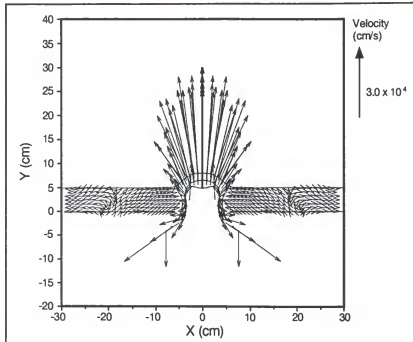


a. Material Interface-Tracer Velocity Plot

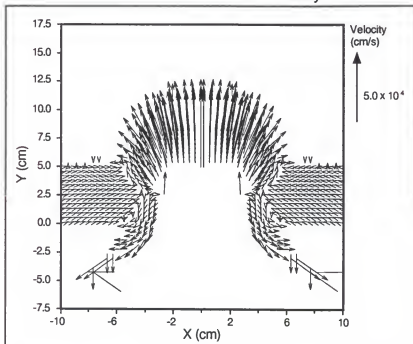


b. Velocity Field

Figure 93. Calculated Velocity Vector Field for CLG0875 at Time = 50 Microseconds (Fracture Strength = -0.85 GPa)



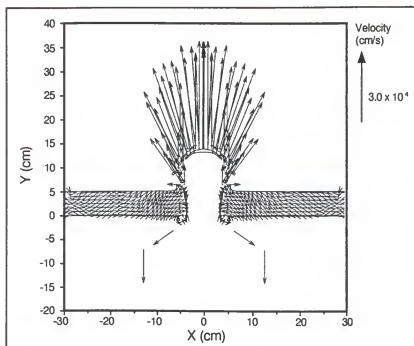
a. Material Interface-Tracer Velocity Plot



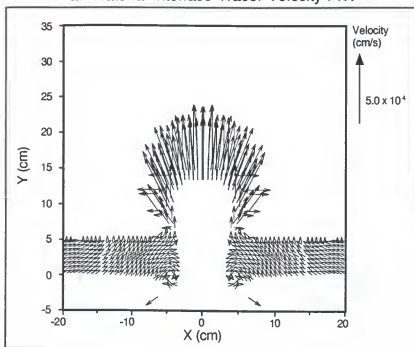
b. Velocity Field

Figure 94. Calculated Velocity Vector Field for CLG0875 at Time = 75 Microseconds (Fracture Strength = -0.85 GPa)



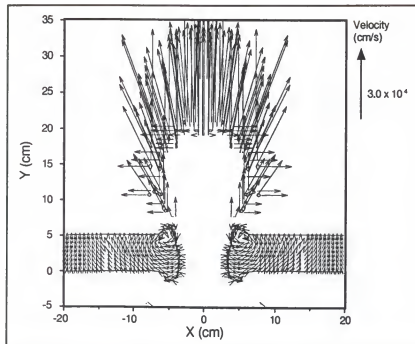


a. Material Interface-Tracer Velocity Plot

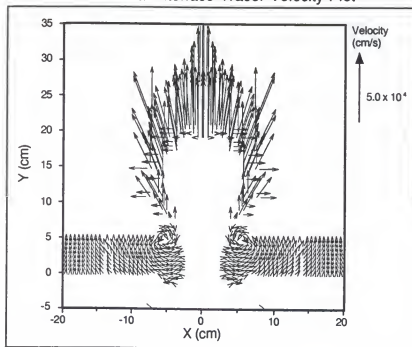


b. Velocity Field

Figure 95. Calculated Velocity Vector Field for CLG0875 at Time = 150 Microseconds (Fracture Strength = -0.85 GPa)

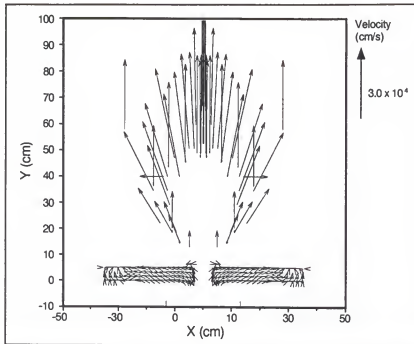


a. Material Interface-Tracer Velocity Plot

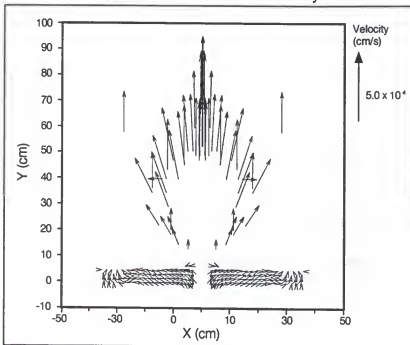


b. Velocity Field

Figure 96. Calculated Velocity Vector Field for CLG0875 at Time = 200 Microseconds (Fracture Strength = -0.85 GPa)

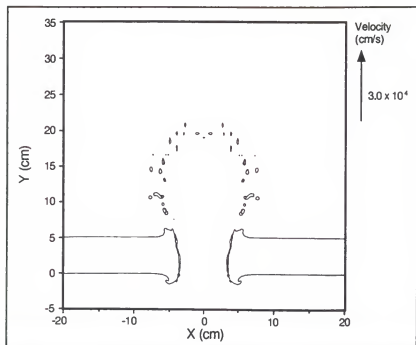


a. Material Interface-Tracer Velocity Plot

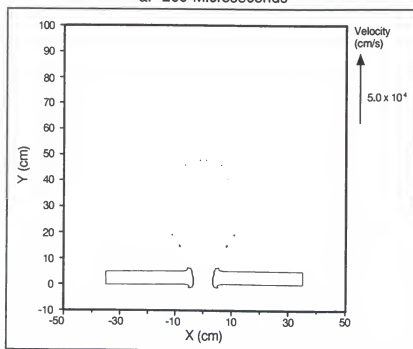


b. Velocity Field

Figure 97. Calculated Velocity Vector Field for CLG0875 at Time = 400 Microseconds (Fracture Strength = -0.85 GPa)



a. 200 Microseconds



b. 400 Microseconds

Figure 98. Calculated Material Interface Plots for CLG0875 (Fracture Strength = -0.85 GPa)

Study of 0.75-Inch (0.01905 Meter) Target Impact (Fracture Strength = -0.85 GPa)

The same technique was used in this study as in the two previous studies. Table 22 presents the calculated tracer point velocities, again at 200 microseconds. Figure 99 presents the tracer point pattern used in this study. Figures 100 through 102 present the MITV and velocity field plots for 25, 50, and 75 microseconds. In this case, the majority of the mass moved along the shot line. In order to display the smaller fragments at the later time, a combination of density and velocity plots (overlaid) were used. Figure 103 shows these plots for 150 and 400 microseconds. Little information was gained from the velocity data since the calculation suffered from severe data dropout, as shown in Table 22. However, comparison of the figures with Figures 50, 51, and 52 did result in some similarities and some differences. The spall cap was represented in all cases as principally intact. However, the experiment resulted in larger, additional fragments. Probably the spall cap was more substantial in the calculations than in the experiment. This would explain where the additional larger pieces came from in the experiments.

Table 22. Tracer Particle Velocity, Component Velocities, and Direction Angle at 200 Microseconds from Computation of Test CLG0951 (Fracture Strength = -0.85 GPa)

Tracer	$v_x$ (ft/s)	$v_y$ (ft/s)	$v$ (ft/s)	$\theta$ (deg)	Tracer	$v_x$ (ft/s)	$v_y$ (ft/s)	$v$ (ft/s)	$\theta$ (deg)
15	60	5583	5584	0.62	265	33	5667	5667	0.34
17	67	5667	5667	0.67	269	DD	DD	DD	DD
19	DD	DD	DD	DD	273	DD	DD	DD	DD
21	DD	DD	DD	DD	277	0	0	0	0
23	DD	DD	DD	DD					
25	DD	DD	DD	DD	366	57	5667	5667	0.57
27	DD	DD	DD	DD	370	DD	DD	DD	DD
29	0	0	0	0	374	0	0	0	0
31	0	0	0	0	378	0	0	0	0
33	0	0	0	0					
35	0	0	0	0					
37	0	0	0	0					
116	57	5667	5667	0.57					
118	DD	DD	DD	DD					
120	DD	DD	DD	DD					
122	DD	DD	DD	DD					
124	DD	DD	DD	DD					
126	DD	DD	DD	DD					
130	0	0	0	0					
134	0	0	0	0					
137	0	0	0	0					

Note: DD - Data drop  
ft/s - Feet per second = 0.3048 meter per second  
 $v_x$  - Velocity in x-direction  
 $v_y$  - Velocity in y-direction  
 $v$  - Total velocity  
 $\theta$  - Angle measure from shot line

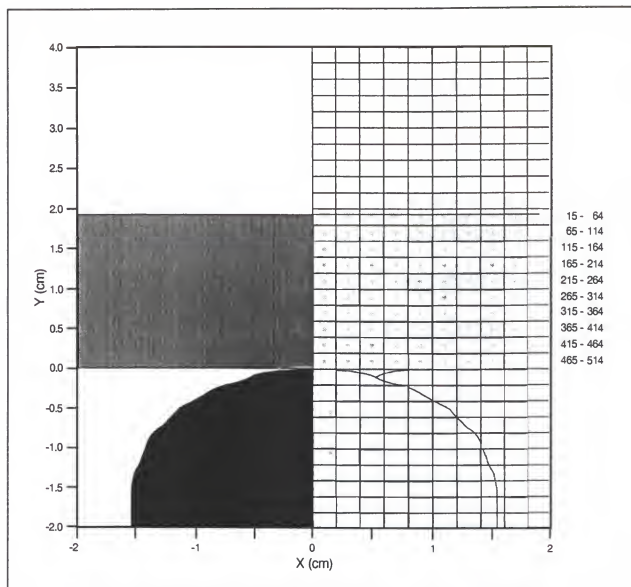
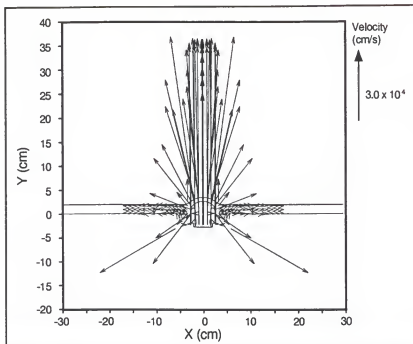
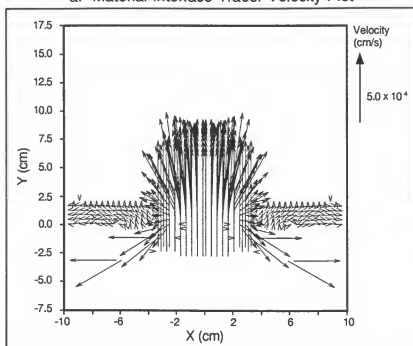


Figure 99. Tracer Particle Pattern for Simulation of Test CLG0951



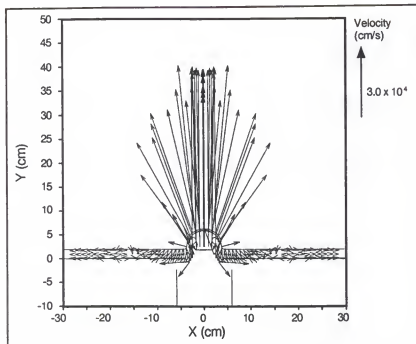
a. Material Interface-Tracer Velocity Plot



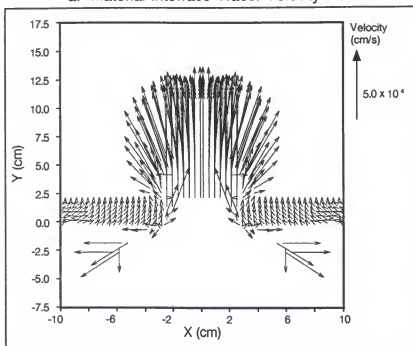
b. Velocity Field

Figure 100. Calculated Velocity Vector Field for CLG0951 at Time = 25 Microseconds (Fracture Strength = -0.85 GPa)



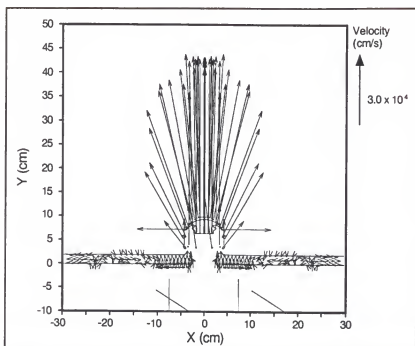


a. Material Interface-Tracer Velocity Plot

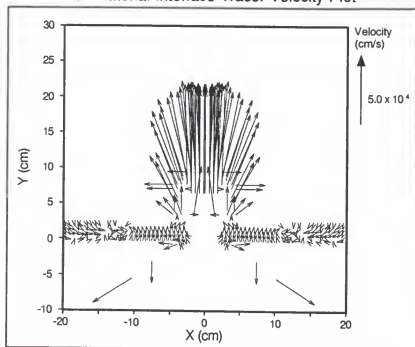


b. Velocity Field

Figure 101. Calculated Velocity Vector Field for CLG0951 at Time = 50 Microseconds (Fracture Strength = -0.85 GPa)

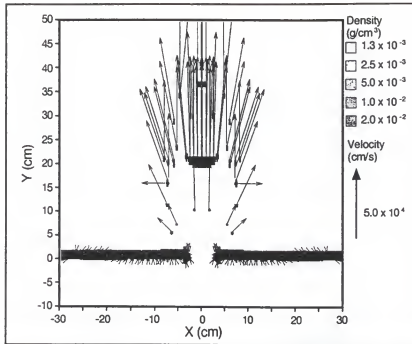


a. Material Interface-Tracer Velocity Plot

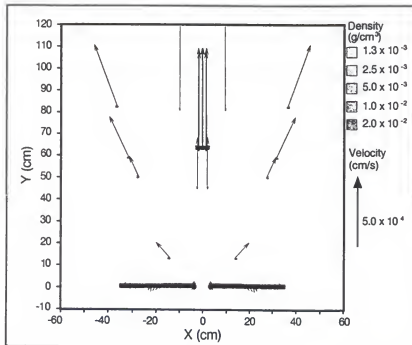


b. Velocity Field

Figure 102. Calculated Velocity Vector Field for CLG0951 at Time = 75 Microseconds (Fracture Strength = -0.85 GPa)



a. 150 Microseconds



b. 400 Microseconds

Figure 103. Calculated Density/Velocity Vector Field for Late Times for CLG0951 (Fracture Strength = -0.85 GPa)

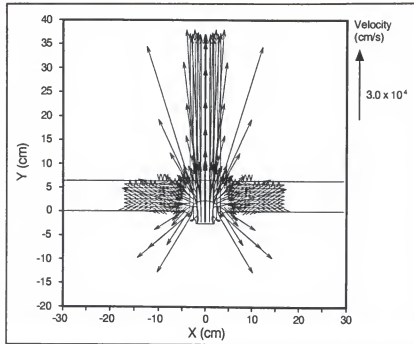
Study of 2.50-Inch (0.0635 Meter) Target Impact (Fracture Strength = -0.50 GPa)

Since the BAD field composition was found to be significantly different for the two dynamic fracture strengths considered, an additional computation was conducted using a further reduced value of dynamic fracture strength. This calculation was for the purpose of further investigating the sensitivity of the BAD results to changes in the dynamic fracture strength. The value used (-0.50 GPa) had no basis in fact. It was selected strictly to have a lower value than what had been previously used. The presentation of data is similar to that in the previous two 2.50-inch (0.0635 meter) target impact studies. Table 23 presents the calculated tracer point velocities at 200 microseconds. The tracer point pattern used was that from Figure 72. Figures 104 through 106 present the MITV and velocity field plots for 25, 75, 100, 200, and 500 microseconds. Again, a material interface plot was generated for easy comparison. Consider Figures 80, 90, and 109. Note that at each decrease in dynamic fracture strength, there was an increase in fracturing effect on the BAD.

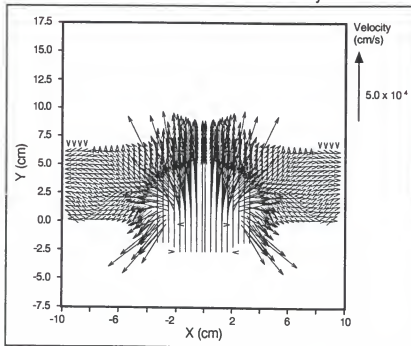
Table 23. Tracer Particle Velocity, Component Velocities, and Direction Angle at 200 Microseconds from Computation of Test CLG0982 (Fracture Strength = -0.50 GPa)

Tracer	$v_x$ (ft/s)	$v_y$ (ft/s)	$v$ (ft/s)	$\theta$ (deg)	$v_x/v_i$	Tracer	$v_x$ (ft/s)	$v_y$ (ft/s)	$v$ (ft/s)	$\theta$ (deg)	$v_x/v_i$
15	37	2667	2667	0.79	0.42	366	100	2667	2669	2.15	
17	133	2600	2603	2.94	0.41	370	500	2400	2452	11.77	0.42
19	533	2667	2719	11.31	0.43	374	1033	1967	2222	27.72	
21	550	2367	2430	13.08	0.38	378	800	1500	1700	28.07	0.39
23	867	2400	2552	19.86	0.40						
25	1,017	1933	2184	27.74	0.34	515	100	2667	2669	2.15	0.35
27	967	1700	1956	29.63	0.31	517	467	1833	1892	14.28	
29	900	1300	1581	34.70	0.25	519	0	0	0	0	0.27
31	667	933	1147	35.54	0.18	521	0	0	0	0	
33	583	467	747	51.34	0.12	523	0	0	0	0	
35	0	0	0	0	0	525	0	0	0	0	0.42
37	0	0	0	0	0	527	0	0	0	0	
											0.30
116	83	2667	2668	1.79	0.42	615	100	2667	2669	2.15	0
118	300	2567	2584	6.67	0.41	617	700	1533	1686	24.54	0
120	433	2567	2603	9.58	0.41	619	0	0	0	0	0
122	867	2433	2583	19.61	0.41	621	0	0	0	0	0
124	1,000	1967	2206	26.95	0.35	623	0	0	0	0	0
126	967	1767	2014	28.69	0.32						
130	667	1133	1315	30.47	0.21						
134	0	0	0	0	0						0.42
137	0	0	0	0	0						
											0.26
265	40	2667	2667	0.86	0.42						0
269	417	2400	2436	9.85	0.38						0
273	967	2033	2251	25.43	0.35						0
277	800	1533	1729	27.55	0.27						

Note: ft/s - Feet per second = 0.3048 meter per second  
 $v_x$  - Velocity in x-direction  
 $v_y$  - Velocity in y-direction  
 $v$  - Total velocity  
 $\theta$  - Angle measure from shot line

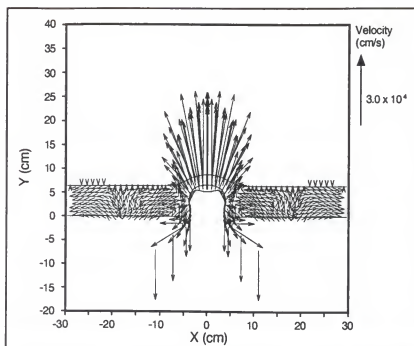


a. Material Interface-Tracer Velocity Plot

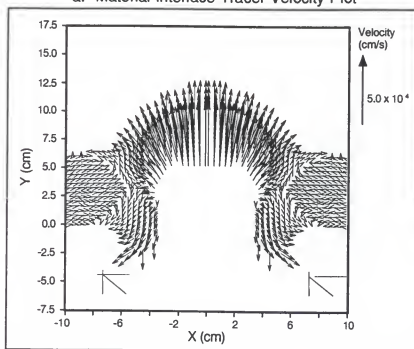


b. Velocity Field

Figure 104. Calculated Velocity Vector Field for CLG0982 at Time = 25 Microseconds (Fracture Strength = -0.50 GPa)

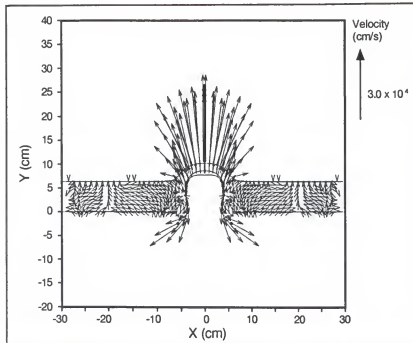


a. Material Interface-Tracer Velocity Plot

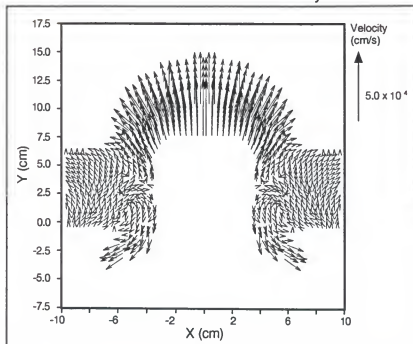


b. Velocity Field

Figure 105. Calculated Velocity Vector Field for CLG0982 at Time = 75 Microseconds (Fracture Strength = -0.50 GPa)



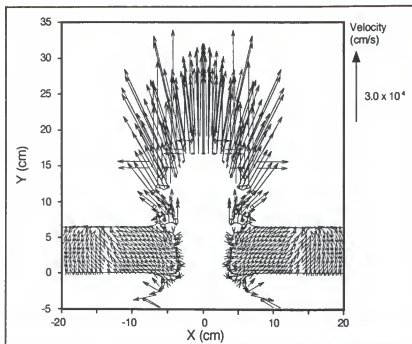
a. Material Interface-Tracer Velocity Plot



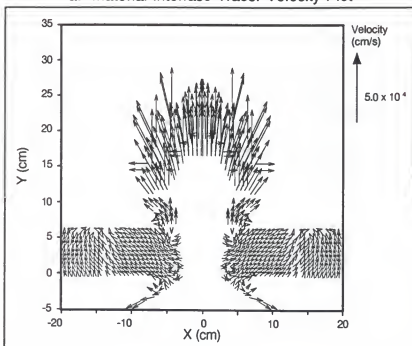
b. Velocity Field

Figure 106. Calculated Velocity Vector Field for CLG0982 at Time = 100 Microseconds (Fracture Strength = -0.50 GPa)



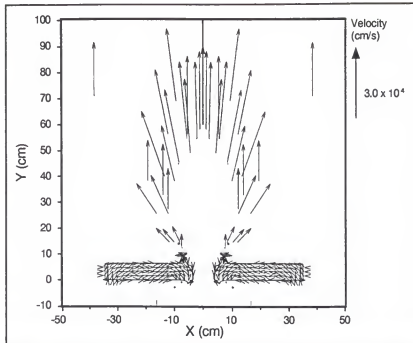


a. Material Interface-Tracer Velocity Plot

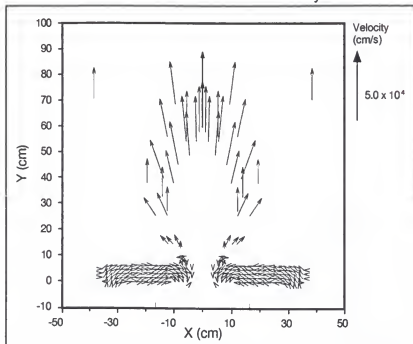


b. Velocity Field

Figure 107. Calculated Velocity Vector Field for CLG0982 at Time = 200 Microseconds (Fracture Strength = -0.50 GPa)

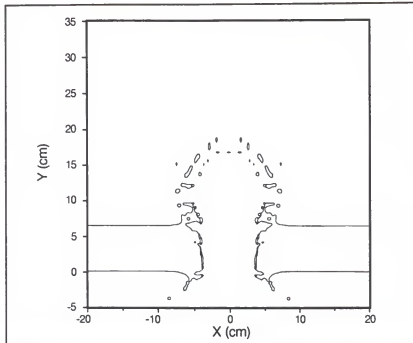


a. Material Interface-Tracer Velocity Plot

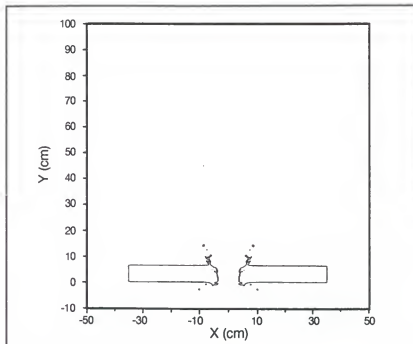


b. Velocity Field

Figure 108. Calculated Velocity Vector Field for CLG0982 at Time = 500 Microseconds (Fracture Strength = -0.50 GPa)



a. 200 Microseconds



b. 500 Microseconds

Figure 109. Calculated Material Interface Plots for CLG0982 (Fracture Strength = -0.50 GPa)

### Chapter Summary

A commercially available hydrocode was found to be able to replicate the test results except for the crater shape. For the other aspects of the infinite armor crater study, the selected input values matched the test results only in a relatively narrow range of impact velocity (1.8 - 2.1 km/s). Reduction in the dynamic yield strength to allow for a lower strain rate condition would enable a match at the lower velocity condition (~1.5 km/s). The upper velocity condition (~2.4 km/s) could not be matched since the hydrocode theory will not allow penetration beyond the hydrodynamic limit (Equation 1-1).

The finite armor study resulted in an encouraging match to the test data. However, the importance of the dynamic fracture strength is paramount. By varying this value, results could be obtained which simulate the single bubble theory or the multiple bubble theory. In this study, values of -1.30, -0.85 and -0.50 were examined where the two first values have basis. However, these are not the only values reported in the literature. For example, Wilbeck, et al. [11] found that best results were achieved when the dynamic fracture strength for RHA was used as -5.8 GPa, Hertel [22] found a value of -2.5 GPa for RHA to work best, and Kmetyk and Yarrington [23] used -20 GPa. Obviously, this variation means that the true nature of this parameter remains to be determined.

## CHAPTER 6 HYDROCODE THEORY

### Background

The previous chapter dealt with the application of a specific hydrocode. In this chapter, a brief overview of hydrocodes will be presented. Hydrocodes were used to solve problems in all three of the impact regimes as outlined in Figure 3. However the problems associated were quite different. In region I, the geometry of the structure as well as the material behavior were important. The projectile was basically nondeforming, other than bending and some local erosion. This was a region best characterized with structural dynamics behavior. In region II, both the projectile and the target behavior were characterized by inertia with material strength and failure as added complications. This event was momentum driven. Large plastic flow was highly localized, usually two to three projectile diameters, and was typically accounted for with incremental elastic - plastic relationships (Zukas, et al. [20]). Several failure models exist for this region. Region III involved impacts at velocities above the sound speed of the materials. The result was a hydrodynamic penetration. This was the region for which hydrocodes were originally developed. Hydrodynamic pressure dominated the event and, for all practical purposes, the material behaved as a fluid. This event was energy driven. Material strength was significant only when the problem decayed into region II. The equations of motion and a high pressure equation of state were the predominate analytical tools. Failure models were available in this region as well.

The events described in the previous chapter occurred in both regions II and III. However, in all cases, the perforation event would be considered to be in region II. The dividing line for the conditions described was approximately 2 km/s and, although some impacts were in excess of this, the penetration front velocity decayed to less than this prior to material failure.

### Governing Equations

#### Introduction

The basic equations governing the behavior of solids under impact conditions were well known and could be summarized easily. However, their solution was not. Zukas, et al. [22] implies that less than three percent of a production hydrocode was used to state these equations. The rest of the code was devoted to input-output operations and various tracking methods to advance the solution in time. Following are the principal equations used grouped into three basic categories. These equations were obtained from Wilbeck, et al. [11], Zukas, et al. [20], Zukas, et al. [24], and Malvern [25]. For consistency, the notations of Malvern [25] will be used where possible.

### Conservation Equations

The conservation of mass equation, as presented by Malvern [25] and Wilbeck, et al. [11] and as used in the hydrocodes, was

$$\frac{d\rho}{dt} + \rho \frac{\partial v_i}{\partial x_i} = 0 \quad (6-1)$$

where:

$$\begin{aligned} \vec{v} & \text{ is the velocity vector} \\ \rho & \text{ is the density} \\ \frac{d}{dt} = \frac{\partial}{\partial t} + v_i \frac{\partial}{\partial x_i} & \text{ is the material derivative.} \end{aligned}$$

The conservation of momentum equation, as presented by Malvern [25] and Wilbeck, et al. [11] and as used in the hydrocodes, was

$$\frac{\partial T_{ij}}{\partial x_j} + \rho b_i = \rho \frac{dv_i}{dt} \quad (6-2)$$

where:

$$\begin{aligned} \vec{T} & \text{ is the Cauchy stress tensor} \\ \vec{b} & \text{ is the body force vector per unit mass.} \end{aligned}$$

The conservation of energy equation, as presented by Malvern [25] and Wilbeck, et al. [11] and as used in the hydrocodes, was

$$\rho \frac{du}{dt} = \frac{1}{2} T_{ij} \left( \frac{\partial v_i}{\partial x_j} + \frac{\partial v_j}{\partial x_i} \right) - \frac{\partial q_j}{\partial x_j} + \rho r \quad (6-3)$$

where:

- $u$  is the internal specific energy
- $\vec{q}$  is the heat flux vector
- $r$  is the distributed internal heat source strength per unit mass.

### Constitutive Relations

Most hydrocodes contained a simple elastic-perfectly plastic model based on a Mises yield criterion. The most prevalent form as presented by Zukas, et al. [22] was

$$J_2' = II_T = \frac{1}{2} T_{ij}' T_{ij}' = \frac{1}{3} Y^2 \quad (6-4)$$

where

- $J_2' \equiv II_T$  is the second invariant of the deviatoric stress tensor
- $\vec{T}'$  is the deviatoric stress tensor
- $Y$  is the dynamic yield strength in uniaxial tension.

In hydrocode calculations, the material yield was checked for at each time step. Stress deviators are estimated based on elastic behavior and an effective stress,  $\sigma_{eff}$ , is calculated, as presented by Zukas, et al. [22], as follows:

$$\sigma_{eff} = \sqrt{3 J_2'} \quad (6-5)$$



If the effective value of the stress exceeded the value of  $Y$ , then plastic flow was assumed to have occurred. The estimated values of the deviatoric stress were then multiplied by a correction factor,  $\alpha$ , to insure that the deviatoric stress would lie on the Mises yield surface. The equation for performing this step, as presented by Zukas, et al. [22], is presented below.

$$\alpha = \sqrt{\frac{2 Y^2}{3 T_{ij}^{est} T_{ij}^{est}}} \quad (6-6)$$

Strain hardening can be added by incorporating into the  $Y$  term an effective plastic strain term.

$$Y = a(b + \bar{\epsilon}^p)^c \quad (6-7)$$

where:

$$\bar{\epsilon}^p = \sqrt{\frac{2}{3} \epsilon_{ij}^p \epsilon_{ij}^p} \quad (6-8)$$

$\bar{\epsilon}^p$  is the effective plastic strain term

$\epsilon^p$  is the plastic strain tensor

$a, b, c$  are constants selected to match data.

Even more elaborate models were available containing strain rate dependence and temperature effects. One of these was the Johnson model as presented by Zukas, et al. [22].

$$Y = [T(\bar{\epsilon}) + C_1 \ln(\dot{\bar{\epsilon}})](C_2 + C_3 \phi) \quad (6-9)$$

where:

- $T(\bar{\epsilon})$  is an effective quasi-static stress (based on effective strain)  
 $\bar{\dot{\epsilon}}$  is the effective strain rate  
 $\phi$  is the absolute temperature  
 $C_1, C_2, C_3$  are constants selected to match data.

Another was the Johnson-Cook model as presented by Zukas, et al. [22].

$$Y = (A + B \epsilon^n) [1 + C \ln(\dot{\epsilon}^*)] (1 - \phi^m) \quad (6-10)$$

where:

- $\epsilon$  is the equivalent plastic strain

$$\dot{\epsilon}^* = \frac{\dot{\epsilon}}{\dot{\epsilon}_0} \quad (6-11)$$

- $\dot{\epsilon}$  is the equivalent plastic strain rate  
 $\dot{\epsilon}^*$  is the dimensionless plastic strain rate  
 $\dot{\epsilon}_0 = 1.0/s$  is the nondimensionalizing term

$$\phi^* = \frac{\phi - \phi_{room}}{\phi_{melt} - \phi_{room}} \quad (6-12)$$

- $\phi_{room}$  is the ambient absolute temperature  
 $\phi_{melt}$  is the absolute temperature of the melting point  
 $\phi^*$  is the homologous absolute temperature  
 $A, B, C, n, m$  are constants selected to match data.

Both Equations 6-9 and 6-10 have the temperature effects and the strain rate effects decoupled. This was common in the hydrocodes. The advantage is that the models are relatively easy to calibrate with a minimum of experimental data.

Although not commonly in use, there were a number of models which were developed to investigate additional dependencies. The Zerilli - Armstrong model, as presented by Zukas, et al. [22], couples the strain, strain rate, and temperature for two classes of metals. For face centered cubic metals, the form is

$$Y = C_1 + C_2 \sqrt{\dot{\epsilon}} e^{(-C_3 \phi + C_4 \phi \ln \dot{\epsilon})} \quad (6-13)$$

and for body centered cubic metals, the form is

$$Y = C_0 + C_1 e^{(-C_2 \phi + C_3 \phi \ln \dot{\epsilon})} C_5 \dot{\epsilon}^n \quad (6-14)$$

where the C values and the n are constants selected to match data.

The Steinberg model, as presented by Zukas, et al. [22], was developed to account for the dependence of modulus and strength on pressure and temperature typical of shock wave experiments. The equations are:

$$G = G_0 \left[ 1 + \frac{\frac{\partial G}{\partial P}}{G_0} \frac{P}{\eta^{1/3}} + \frac{\frac{\partial G}{\partial \phi}}{G_0} (\phi - 300) \right] \quad (6-15)$$

and

$$Y = Y_0 (1 + \beta \epsilon)^n \left[ 1 + \frac{\frac{\partial Y}{\partial P}}{Y_0} \frac{P}{\eta^{1/3}} + \frac{\frac{\partial Y}{\partial \phi}}{Y_0} (\phi - 300) \right] \quad (6-16)$$

where:

subscripts of 0 denote the reference state

$\eta$  is the ratio of initial to current specific volume

$G$  is the shear modulus.

Note that although these equations are intended to be used at high strain rates, there is not an explicit strain rate dependency.

The Doraivelu model, as presented by Zukas, et al. [22], was developed to be used for materials with porosity or voids. The form of the model was

$$A(\eta)J_2' + B(\eta)J_1^2 = \delta(\eta)Y^2 \quad (6-17)$$

where:

$$A(\eta) = 2 + \eta^2 \quad (6-18)$$

$$B(\eta) = \frac{1}{3}(1 + \eta^2) \quad (6-19)$$

$\eta$  is the relative density ratio  $\rho/\rho_0$

$J_1 = I_\tau$  is the first invariant of the stress tensor

$\delta(\eta)$  is a coefficient which depends on the material.

There were also models developed for the rigid - plastic model which included pressure effect. These models are not reported on here since the rigid - plastic model was not used. These models were of more importance in work involving concrete, etc.

### Equations of State

The behavior of materials was normally modeled in the hydrocodes by decomposing the stress tensor into hydrostatic components (pressure terms) and deviatoric components (plasticity terms). Although some attempts have been made to incorporate pressure into the yield criteria as presented above, the deviatoric terms are treated as independent of pressure. The hydrostatic pressure was considered to be independent of the strain rate.

The purpose of an equation of state is to relate the thermodynamic properties (pressure and internal energy) of a material to its density and temperature. There were two basic methods used in the hydrocodes to accomplish this. In the first method, a complex form was assumed which might include rate dependency, and then experimental wave profiles were matched by trial and error variation of the constants. In the second method, a simple form analogous to the rate independent approximation in uniaxial stress was assumed and the dynamic stress - strain behavior was determined directly from experiments. Some of the more commonly used forms will be discussed below.

The model used in the HEMP hydrocode, as presented by Zukas, et al. [22], was

$$P = C_1\mu + C_2\mu^2 + C_3\mu^3 + C_4 \frac{\rho}{\rho_0} E \quad (6-20)$$

where:

$C_1, C_2, C_3, C_4$  are constants selected to match data

$$\mu = \frac{\rho}{\rho_0} - 1 \quad (6-21)$$

$\rho_0$  is the density at the initial reference state.

The Mie - Gruneisen equation, as presented by Zukas, et al. [22] and Wilbeck, et al. [11], has the form

$$P = P_H \left( 1 - \frac{1}{2} \gamma \mu \right) + \gamma p (E - E_0) \quad (6-22)$$

where:

$$P_H = C_1\mu + C_2\mu^2 + C_3\mu^3 \quad \mu \geq 0 \quad (6-23)$$

$$C_1 = \rho_0 c_0^2 \quad (6-24)$$

$$C_2 = \rho_0 c_0^2 (2k - 1) \quad (6-25)$$

$$C_3 = \rho_0 c_0^2 (3k^2 - 4k + 1) \quad (6-26)$$

$$k = \frac{u_s - c_0}{u_p} \quad (6-27)$$

$$\gamma = \frac{K_s \beta}{c_p \rho} \quad (6-28)$$

$$K_s = -V \left( \frac{\partial P}{\partial V} \right)_s \quad (6-29)$$

subscript of s denotes constant entropy

$$\beta = \frac{1}{V} \left( \frac{\partial V}{\partial \phi} \right) \quad (6-30)$$

$P_H$  is the Hugoniot pressure at density  $\rho$

$c_0$  is the reference sound speed

$u_s, u_p$  are the shock and particle velocity, respectively

$E$  is the internal energy per unit mass

$E_0$  is the reference state for  $E$

$K_s$  is the adiabatic bulk modulus

$\gamma$  is the Gruneisen parameter.

As a final model, consider the following which Wilbeck, et al. [11] states is used in many hydrocodes.

$$P = B_1\mu + B_2\mu^2 + B_3\mu^3 + B_4\mu^4 + \gamma(\mu + 1)p_0 E \quad (6-31)$$

where:

$$B_1 = C_1 \quad (6-32)$$

$$B_2 = C_2 - C_1 \frac{\gamma}{2} \quad (6-33)$$

$$B_3 = C_3 - C_2 \frac{\gamma}{2} \quad (6-34)$$

$$B_4 = -C_3 \frac{\gamma}{2} \quad (6-35)$$

C terms and others are as defined above.

#### Failure Criteria

There were a number of failure models of both the instantaneous and cumulative types available in the hydrocodes. In the instantaneous models, failure meant that the material separated. The failure criterion did not include any damage calculations. A threshold value was used to determine when failure had occurred. The critical value for stress or pressure (mean stress) can be

determined from tests. Examples of this type of model, as presented by Zukas, et al. [25] and Wilbeck, et al. [11] and as used in the hydrocodes, are as follows:

$$P < P_{fracture} \quad (6-36)$$

$$\sigma > \sigma_{fracture} \quad (6-37)$$

$$\sigma_I, \sigma_{II}, \sigma_{III} > \sigma_{fracture} \quad (6-38)$$

where:

$P$  is the mean normal pressure (tension is negative)

$P_{fracture}$  is the fracture pressure

$\sigma$  is the tensile stress

$\sigma_I$  is the first principal stress

$\sigma_{II}$  is the second principal stress

$\sigma_{III}$  is the third principal stress

$\sigma_{fracture}$  is the maximum tensile stress allowed before failure.

A critical strain to failure model can also be used. Zukas, et al. [22] presents a Hancock model which employs this technique.

$$\epsilon^{eff} = \alpha e^{\left(\frac{3\sigma_m}{2\sigma'}\right)} \quad (6-39)$$

where:

$\epsilon^{eff}$  is the effective failure strain

$\sigma_m$  is the mean stress or pressure

$\sigma'$  is the effective stress which is proportional to the root mean square of the principal shear stress

$\alpha$  is a constant used to fit experimental data.



These instantaneous models all ignore and dependence on time, strain rate, and loading history. In reality, fracture is a complex function including, as a minimum, all of these. The next level of sophistication is typified by the Tuler - Butcher model as presented by Wilbeck, et al. [11].

$$\int_0^t (\sigma - \sigma_0)^\lambda dt > K \quad (6-40)$$

where:

$\sigma_0$  is the stress below which no damage will occur

$K$  is the critical value beyond which damage occurs

$\lambda$  is the material constant used to fit experimental data.

Another such example is the plastic work model.

$$\int_0^t W_p dt > W_{pmax} \quad (6-41)$$

where:

$W_p$  is the plastic work

$W_{pmax}$  is the maximum plastic work allowed before failure

An example of still further sophistication is the Johnson - Cook model as presented by Zukas, et al. [22].

$$D + \sum \frac{\Delta \epsilon}{\epsilon^f} \quad (6-42)$$

where:

$$\epsilon' = (D_1 + D_2 e^{D_3 \sigma^*}) [1 + D_4 \ln(\dot{\epsilon}^*)] (1 + D_5 \phi^*) \quad (6-43)$$

$$\sigma^* = \frac{\sigma_1 + \sigma_2 + \sigma_3}{3\sqrt{3}J_2'} \quad (6-44)$$

$\sigma^*$  is a dimensionless pressure-stress ratio

$\sigma_1, \sigma_2, \sigma_3$  are the principal stresses

$\phi^*$  is the homologous temperature

$$\dot{\epsilon}^* = \frac{\dot{\epsilon}}{\dot{\epsilon}_0} \quad (6-45)$$

$\dot{\epsilon}^*$  is the dimensionless strain rate ( $\dot{\epsilon}_0 = 1.0/\text{s}$ )

$\epsilon'$  is the equivalent strain to fracture corresponding to the instantaneous conditions when the increment of strain is accumulated

$\Delta\epsilon$  is the increment of equivalent plastic strain which occurs during the tensile loading history

$D$  is the damage parameter.

For this model, fracture occurs when  $D=1$ .

### Discussion of Equations

The differential equations presented in the previous section were basic to, and used in, most production hydrocodes. The exceptions to this were the equation of state and fracture models. Generally only a subset was present. None of the fracture models represented the depth of detail usually involved with crack onset or crack propagation models.

Fracture and the resulting formation of the BAD field was a recent concern of the hydrocode community; dating back only to the late 1970s. It is anticipated that, in time, these models will improve.

### Spatial Discretization

There were two methods used to provide the spatial discretization needed to solve these governing equations: finite difference and finite elements. Finite difference approximated the differential equations, boundary conditions, and initial conditions by substitution of differential operators and solved the resulting set of algebraic equations numerically using standard techniques. Finite elements replaced the continuum with a finite degree of freedom system and solved the results exactly. Zukas, et al. [22] states that if the effort was done correctly, there was no basic mathematical difference between the methods so the results should have the same degree of accuracy. The main difference lies not in the methods but in the data management involved. Since the finite difference technique was developed with irregularly shaped objects in mind and was not an outgrowth of the requirements of a technique, such as was true of finite difference, this technique offered some distinct advantages in the initial setup of a complex geometric problem.

Spatial discretization can be carried out in Eulerian or Lagrangian frameworks. In the Eulerian method, the grid was fixed in space and the material flowed through it. In the Lagrangian method, the grid was fixed to the material and flowed with it. There were advantages and disadvantages to both methods and the tendency is toward development of codes with both techniques. Basically, Eulerian codes must have convective terms to move the material through the grid and

Lagrangian codes must have slide line capability for transfer of momentum during penetration or impact. Although the Lagrangian formulization, even with elaborate slide lines, was still more efficient than the Eulerian codes, it suffered from another problem. As the grid became heavily distorted, the time increments must decrease and the resulting time to complete the study will go up. Other problems were also associated with these distortions. However, a solution was developed. When distortion reached a predetermined point, a rezoning of the material occurred. This, of course, added additional time.

### Time Integration

Time integration was generally done through the use of an explicit central difference method. The stability of the method was controlled by the Courant stability criterion, as presented by Zukas, et al. [22].

$$\Delta t = \frac{\min \Delta x}{\max (c, u)} \quad (6-46)$$

where:

$\Delta t$  is the time step

$\Delta x$  is the spatial step

$c$  is the characteristic material sound speed

$u$  is the particle velocity

and the minimization was taken over the entire grid. Thus the smallest cell or element governed the time step for the entire grid.

### Artificial Viscosity

Mathematical discontinuities could not be directly dealt with in the continuum of current hydrocodes. Thus an artificial viscosity was used to spread shock fronts over several grid widths. This term was added to the pressure computed from the equation of state.

$$q = \begin{cases} c_1 \rho / \Delta |\dot{\epsilon}| - c_0 \rho^{1/2} \dot{\epsilon} |\dot{\epsilon}|, & \dot{\epsilon} < 0 \\ 0, & \dot{\epsilon} \geq 0 \end{cases} \quad (6-47)$$

where:

- $q$  is the artificial viscosity
- $c_0$  is the user defined constant
- $c_1$  is the user defined constant
- $\rho$  is the material density
- $\Delta$  is the characteristic grid length
- $\dot{\epsilon}$  is the volumetric strain rate.

The addition of the artificial viscosity term also added another complexity. As a result, the stability criterion presented as Equation 6-46 had to be modified. Wilbeck, et al. discussed this problem in some depth and presented an empirical form to be used.

Chapter Summary

Production hydrocodes had excellent capabilities in computing results of impacts. These capabilities were greatly enhanced when data were available to compare to the code result and thus enable a refining of the input data. This calibration process was generally required if detailed studies were to be conducted. The only major weakness in the codes was in the area of fracture and the resulting formation of the BAD field. As a class, the fracture models were simplistic. Since this was the latest area to be developed in the codes, this was understandable.

## CHAPTER 7 SUMMARY, CONCLUSIONS, AND RECOMMENDATIONS

The primary objective of the study was to determine whether the mass of the BAD was on the surface bubble (Figure 2). The new spall field slicing procedure has clearly shown that it was not. The field actually consisted of a cloud of particles having significant velocity variation along any given ray. This finding will have a profound impact on the vulnerability modeling community which currently assumes all mass to be on the surface bubble and thus a constant velocity on any ray. A statistical variation of the velocity along a ray and an associated mass distribution will have to be developed. This further implies that a statistically significant quantity of data will have to be gathered to accomplish this effort. The make screen procedure, also developed as part of this study, holds excellent potential as a means of collecting these data since it can be incorporated into the normal test procedure. However, as explained in the body of this report, a significant amount of work still remains to perfect this procedure into a standard test technique. A second method of obtaining a statistically significant set of data would be through modeling and simulations using a hydrocode.

A secondary objective of this study was to investigate the use of a commercially available hydrocode to determine if the code could replicate the test results. The code selected was CTH, an Eulerian code. After a considerable amount of parameter studies, as detailed in this dissertation, a reasonable match was achieved. Figures 110, 111, and 112 present the match between the

predicted BAD velocity fields and those reduced from the spall field slicing experiments for 0.75-inch (0.01905 meter) , 2.00-inch (0.0508 meter), and 2.50-inch (0.0635 meter) targets, respectively. Due to the slight variations in impact velocities for the various impact tests, all velocity data were presented as a ratio of the measured or calculated fragment velocity and the impact velocity. Figure 110 provides little insight since most of the predicted velocity data suffered from severe data dropout as explained within the body of this dissertation. Figure 112 is the most informative. This figure presents data from two tests, as well as predicted values, calculated using three different values of the target material dynamic fracture strength. Several conclusions can be drawn from these figures:

1. Dynamic fracture strength plays a major role in the resulting BAD data. Anything from a single bubble result to a wide band of fragments (multiple bubbles) can be achieved by using different values.
2. Variations in the calculated velocities along a ray can be achieved with changes to the dynamic fracture strength.
3. The test results cover a wider variation in velocity than do the results of the calculation performed with a dynamic fracture strength of -0.85 GPa. However, they were generally within the variations in velocity predicted by the calculation using a dynamic fracture strength of -0.50 GPa.



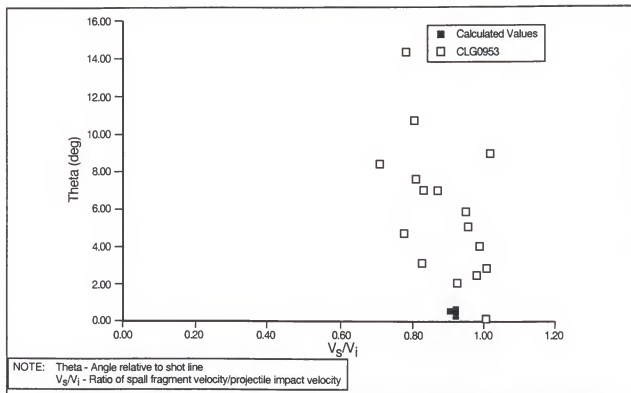


Figure 110. Comparison of the Calculated Values for BAD Velocity and Those Determined from Actual Tests - 0.75-Inch (0.01905 Meter) Target

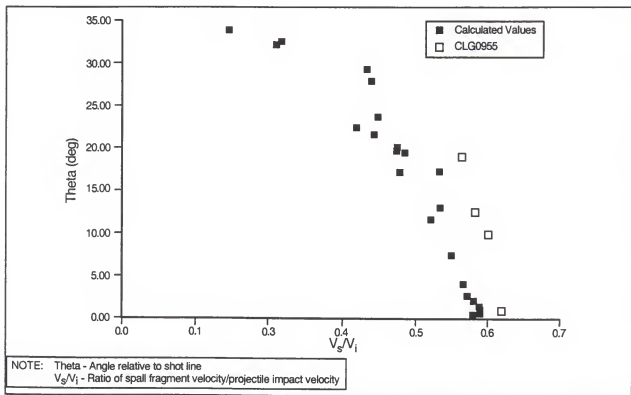


Figure 111. Comparison of the Calculated Values for BAD Velocity and Those Determined from Actual Tests - 2.00-Inch (0.0508 Meter) Target

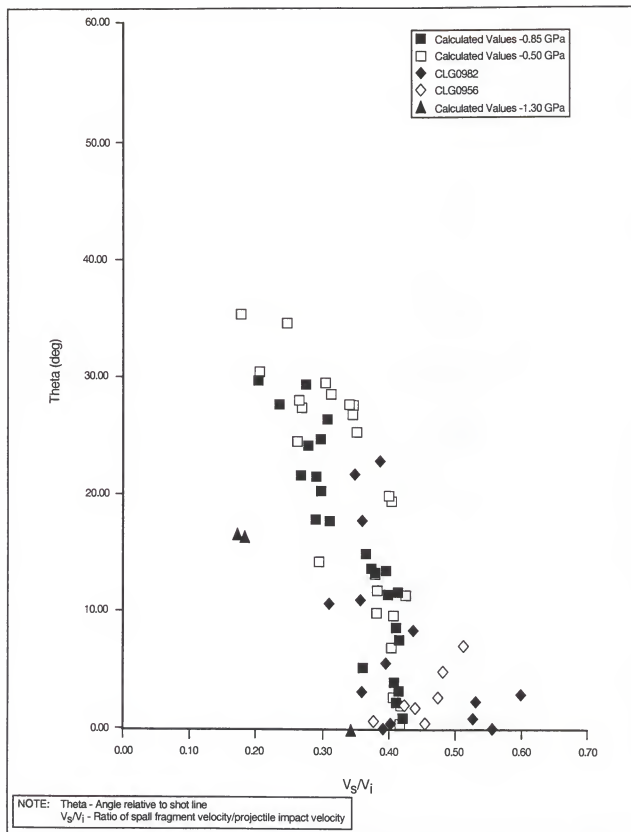


Figure 112. Comparison of the Calculated Values for BAD Velocity and Those Determined from Actual Tests - 2.50-Inch (0.0635 Meter) Target

Figures 113 and 114 present the calculated values for the 2.50-inch (0.0635 meter) target in a different manner. This was done to examine if the different layers of the armor plate contributed to the variation in velocity. The calculation using a dynamic fracture strength of -0.85 GPa (Figure 113) was inconclusive. However, the calculation using a dynamic fracture strength of -0.50 GPa (Figure 114) was more enlightening. The trend was that the deeper into the armor, from the back, that the particle originated, the slower the velocity along a given ray. This would be in keeping with the concept that the BAD fragment velocities were, in part, due to the momentum captured from the stress wave. Since the largest momentum would occur at the back and the resulting energy in that wave would be decreased after the fracture then the next layer should have a lower velocity.

Comparison of the total mass and mass distribution was not possible in other than a qualitative manner. Without modifications to the code, mass values for the fragments were not available. As discussed in the body of the report, the calculated results compared well with the test results at this level of detail. The exception was along the shot line. This problem may well be attributed to the axisymmetrical calculations.

Two other observations with regard to calculated BAD fields and actual test results should be noted:

1. For a given set of impact parameters, the code will always predict exactly the same BAD field. This deterministic approach does not match what actually occurs.
2. The code-predicted BAD field displays no apparent rotational behavior. The actual fields contain particles which have significant rotational behavior. This will, of course, affect the energy balance.

Finally, the importance of material properties should be noted. The entire computational study revolved around sensitivity investigations involving these values. The results were found to depend greatly on those values which were not available or not readily available to the general community. Further testing to determine these values at high strain rates is needed.

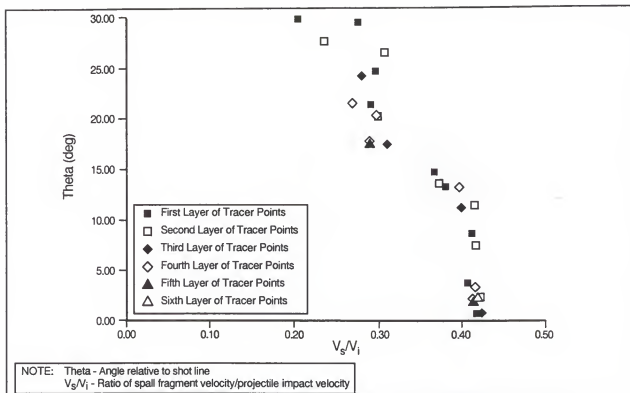


Figure 113. Tracer Point Velocities as a Function of Origin for 2.50-Inch (0.0635 Meter) Target Impact (Fracture Strength = -0.85 GPa)

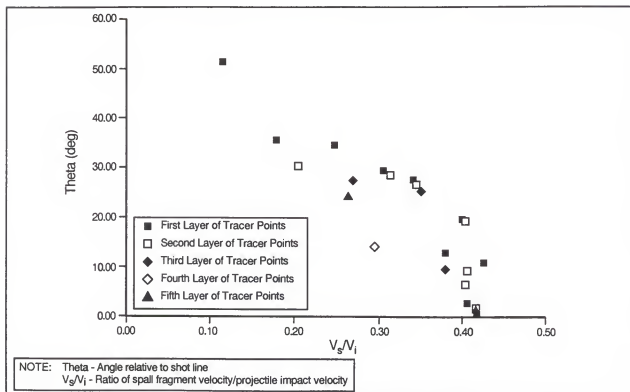


Figure 114. Tracer Point Velocities as a Function of Origin for 2.50-Inch (0.0635 Meter) Target Impact (Fracture Strength = -0.50 GPa)

## REFERENCES

1. Canadian Armament Research and Development Establishment, "Tripartite Anti-Tank Trials and Lethality Evaluation, Part I." November 1959.
2. Nail, C. L., E. Jackson, and T. E. Beardon, "Vulnerability Analysis Methodology Program (VAMP): A Combined Compartment-Kill Vulnerability Model." Computer Sciences Corporation Technical Manual CSC TR-79-5585, October 1979.
3. Flint, J. B., "Submunition Evaluation Program Project CHICKEN LITTLE; Volume X: Vulnerability Models; Part 3: PDAM Spall Model." AD-TR-87-67, November 1987.
4. Nail, C. L., "Vulnerability Analysis for Surface Targets (VAST)- An Internal Point-Burst Vulnerability Assessment Model-Revision I." Computer Sciences Corporation Technical Manual CSC TR-82-5740, August 1982.
5. Ozolins, A., "Stochastic High-Resolution Vulnerability Simulation for Live-Fire Programs." *The Proceedings of the Tenth Annual Symposium on Survivability and Vulnerability of the American Defense Preparedness Association*, held at the Naval Ocean Systems Center, San Diego, California, May 10-12, 1988.
6. Woodward, Raymond L., "Penetration of Semi-infinite Metal Targets by Deforming Projectiles." *International Journal of Mechanical Science*, Vol. 24, No. 2, pp. 73-87, 1982.
7. Johnson, G. R., R. A. Stryk, T. J. Holmquist, and O. A. Souka, "Recent EPIC Code Developments for High-Velocity Impact: 3D Element Arrangements and 2D Fragment Distribution." *International Journal of Impact Engineering*, Vol. 10, pp. 281-294, 1990.
8. Grady, D. E., "The Spall Strength of Condensed Matter." *Engineering Fracture Mechanics, An International Journal*, Vol. 36, pp. 353-384, 1987.
9. Zukas, J. A. and K. D. Kimsey, "Supercomputing and Computational Penetration Mechanics." Technical Report BRL-TR-3143, August 1990.
10. Dyess, W. W., Jr., "Submunition Evaluation Program; Project CHICKEN LITTLE, Volume IV: Range Target Tests; Part 1: Test Design and Conduct." AD-TR-87-62, September 1987.

11. Wilbeck, J. S., C. E. Anderson, Jr., J. P. Riegal III, J. Lankford, S. A. Mullin, and S. R. Bodrier, *Course Notes - A Short Course on Penetration Mechanics*. San Antonio, Texas: Southwest Research Institute, 1990.
12. Matuska, Daniel A., "A High Velocity Penetration Model." AFATL-TR-84-58, June 1984.
13. Dyess, William W., Jr., "Submunition Evaluation Program; Project CHICKEN LITTLE; Volume IV: Range Target Tests; Part 3: Evaluation of the AVCO Skeet." AD-TR-87-78, October 1987.
14. Dyess, William W., Jr., "Submunition Evaluation Program; Project CHICKEN LITTLE; Volume IV: Range Target Tests; Part 6: Summary Comparison." AD-TR-87-79, November 1987.
15. McGlaun, J. M., S. L. Thompson, and M. G. Elrick, "CTH: A Three-Dimensional Shock Wave Physics Code." *International Journal of Impact Engineering*, Vol. 10, pp. 351-360, 1990.
16. Silling, S. A., "CTH Reference Manual: Viscoplastic Models." SAND91-0292, June 1991.
17. Taylor, Paul A., "CTH Reference Manual: The Steinberg-Guinan-Lund Viscoplastic Model." SAND92-0716, September 1992.
18. O'Donoghue, P. E., C. E. Bodner, C. E. Anderson, Jr., and M. Ravid, "Comparison of a High Velocity Impact Model with Numerical Simulation." *International Journal of Impact Engineering*, Vol. 8, No. 4, pp. 289-301, 1989.
19. Ravid, M., S. R. Bodner, and I. Holeman, "Analysis of Very High Speed Impact." *International Journal of Engineering Science*, Vol. 25, No. 4, pp. 473-482, 1987.
20. Zukas, J. A., T. Nickolas, H. F. Swift, L. B. Greszczuk, and D. R. Curran, *Impact Dynamics*. New York: Wiley-Interscience, 1982.
21. Lyman, Taylor (editor), *Metals Handbook*. Novelty, Ohio: The American Society for Metals, April 1960.
22. Hertel, E. S., "A Comparison of Calculated Results with Experimental Data for Long Rod Projectiles." SAND90-0610, December 1990.
23. Kmetyk, L. N. and P. Yarrington, "Cavity Dimensions for High Velocity Penetration Events - A Comparison of Computational Results with Data." SAND88-2693, May 1989.

24. Zukas, J. A., V. Holer, R. L. Jameson, C. L. Mader, T. Nicholas, A. M. Rajendran, R. F. Recht, A. J. Stilp, W. P. Walters, and R. L. Woodward, *High Velocity Impact Dynamics*. New York: Wiley-Interscience, 1990.
25. Malvern, L. E., *Introduction to the Mechanics of a Continuous Medium*. Englewood Cliffs, New Jersey: Prentice-Hall, Inc., 1969.

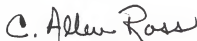


## BIOGRAPHICAL SKETCH

William Winfield Dyess, Jr., was born in San Francisco, California, in 1945 and raised in Robertsedale, Alabama. He entered Auburn University in June 1964 and graduated with a Bachelor of Aerospace Engineering in August 1967 and with a Master of Science degree in aerospace engineering in August 1969.

In 1969, Mr. Dyess was employed as an Aircraft/Store Compatibility Engineer at Eglin Air Force Base, Florida. In 1980, he transferred to the position of Warhead Lethality Engineer, still at Eglin Air Force Base. In 1989, he married Mildred F. Campbell. He applied and was selected for the Air Force Development Test Center Long-Term, Full-Time training program in 1991 and completed his residency requirements for the Doctor of Philosophy degree in 1992. Upon return from school, he was transferred to the position of Technical Director of the Munitions Test Division of the 46th Test Wing of the Air Force Development Test Center at Eglin Air Force Base. While working there, he completed the requirements for his doctoral degree. He also has three sons from a previous marriage and holds the position of Adjunct Assistant Professor with Troy State University, where he has been teaching math and physics since 1981.

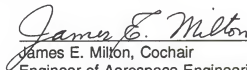
I certify that I have read this study and that in my opinion it conforms to acceptable standards of scholarly presentation and is fully adequate, in scope and quality, as a dissertation for the degree of Doctor of Philosophy.



---

C. Allen Ross, Chair  
Professor Emeritus of Aerospace  
Engineering, Mechanics and  
Engineering Science

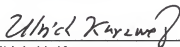
I certify that I have read this study and that in my opinion it conforms to acceptable standards of scholarly presentation and is fully adequate, in scope and quality, as a dissertation for the degree of Doctor of Philosophy.



---

James E. Milton, Cochair  
Engineer of Aerospace Engineering,  
Mechanics and Engineering Science

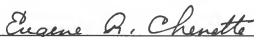
I certify that I have read this study and that in my opinion it conforms to acceptable standards of scholarly presentation and is fully adequate, in scope and quality, as a dissertation for the degree of Doctor of Philosophy.



---

Ulrich H. Kurzweg  
Professor of Aerospace Engineering,  
Mechanics and Engineering Science

I certify that I have read this study and that in my opinion it conforms to acceptable standards of scholarly presentation and is fully adequate, in scope and quality, as a dissertation for the degree of Doctor of Philosophy.



---

Eugene R. Chenette  
Professor Emeritus of  
Electrical Engineering

I certify that I have read this study and that in my opinion it conforms to acceptable standards of scholarly presentation and is fully adequate, in scope and quality, as a dissertation for the degree of Doctor of Philosophy.



---

Nicolae D. Cristescu  
Graduate Research Professor of  
Aerospace Engineering, Mechanics  
and Engineering Science

This dissertation was submitted to the Graduate Faculty of the College of Engineering and to the Graduate School and was accepted as partial fulfillment of the requirements for the degree of Doctor of Philosophy.

December 1994



---

Winfred M. Phillips  
Dean, College of Engineering

---

Karen A. Holbrook  
Dean, Graduate School